

Geologic Storage of Carbon Dioxide

Principal Investigators

Jerry Harris, Professor, Geophysics; Anthony Kavscek, Associate Professor, Franklin Orr, Jr., Professor, Energy Resources Engineering; Mark Zoback, Professor, Geophysics.

Investigators

Paul Hagin, Youli Quan, Research Associates, Geophysics; Tom Tang¹, Senior Research Associate, Energy Resources Engineering; Eduardo Santos, Postdoc, Geophysics; Adeyemi Arogunmati, Laura Chiaramonte, Jolene Robin-McCaskill, John P. Vermeylen Graduate Research Assistants, Geophysics; Abhishek Dutta, Taku Ide, Wenjuan Lin, Graduate Research Assistants, Energy Resources Engineering; Kristian Jessen², Acting Assistant Professor, Energy Resources Engineering.

Collaborators

Reginald Mitchell, Associate Professor, Mechanical Engineering, David Pollard, Professor, Geological and Environmental Sciences. Sally M. Benson, Professor, Energy Resources Engineering.

Abstract

We report our progress in an interdisciplinary, fundamental study of CO₂ transport and sequestration in deep, unmineable coal seams. Experiments, modeling, and theory development are combined. The integrated laboratory study probes physical and chemical properties including permeability, acoustic properties, rock compressibility, elastic-plastic deformation, and adsorption. Coal samples from the Powder River Basin, Wyoming, present mechanical and flow properties that change dramatically in the presence of carbon dioxide. Notably, we observe that CO₂ adsorption causes the static bulk modulus to decrease by a factor of two, while simultaneously causing the dynamic bulk modulus to increase by several percent. Permeability decreases by approximately an order of magnitude in the presence of CO₂, which is consistent with observations of adsorption-related swelling of the coal matrix. CO₂ also appears to change the constitutive behavior of coal; helium saturated coal samples exhibit elastic behavior, while CO₂ saturated samples exhibit viscous, anelastic behavior, as evidenced by creep strain observations. This understanding of coal constitutive relations in the presence of CO₂ provides valuable parameter input for current and future modeling studies.

Findings to date from five complementary modeling studies are presented. The first is a continuation of our work to formulate a model for gas-flow with adsorption through coal. The extended Langmuir and the ideal adsorbed solution (IAS) models are contrasted for description of multicomponent adsorption. It is found that adsorption hysteresis is a complicating factor for computations. Second, given the safety risk associated with injection and sequestration of CO₂, it is imperative to identify and model the risk of migration through potential leakage pathways. We have investigated the feasibility of CO₂ sequestration at Teapot Dome oil field, Wyoming with the objective of predicting the risk of CO₂ leakage. Third, we are expanding our previous coalbed methane reservoir simulation studies to include gas shale reservoirs. We have begun reservoir modeling, risk analysis, and economic assessment to test the feasibility of CO₂ sequestration and

¹ Currently at Chevron, ² Currently at the University of Southern California

enhanced recovery in the Barnett shale in Texas. Fourth, we outline work done to characterize a subsurface fire at a location in the San Juan Basin near Durango, Colorado. The fire was discovered in 1998 and continues to burn today, but anecdotal evidence from suggests that the fire may have been burning for decades. The research effort described here is an attempt to understand the geometry and flow setting of the fire so that pressure gradients that drive the flow of oxygen to the combustion zone can be estimated.

We discuss three algorithms for implementing dynamic imaging for monitoring CO₂ storage. Each provides a methodology for integrating old time-lapse data with new data in order to update the subsurface model. The first algorithm, the ensemble Kalman filter (EnKF), is a stochastic method. We demonstrate it using time-lapse surface seismic data. Unlike conventional seismic methods that give relative impedance, the EnKF inversion yields absolute seismic velocity. The second is a specific dynamic imaging algorithm we call DynaSIRT. DynaSIRT integrates data from previous surveys and updates the model without reprocessing older data. It preserves state variables that store the temporally damped data from previous surveys and timestamps data to track parameter updates. We show results of DynaSIRT applied to synthetic time-lapse diffraction tomography data, where it provides a clear detection of a CO₂ leak even for sparse survey geometry. Lastly, we introduce the method of data evolution to supplement sparse data surveys for continuous monitoring. Data evolution may be used with any dynamic imaging stream to supplement sparse data recordings with predicted data based on spatio-temporal interpolation. Data evolution, when combined with new sparse surveys, moves us closer to an ideal data processing of quasi-continuous subsurface monitoring. And finally, we report a feasibility study for the use controlled-source electromagnetics (CSEM) for monitoring geological CO₂ storage in coal. In order to test various monitoring methods and strategies, we used relatively realistic time-lapse seismic and electrical models that were constructed from flow simulation and rock physics.

Introduction

Despite the considerable activity worldwide to investigate many of the practical issues related to implementation of widespread geological sequestration of carbon dioxide, fundamental scientific and engineering science questions remain regarding the injection of carbon dioxide into deep unmineable coal seams. Questions of similar scope also remain about the use of gas injection to enhance coalbed methane recovery. This report summarizes progress of laboratory, theoretical and field studies investigating the feasibility of CO₂ sequestration in coal and the ability to monitor effectively the distribution of CO₂ in a geological repository after injection.

This report is roughly organized as follows. Site assessment and evaluation themes are presented first. These are followed a description of our efforts to quantify fluid migration within coal. Finally, monitoring strategies for assessing plume dynamics are outlined.

Three laboratory groups currently conduct experiments on coal samples. We continue to take full advantage of the combined capabilities of our laboratory equipment, and we have tightly integrated our experimental research efforts. To summarize, Mark Zoback is directing an effort to measure the elastic, viscoplastic and flow properties of coal, including shrinkage and swelling, as a function of gas adsorption. Tony Kavscek is directing an effort to measure adsorption isotherms, probe adsorption induced permeability changes to coal, and study the flow and transport properties of coal. Jerry Harris is directing an effort to measure the dynamic elastic properties and attenuation of coal. Our experimental efforts and results are summarized in the sections entitled “Laboratory Studies of the Mechanical, Flow, and Adsorption Properties of Low-Rank Coal Samples from the Powder River Basin, Wyoming”; “Gas Sorption and Coal Permeability”; “Multicomponent Sorption Modeling During Convective Transport in Coalbeds.”

A similar high level of activity is underway in the area of site assessment and modeling. Mark Zoback and coworkers are investigating site assessment techniques incorporating fluid flow and geomechanical constraints. Tony Kavscek and collaborators are probing numerical description of carbon dioxide transport-adsorption and subsequent swelling of coal matrix. These contributions are found in the sections entitled “Reservoir Model for Fluid Flow Simulations with Geomechanical Constraints Teapot Dome Wyoming”, “Multicomponent Sorption Modeling During Convective Transport in Coalbeds.”, and “Multicomponent Sorption Modeling During Diffusive Transport in Coalbeds.”

Lynn Orr and coworkers continue their study of reactive processes in coal to characterize, from a subsurface perspective, the progression of events leading to a self-sustaining fire in a coalbed. Coalbed fires account for significant emissions of carbon dioxide to the atmosphere. The study is entitled, “Field Study and Analysis of a Coal Bed Fire.” Geological field observations and coalbed gas composition data are combined with geomechanical modeling for the formation of fissures in coal.

Jerry Harris and collaborators are investigating quasi-continuous strategies for monitoring the subsurface volume contacted by carbon dioxide. This work includes acquisition strategies as well as the optimal tradeoffs made between temporal and spatial accuracy. These techniques are designed to construct time-lapse subsurface images using relatively low-resolution active seismic imaging in order to reduce the cost of quasi-continuous long-term monitoring.

Background

Three principal settings are being considered for geologic sequestration of carbon dioxide – deep saline aquifers, depleted oil and gas reservoirs, and deep unmineable coal seams. Of these, coal bed storage of CO₂ remains the least well understood. While the potential volumes of storage in coal beds are more variable in comparison to the other geological settings, the appreciable coal deposits in the U.S., China, Russia and India, provide important opportunities to sequester CO₂ if coalbeds are indeed a viable storage setting for greenhouse gases. The work summarized here represents concrete steps related to improved quantitative evaluation of this storage mechanism as well as the potential for cost recovery associated with ECBM.

Laboratory Studies of the Mechanical, Flow, and Adsorption Properties of Low-Rank Coal Samples from the Powder River Basin, Wyoming

Introduction

Coal bed methane (CBM) production from unmineable coal seams is an unconventional gas resource of increasing importance. Methane is generated during the coal maturation process and as a result of microbial action and resides in the coal matrix as an immobile, adsorbed phase. During CBM production, the pressure inside a coal seam is reduced and methane desorbs from the coal matrix, at which point it exists as a free gas and can flow through the cleat (natural fracture) system to the producing wells. According to the U.S. Energy Information Agency (EIA), coal bed methane production currently accounts for 10% of the domestic natural gas supply, and is anticipated to increase significantly over the next several decades as conventional gas supplies continue to decline [1].

Coal exhibits the interesting property of selectively adsorbing certain gases. In particular, many coals have been observed to preferentially adsorb carbon dioxide over methane [2], making coal an attractive candidate for geological sequestration of CO₂, since adsorbed gases are essentially immobile [3, 4]. In addition, because the adsorption of carbon dioxide forces desorption of methane, it is possible that CO₂ can be used to enhance coal bed methane (ECBM) production [5, 6, 7].

While several small-scale field studies have been performed (or are currently underway) in various coal seams around the world [8, 9, 10, 11], the feasibility of ECBM or geological sequestration of CO₂ for a given site is still largely dependent on predictions from numerical modeling tools such as reservoir simulators that have been modified for CBM [12, 13]. These numerical models require values for numerous input parameters, many of which can be derived from laboratory data.

Furthermore, predictions from reservoir simulators can only be as accurate and realistic as the underlying theoretical and mathematical models allow. Laboratory studies are needed to develop and verify theoretical models of the complex mechanical and chemical behavior of coal. For example, the adsorption of gases onto the surfaces of the coal matrix has been observed to cause volumetric swelling of the coal, while desorption of gases causes volumetric shrinkage [14, 15]. This swelling and shrinkage of the matrix changes the width of the cleats and natural fractures in the coal, which in turn causes changes in cleat permeability [16, 17, 18]. Because adsorption, and therefore swelling, increases with pressure, permeability is expected to decrease as a function of pressure. However, in the absence of swelling, permeability will increase as a function of pressure. These opposing effects need to be better understood if accurate models of permeability change are to be developed for coal.

The Powder River Basin, which extends from eastern Wyoming into southeastern Montana, is the largest and fastest growing CBM producer in the world, with approximately 17,000 wells currently producing 30 billion cubic feet of gas per month

[19]. The primary production coal seams fall within the Wyodak-Anderson zone of the Fort Union Formation, at depths ranging from 500 to 1500 feet. For this study, we obtained four-inch diameter core samples from the Roland and Smith coal zones, from a depth range of 1300-1400 feet. The samples have an initial porosity of approximately 10%, an initial permeability of 1 millidarcy, and ash content that varies from 10-20%.

Our research focus for this study has been to better understand the effects of adsorption on the mechanical and flow properties of sub-bituminous coals. We conducted laboratory experiments on one-inch diameter core samples of coal, under hydrostatic and triaxial loading conditions, as a function of effective stress, using both helium and carbon dioxide as saturating gases. We present measurements of elastic stiffness, permeability, swelling strain, and creep strain, for both intact and powdered coal samples. We also present independent verification of the adsorption isotherms for PRB coal published in previous GCEP reports by the Earth Resources Engineering research group under supervision of Tony Kovscek.

Background

In an effort to better understand the technical and safety issues associated with ECBM and sequestration of CO₂ in unmineable coal seams, a number of small-scale pilot studies are ongoing or expected to begin in the near future. In addition, a number of laboratory studies of the adsorption and flow properties of coal have been performed, with a particular focus on relating swelling/shrinkage to changes in permeability. These laboratory and field studies provide valuable data and information to researchers focused on theoretical and numerical models of the complex mechanical and chemical interactions during injection of CO₂ into coal.

International Pilot Studies

The distinguishing characteristics of the international pilot studies that have been completed-to-date are their small size and location in areas where active CBM production is not currently underway. The RECOPOL/MOVECBM project, an ECBM pilot study in Poland, completed its active phase in 2007. This project involved a single injector and producer well pair, with an injection target-rate of 1 ton of pure CO₂ per day (for reference, approximately 3000 tons of CO₂ per day are injected at the Sleipner Field). While CO₂ injection was observed to enhance methane production, injectivity was lower than expected until the injector well was stimulated via hydraulic fracturing. The study authors concluded that, “interaction between CO₂ and coal under reservoir conditions is still a research issue” [8]. A 4-D surface seismic array was used to monitor the movement of the injected CO₂ during the second phase of the project; to date, we are not aware of any published results from this part of the study.

A second small-scale ECBM pilot study was carried out near the city of Yubari, Japan, from 2003 to March of 2008. While this study also involved a single injector and producer well pair, and had a similar injection rate (~ 3 tons of CO₂ per day), it differed from RECOPOL in that both CO₂ and Nitrogen were injected. Interestingly, the study authors observed that permeability decreases in the vicinity of the injector well, possibly caused by CO₂-related swelling of the coal, were temporarily reversed following nitrogen flooding [9]. This observation supports laboratory observations and numerical

simulations that suggest that injecting gas mixtures of CO₂ and N₂, rather than pure CO₂, will minimize swelling and permeability loss [e.g. 20].

U.S. Pilot Studies

A number of pilot studies are currently being planned and implemented as part of the U.S. DOE/NETL network of regional partnerships for carbon sequestration. As compared with the international pilot studies previously described, these projects tend to be larger in scope and located in areas of active CBM production. Pilot studies are planned for the Black Warrior Basin in Alabama, the San Juan Basin in New Mexico, and the Illinois Basin. For details, please refer to http://www.netl.doe.gov/technologies/carbon_seq/index.html.

In addition to the pilot studies sponsored by the Department of Energy, it is worth noting that Consol Energy is conducting a pilot study to explore the possibility of making ECBM economical in the current market [7]. This pilot study is awaiting final permitting approval and should begin this year.

Laboratory Studies

As mentioned above, recent experimental efforts have focused on better understanding the relationship between coal swelling/shrinkage and permeability change. Robertson and Christiansen conducted a series of laboratory experiments on coal samples from the Powder River Basin, and found that an empirically derived variable modifier was needed to relate unconfined swelling strain to permeability reductions using the Palmer-Mansoori and Shi-Durucan models [21]. This result is interesting because most off-the-shelf reservoir simulators use either the Palmer-Mansoori or Shi-Durucan equations to model shrinkage and swelling. Fujioka [9] conducted laboratory experiments on samples of the Bibai coal from the Ishikari Basin, which focused on testing the repeatability of physical properties measurements after flooding a CO₂ saturated sample with N₂. Interestingly, while shrinkage and swelling strains were observed to be reversible and repeatable, permeability and ultrasonic P-wave velocity were observed to permanently change during the initial CO₂ saturation phase. In addition, some fundamental research into how adsorption of CO₂ changes the micro and meso pore structure of coal is being carried out [22]. Notably, the authors find that CO₂ adsorption decreases the mean pore size of vitrains, but does not effect the pore size distribution of other components of coal.

Results

Sample Description and Experimental Procedure

We obtained 4-inch diameter core samples of sub-bituminous coal from the Roland and Smith coal zones of the Fort Union Formation in the Powder River Basin, Wyoming. The depth to these zones is approximately 1300-1400 feet. Note that these samples are from the same well and depth range as those reported on by Tang *et al.* [24] in previous GCEP reports. Figure 1 shows the field area and the stratigraphic column. These samples were stored at room conditions, and so it was assumed that the initial methane gas was completely desorbed prior to testing. Due to the numerous cleats and microfractures, obtaining one-inch diameter core plugs for testing was difficult, and some samples were molded from powdered coal. For both the intact and powdered coal samples, sample

preparation procedures followed those initiated by Tang *et al.*, in an effort to make comparison of the two data sets possible.

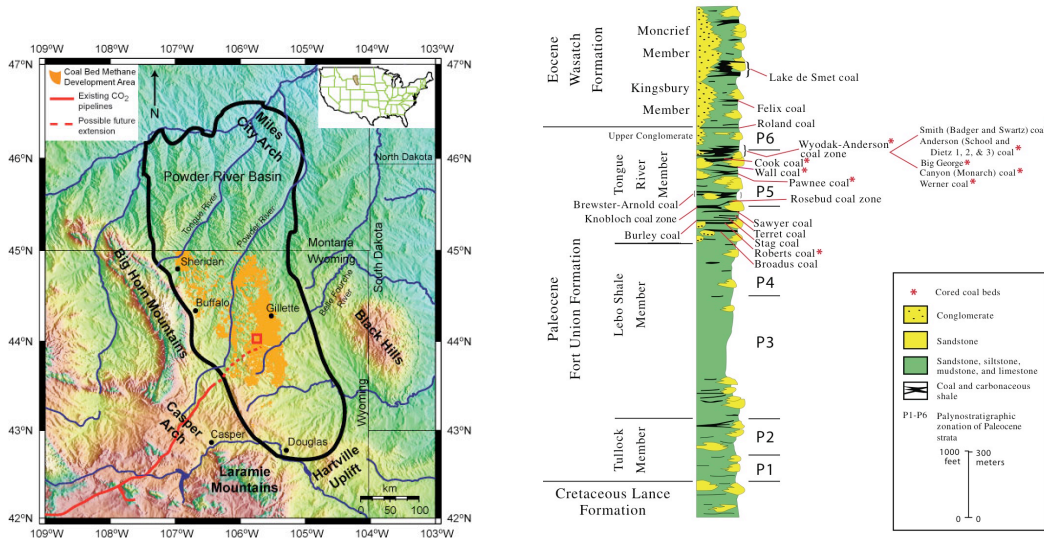


Figure 1: Topographic map of the Powder River Basin, showing the area of active CBM development (adapted after 25) and stratigraphic column of the major formations and coal zones of the Powder River Basin (adapted after 19).

For both the intact and powdered samples, cylindrical core plugs were prepared, with a nominal size of one-inch diameter and two-inch length. For reference, the initial porosity of the intact samples was approximately 10%, while that of the molded samples was approximately 30%. The samples contain 10-20% ash content, which serves to reduce the initial bulk density (~1.5 g/cc for the intact samples). Prior to testing, all samples were vacuum-dried until constant mass was achieved, to remove residual moisture and gas.

Our laboratory apparatus (Fig. 2) is a conventional triaxial machine, commonly used in rock mechanics testing. For the purpose of this study, we modified it to enable simultaneous measurement of stress and strain, ultrasonic P and S wave velocities, and gas permeability. For schematics and specific details concerning the apparatus, please consult the 2006 GCEP Annual report.

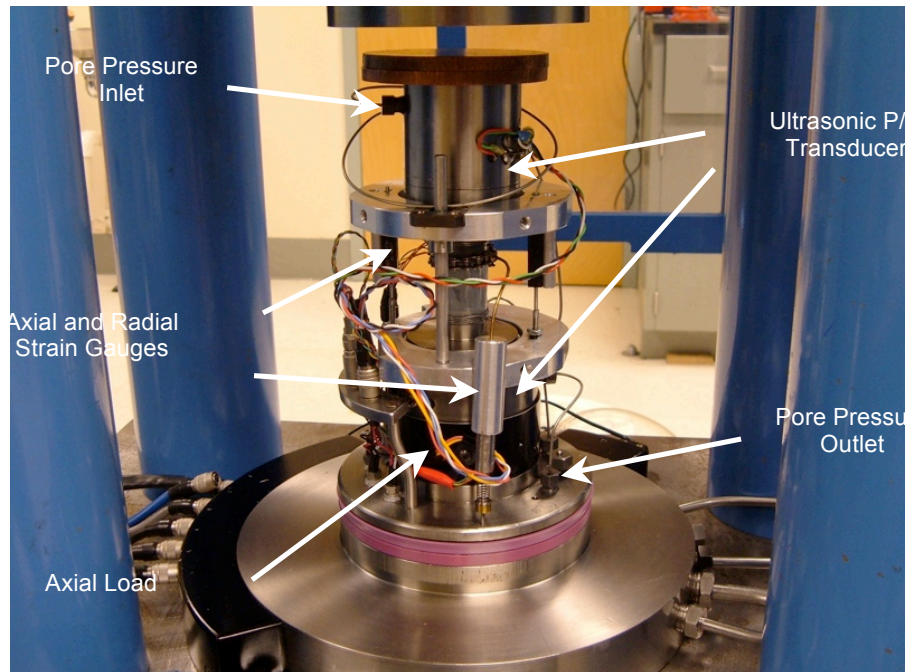


Figure 2: Photograph of the triaxial testing equipment used in the studies described in this report.

In an effort to establish a baseline set of measurements, we tried to isolate the effects of stress, pore pressure, temperature, moisture, and gas mixture by varying only one component of the system at a time. For all of the data shown below, measurements were carried out at room temperature, only single phase Helium or CO₂ was used as a pore fluid, and moisture and humidity were minimized. However, both pore pressure and effective stress were varied during experiments. Measuring permeability as a function of both pore pressure and effective stress is particularly important, as permeability can vary due to swelling/shrinkage (a function of pore pressure) and due to mechanical opening/closure of pathways (a function of effective stress).

Adsorption Isotherms

For general reference and internal verification of the isotherms reported by Tang *et al.*, we measured adsorption isotherms for both intact and powdered coal samples. Total adsorption isotherms (at 22°C) were determined for pure CO₂ using the volumetric method. Our results are shown in Figure 3. While our isotherms fall slightly below those measured in the lab of Tony Kovscek, given the difference in apparatus setups and innate heterogeneity of coal, we believe that a maximum of 15% error between the data sets provides a satisfactory match.

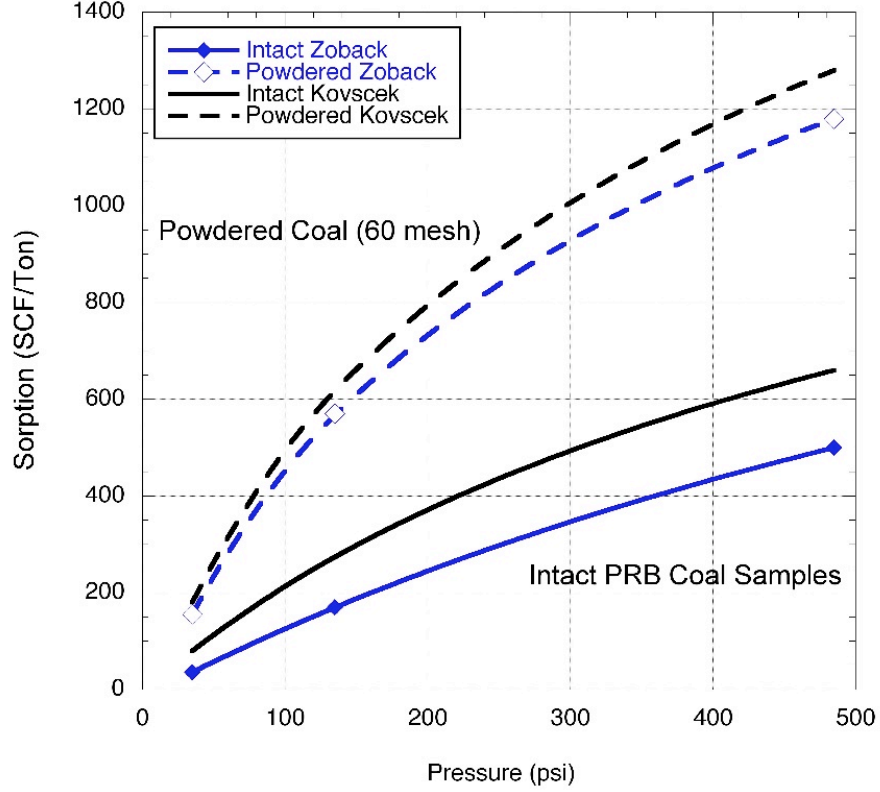


Figure 3: Total adsorption isotherm for powdered and intact coal samples from the Powder River Basin, Wyoming. Experiments performed at a temperature of 22 C. Blue curves show data from this study (“Zoback” in the legend). Black curves are shown for comparison, and are adapted after Tang *et al* (“Kovscek” in the legend).

Static and Dynamic Elastic Parameters

We measured the elastic stiffness of intact samples of PRB coal using two different methods. Static elastic parameters can be determined from a stress-strain curve. In general, the slope of the tangent of the stress-strain curve at a particular value of strain gives the elastic stiffness at that point. For example, bulk modulus can be calculated by plotting hydrostatic stress against volumetric strain. On the other hand, assuming that the sample is an isotropic, homogeneous medium, dynamic elastic parameters can be derived from measurements of ultrasonic velocities. At a particular value of stress or strain, the dynamic bulk modulus is given by:

$$K = \rho \left(V_p^2 - \frac{4}{3} V_s^2 \right), \quad (1)$$

where K is the bulk modulus, ρ is bulk density, V_p is the P-wave velocity, and V_s is the S-wave velocity. Note that for an isotropic, homogeneous elastic material, the static and dynamic measurements will produce identical values of bulk modulus.

For these tests, a series of loading cycles were performed, in which the confining pressure was increased to a target pressure at a rate of 6 MPa/hour, held constant for a period of 10 hours, and then decreased back to the initial pressure value. The pressure holds were used to test whether or not creep strain would occur; please see the section on creep strain below. Pore pressure was held constant during these tests. The samples were first saturated with Helium, and a series of loading cycles was performed. The samples were then unloaded to the initial conditions, and saturated with CO₂. The same series of loading cycles was then repeated. Stress and strain data were collected every 10 seconds. P and S wave velocities were captured every 60 seconds.

The results from these measurements are shown in Figure 4. There are several important details to note in this Figure. First, note that for the Helium-saturated case, the dynamic and static values of bulk modulus are nearly identical, indicating that the coal sample is elastic, which is the expected behavior. Interestingly, when the same sample is saturated with CO₂, the static bulk modulus decreases by approximately a factor of two, while the dynamic modulus increases slightly. This divergence in behavior suggests that the CO₂ is bearing some of the externally applied load, and is stiffening micropores while lubricating larger grain and maceral boundaries.

In order to verify the observed increase in dynamic bulk modulus with CO₂ saturation, we conducted a series of cyclic-loading experiments as a function of pore pressure. Because the stiffness of CO₂ increases with pressure, we expected the observed dynamic bulk modulus to increase with pore pressure. The results of these tests are shown in Figure 5, and as anticipated, dynamic bulk modulus increases with increasing pore pressure. While the increase is not large, an approximately 20% change in bulk modulus with a factor of four increase in pore pressure, it is observable.

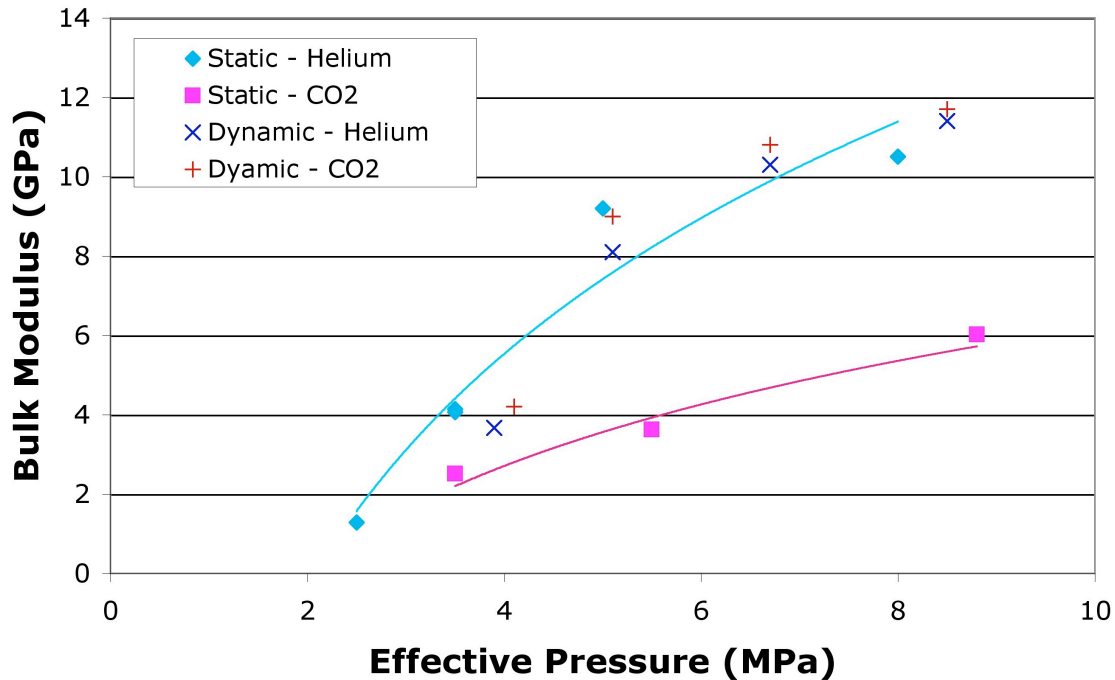


Figure 4: Static and dynamic bulk modulus plotted as a function of effective pressure for Helium and CO₂ saturated PRB coal samples. The pore pressure was kept constant at 1 MPa. Note that while the static bulk modulus decreases by a factor of two after being saturated with CO₂, the dynamic bulk modulus actually increases slightly.

Permeability of Intact and Powdered PRB Coal Samples

Klinkenberg-corrected measurements of Darcy-flow permeability are plotted as a function of effective stress in Figure 6. Please note that unlike most gas permeability measurements on coal, for these tests the pore pressure was held constant at 1 MPa, while the effective stress was increased. We implemented this experimental procedure because we are interested in understanding the effects of both adsorption and stress on permeability.

There are several things to note in Figure 6. For the reference data set collected using Helium, the observed decrease in permeability with increasing effective stress can be attributed to the mechanical closing of cleats and other pathways. Saturating the samples with CO₂ causes a decrease in permeability, regardless of effective stress, and can be thought of as a downward shift along the y-axis in this plotting space. Finally, the differences between the powdered and intact samples are interesting. Relative to the intact sample, the powdered sample has a higher initial permeability, a larger change in permeability with increasing effective stress, and a smaller decrease in permeability following CO₂ saturation. All of these observations are consistent with the fact that powdered sample has more porosity (30% vs. 10%) and is more compressible (by a factor of 2-3) than the intact sample.

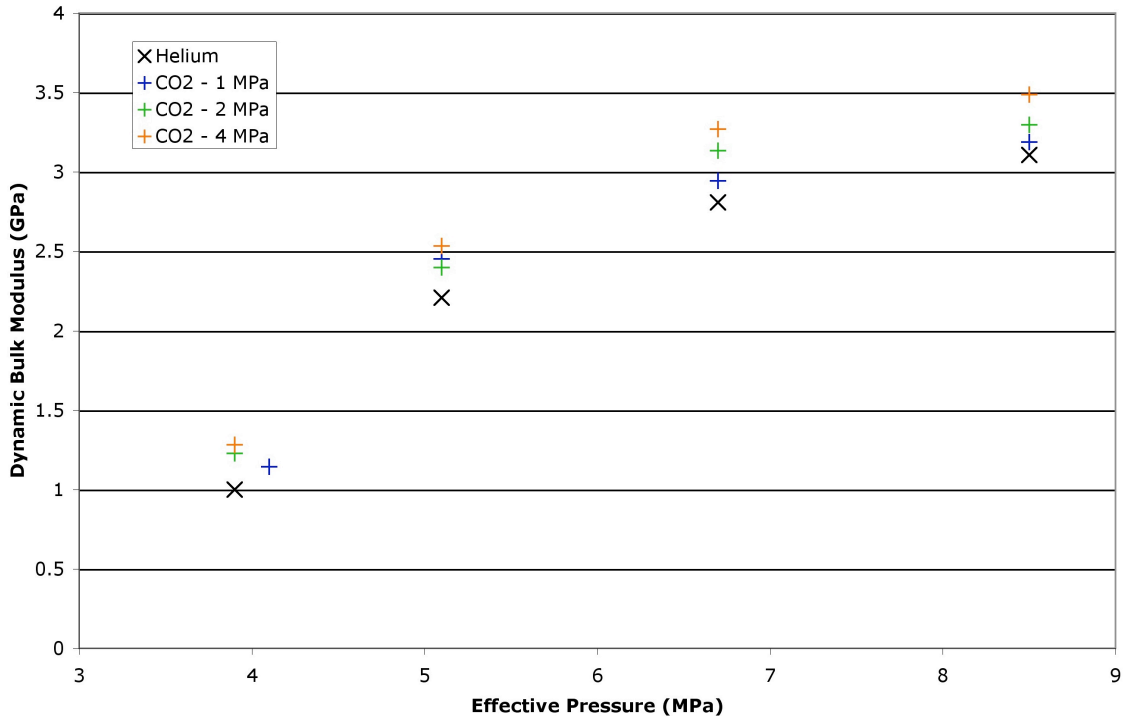


Figure 5: Normalized dynamic bulk modulus as a function of effective pressure for CO₂ saturated coal samples. Note that bulk modulus is observed to increase with pore pressure.

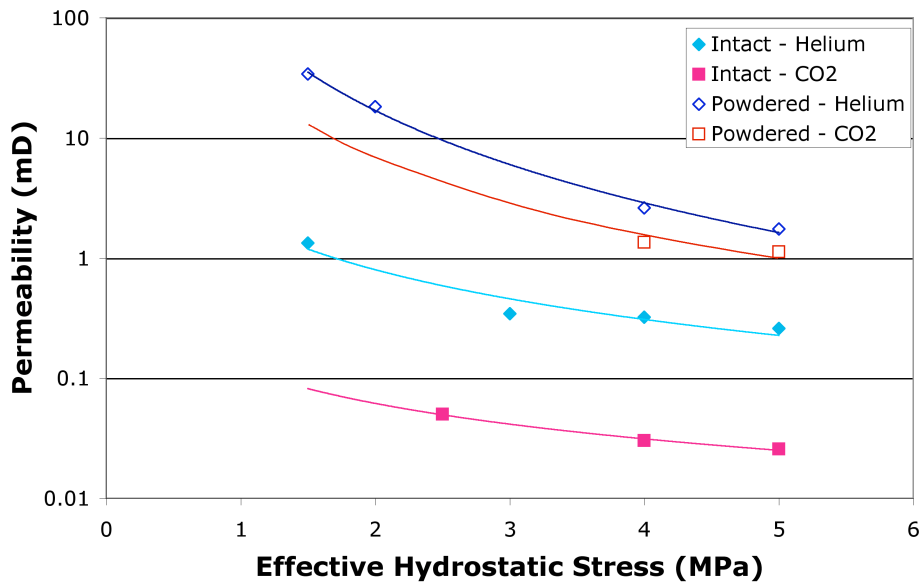


Figure 6: Gas permeability plotted as a function of effective hydrostatic stress for both powdered and intact PRB coal samples.

Measurements of Confined Swelling Strain

The decrease in permeability following CO₂ saturation suggests that the coal matrix is swelling in response to adsorption. Because we have been measuring permeability under hydrostatic loading conditions, we elected to measure volumetric swelling strain under the same boundary conditions, in an effort to make relating the two quantities easier. These swelling measurements are shown as a function of time in Figure 7, and as a function of pore pressure in Figure 8. In both figures, the effective hydrostatic stress is held constant at 1 MPa.

The swelling behavior as a function of time is interesting because the swelling strain can be seen to increase linearly at first, followed by a much more gradual asymptotic approach to the equilibrium swelling for a given pore pressure. These observations can be attributed to convective behavior while the CO₂ is saturating the macro-pore space and cleats, followed by diffusive behavior as the CO₂ slowly invades the matrix. As expected, swelling strain increases with adsorption, which in turn increases with pore pressure. While we do not currently have enough data to attempt any quantitative modeling of the adsorption and swelling, we plan to continue making swelling measurements in the future.

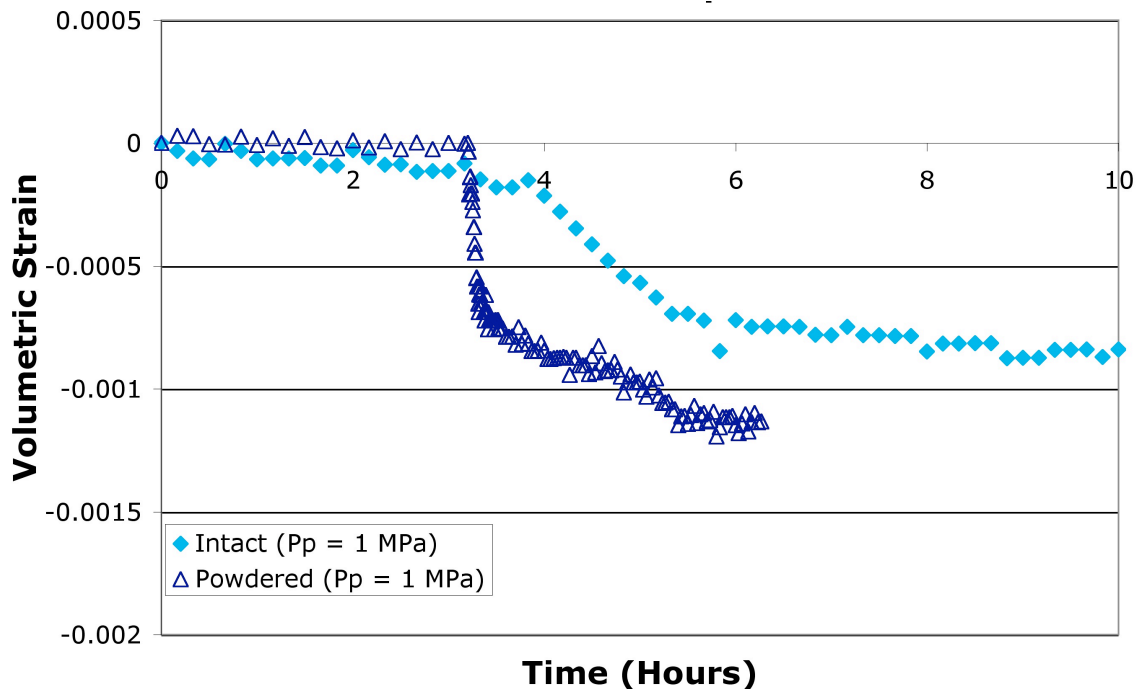


Figure 7: Volumetric swelling strain plotted as a function of time for powdered and intact PRB coal samples. Negative strain indicates swelling. The samples are initially saturated with Helium. At approximately 3 hours, the samples are flooded with CO₂ at constant pore pressure and effective hydrostatic stress.

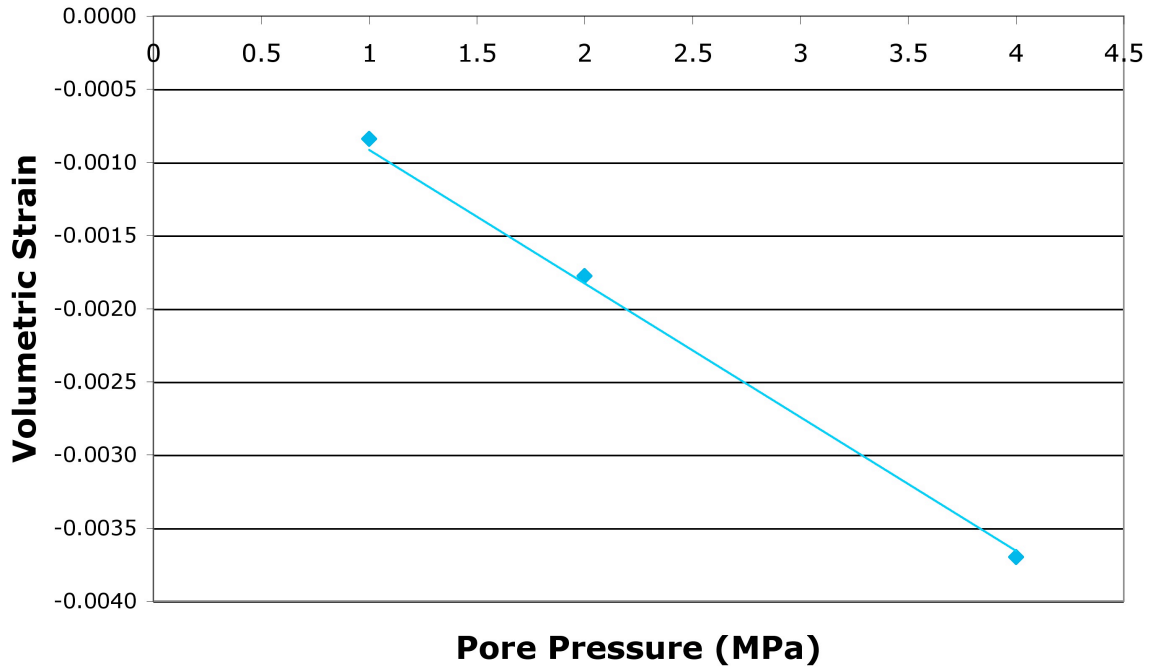


Figure 8: Volumetric swelling strain plotted as a function of pore pressure for intact PRB coal samples, at a constant effective hydrostatic stress of 1 MPa. The increase in swelling with pore pressure appears to be linear, but more data at higher pore pressures are needed to confirm this.

Observations of Creep Strain

During the cyclic-loading tests we conducted, we observed an interesting change in deformation behavior when the samples were saturated with CO₂. Specifically, even when the effective hydrostatic stress was held constant, the samples continue to deform. This time-dependent behavior is typical of materials that have a viscous component of deformation. Considerable work needs to be done to further understand this phenomenon. Our results to date are shown in Figure 9.

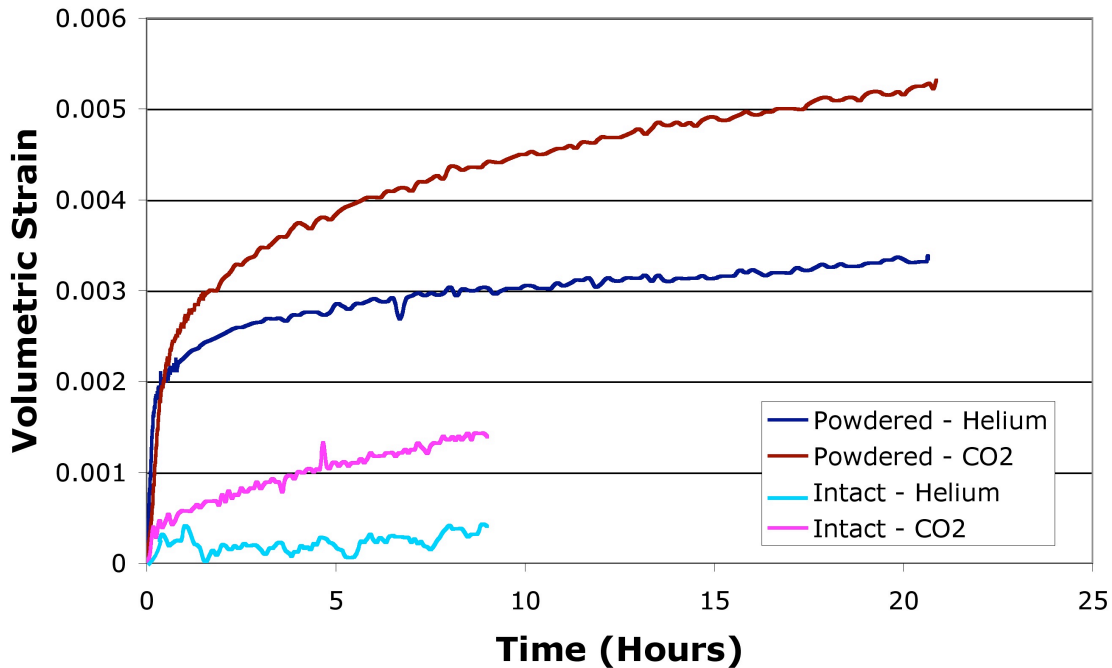


Figure 9: Volumetric creep strain plotted as a function of time for powdered and intact PRB coal samples, at a constant effective hydrostatic stress of 5 MPa. Notice that the intact, Helium saturated sample behaves elastically: there is no significant time-dependent strain. On the other hand, the intact, CO₂ saturated sample continues to deform as a function of time. The powdered samples show more complex behavior, but the CO₂-saturated sample still exhibits significantly more creep strain than the Helium-saturated sample.

Feasibility Assessment of CO₂ Sequestration and Enhanced Recovery in Gas Shale Reservoirs

Introduction

Near to medium-term CO₂ storage in oil and gas fields, unminable coal seams, and deep saline aquifers does not seem to be limited by total storage capacity. An IPCC report from 2005 found that worldwide geologic sequestration capacity is 675 to 900 GtCO₂ for oil and gas fields, 3 to 200 GtCO₂ for unminable coal seams, and >1000 GtCO₂ for deep saline aquifers [26]. Given the expense of capturing CO₂ at a point source, cost is the largest limiting factor in the near-term. Thus, it is most likely that large-scale CO₂ storage will be implemented in combined enhanced hydrocarbon recovery and sequestration projects in order to offset the capture and storage costs.

Oil reservoirs have been enhanced by CO₂ injection since the 1970's. Natural gas reservoirs, however, are not typical candidates for enhanced recovery because the free gas phase flows easily in a conventional reservoir. In some "unconventional" gas reservoirs, such as deep unminable coal seams and organic-rich black shales, methane (CH₄) is found both free within the pore and fracture space as well as adsorbed onto

internal solid surfaces. These unconventional reservoirs are candidates for enhanced recovery with carbon sequestration because in some cases CO_2 is preferentially adsorbed over CH_4 , allowing for increased production with secure carbon storage as the CO_2 displaces the CH_4 . The conceptual model for gas production in both coal beds and gas shale reservoirs is shown in Figure 10.

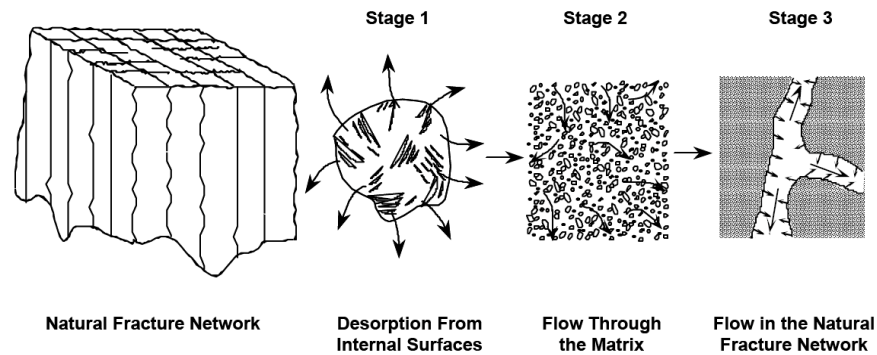


Figure 10: Conceptual model of gas production in shale and coal [27].

Enhanced recovery with CO_2 sequestration has been tested in the field for coal, but it has not yet been tested for gas shale reservoirs. Since gas shales and coals share similar properties, it is important to investigate if gas shales could also benefit from enhanced recovery with CO_2 . While shales by their nature do not have the porosity and permeability of typical petroleum reservoirs or saline aquifers, they may still be attractive targets for CO_2 sequestration. They are extensive in area and thickness (Figure 11), which is helpful in matching them with point sources of CO_2 .

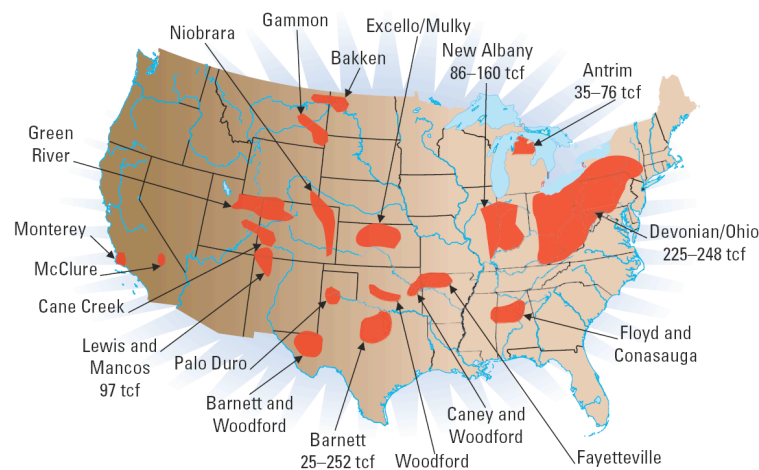


Figure 11: Map of extensive gas shale resources in U.S. [28].

Our work will test the feasibility of enhanced recovery and CO_2 sequestration in gas shale reservoirs using the Barnett shale in Texas as a case study. Based on the lessons learned from studies on ECBM as a starting point, we will perform an initial test of the concept by integrating laboratory experimentation, reservoir modeling, fluid flow

simulation, risk analysis, and economic assessment. These studies will provide a greater physical understanding of gas shale reservoirs as well as guide future investigations in enhanced recovery and CO₂ sequestration. Additional background on gas shales and details of our research plans can be found below.

Background

The Barnett lies at a depth of 6500 to 8500 feet, which is associated with formation pressures of 3000 to 4000 psi [29]. Net thickness of organic-rich shale layers is 50 to 200 feet, thickening towards the deeper eastern part of the formation [29]. Typical composition of the producing facies of the Barnett are 45% quartz, 27% illite, 8% carbonate, 7% feldspar, 5% organic matter, 5% pyrite, and 3% siderite [30]. Porosity is on average 4-5%, while permeability of the intact matrix is measured in the tens to hundreds of nanodarcies [29].

Like coals, Barnett shale samples exhibit adsorption of CH₄. A set of Langmuir isotherms for Barnett shales is shown below in Figure 12. This database did not reveal the composition for each sample, thus it is not possible to correlate the range of adsorption capacities with a property such as TOC. In general, adsorption in gas shales is believed to be a combination of adsorption in microporous organic material, typically kerogen, and adsorption on layered clays, such as illite. A linear relation between TOC and CH₄ adsorption capacity has been previously found for Appalachian and Antrim shales [31].

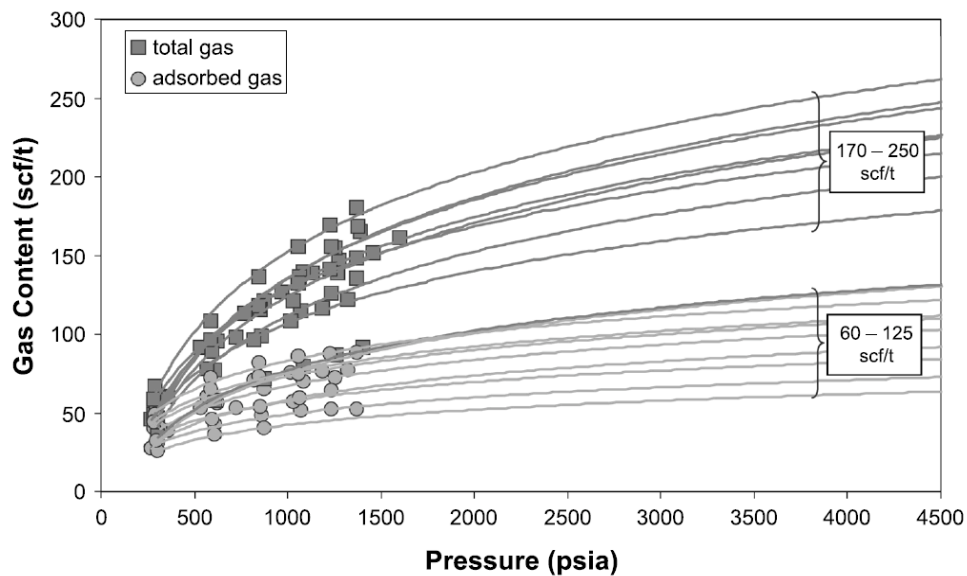


Figure 12: Methane adsorption isotherms for Barnett shale core samples [29].

Nuttall et al. is the only study that has tested the adsorption of CO₂ on gas shale samples. [31] They report that CO₂ is preferentially adsorbed at over five times the volume of CH₄ on average in organic-rich shales (Figure 13). They also find a linear correlation between TOC and CO₂ adsorption capacity (Figure 14). While adsorption studies of CH₄ have been conducted for Barnett shale reservoirs, no adsorption studies for carbon dioxide exist. Thus, it will be necessary to study the adsorption of CO₂ and CH₄

on Barnett shale samples in order to verify that a similar relation exists as was found for Devonian shale samples.

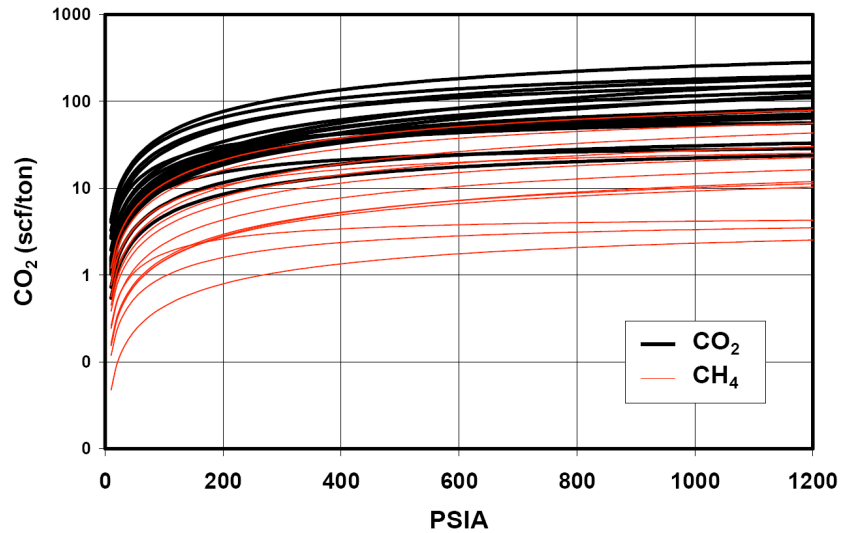


Figure 13: Preferential adsorption of CO₂ over CH₄ in Devonian shale samples [31].

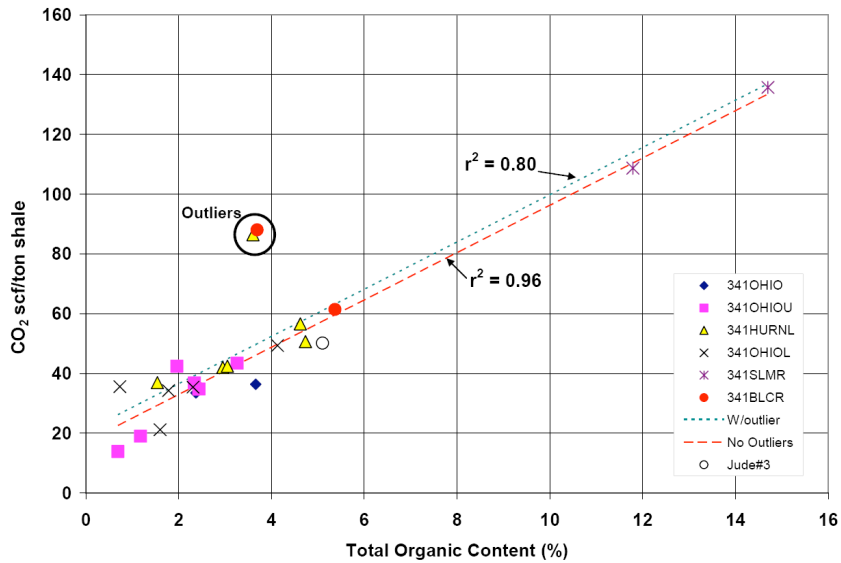


Figure 14: Relationship between Total Organic Carbon and CO₂ adsorption at 400 psi in Devonian shale samples. Linear trend of CO₂ adsorption capacity vs. TOC is consistent with linear trend found for methane [31].

In addition to adsorption properties, knowledge of the mechanical state of a gas shale reservoir is critical for optimal design of an enhanced recovery and CO₂ sequestration project. The in situ stress of the Barnett shale is in a normal faulting environment, with an overburden (S_v) gradient of 1 psi/ft but relatively isotropic horizontal stresses of about 0.7 psi/ft [32]. The development of hydraulic fracturing techniques has made the Barnett an economically viable natural gas reservoir. However, the geomechanical aspects of

hydraulic fracture stimulation in the Barnett are not well understood. Thus, mechanical studies on Barnett shale rocks as well as further research on the stimulation process in the Barnett will be crucial to understanding the potential for CO₂ sequestration and enhanced recovery.

Reservoir Model for Fluid Flow Simulation with Geomechanical Constraints, Teapot Dome, WY

Introduction & Background

Mature oil and gas reservoirs are attractive targets for geological sequestration of CO₂ because of their potential storage capacities and the possible cost offsets from enhanced oil recovery (EOR). This project investigates the feasibility of a CO₂ sequestration at Teapot Dome oil field, Wyoming, USA, with the objective of predicting the potential risk of CO₂ leakage along reservoir-bounding faults or through a potentially compromised caprock in the context of providing the technical foundation required for RMOTC and its partners to consider and design the CO₂-EOR injection project.

Teapot Dome is an elongated asymmetrical, basement-cored anticline with a north-northeast axis. It is part of the Salt Creek structural trend, located in the southwestern edge of the Powder River Basin. The Tensleep Formation in this area consist of interdune deposits such as eolian sandstones, sabkha carbonates, evaporates (mostly anhydrite), and some very low permeability dolomicrites. The average porosity is 0.10 ranging from 0.05-0.20. The average permeability is 30 mD, ranging from 10 – 100 mD. The average reservoir thickness is 50 ft. The reservoir has strong aquifer drive. In the study area, the Tensleep Formation has its structural crest at 1675 m. It presents a 3-way closure trap against a NE-SW fault to the north.

In previous stages of this project, the Tensleep Formation has been evaluated as the target horizon for a pilot CO₂ EOR-carbon storage experiment, in a three-way closure trap against a bounding fault, termed the S1 fault. A comprehensive geomechanical model for the Tensleep Fm. was generated yielding a Normal Fault - Strike Slip (NF/SS) present day stress state. The components of the stress tensor as well as the geometry of the fault were determined and subjected to a sensitivity analysis. It was established that in the most pessimistic scenario, in 99.9% of the cases at the depth of the Tensleep Fm. (the target horizon) approximately 9 MPa of excess pressure would be required to cause the S1 fault to reactivate. This value could be achieved by a CO₂ column height of approximately 1500 m. The average closure of the Tensleep Fm. structure in this area does not exceed 100 m. Therefore the S1 fault does not appear to be at risk of reactivation and therefore providing a leakage pathway for CO₂ under the present stress field. In a NF/SS present stress state, such as the one here, when the buoyancy pressure of the CO₂ equals the magnitude of the minimum horizontal stress (S_{hmin}) a vertical hydro-fracture will develop, therefore compromising cap-rock integrity. In order to reach the lower bound of the estimated S_{hmin} magnitudes, a CO₂ column height of approximately 1000 m would be needed, but since the structural closure is only 100 m, as stated before, it was estimated that caprock integrity is not a risk either.

Other potential paths for leakage could be minor faults and fractures present in the reservoir and caprock. It has been proposed that critically-stressed fractures (i.e. active) are permeable, therefore providing potential pathways for the CO₂ to leak [33, 34].

Tensleep Fractures at Teapot Dome

Several authors [37, 38, and 39] have described fractures in the Tensleep Formation, from cores, FMI logs and outcrops, as vertical to near vertical. In particular at Teapot Dome, Lorenz and Cooper [37] performed a fracture characterization in core samples where they found an average of 1 fracture every 5 feet, although with increase cement content, they noted an increase in fracturing. In high porosity sandstones they described a fracture intensity of approximately 10 fractures per foot, in dolomitic sandstones 3 fractures per foot and in heavily cemented fractures 1 fracture per foot.

These values correspond to a fractured reservoir and careful consideration must be given to the fractures to estimate their contribution to the risk of CO₂ leakage.

Results

Critically Stressed Fractures at Teapot Dome

Figure 15 shows the dominant sets of open fractures determined by Schwartz et al. [38] (yellow set) from FMI logs of five wells located approximately parallel to the axis of the anticline. Also in Figure 15 it is shown the preferred strike direction of natural fractures from FMI logs described by Lorenz [39] (red set).

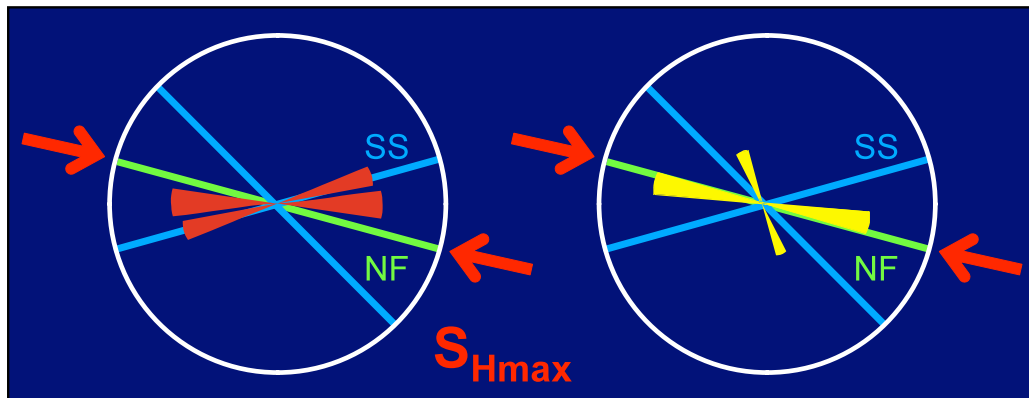


Figure 15: Strike orientation of main fracture sets in the Tensleep Formation from Lorenz [37] (left) and Schwartz et al. [38] (right).

Our previous geomechanical characterization yielded a NF/SS regime with a maximum horizontal stress (S_{Hmax}) direction of $\sim 116^\circ$ (red arrow in Figure 15). In a NF stress regime the optimal direction for slipping is parallel to S_{Hmax} (green line) whereas in a SS regime the optimal directions are 30° with respect S_{Hmax} (blue lines).

Comparing the strike of the main fracture sets described in the Tensleep Formation, with the critical directions, we can observe that at least three of these sets are parallel to

one of the optimal directions for slip. Figure 16 shows that the fracture sets a, b and c are very close to the critical pressure needed for reactivation. The presence of these minor faults enhances formation permeability and injectivity of CO₂. However, the potential for slip on these faults could potentially compromise the top seal capacity of the Tensleep if these minor faults extend up into the cap rock.

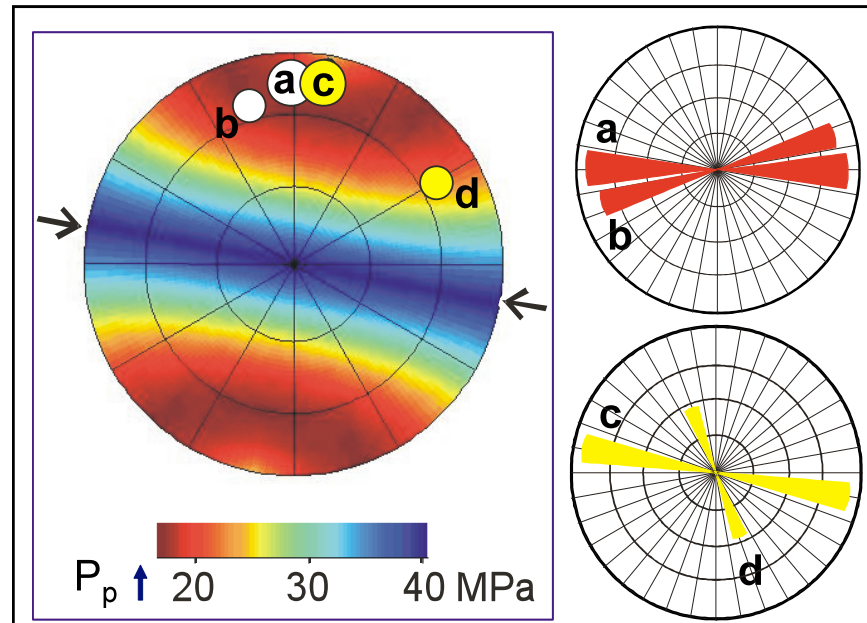


Figure 16: Rose diagram of the dominant fracture sets at the Tensleep Fm. (right) and the poles of these sets color-coded with the critical pressure needed to reactivate them (left). Note the black arrow in the bottom indicating the hydrostatic pore pressure (~16.5 MPa).

3D Stochastic Reservoir Model

We had developed a 3D reservoir model as input of a fluid flow simulation using geomechanical constrains with the objective of modeling the migration of the injected CO₂ as well as to obtain limits on the rates and volumes of CO₂ that can be injected without compromising seal integrity.

The Tensleep Fm. consists mainly of porous and permeable eolian-dune sandstones, interbedded with thin sabkha carbonates, minor evaporates (mostly anhydrite), and thin but widespread extensive beds of very low-permeability dolomicrites [40,41]. Figure 17 shows the schematic stratigraphic column of the reservoir and caprock following Yin [42] that we utilize to construct our reservoir model.

The geometry of the model was built utilizing time structure maps from the seismic volume, at the top of the Tensleep Fm. and at the top of the main producing interval B-Sand, as well as formation tops of the Minekhata Member, Opeche Shale Member, A-Sandstone, C-Dolostone, lower B-Sandstone and C-Dolostone from aproximatelly ~26 wells in the area.

We built a grid with axes of $\sim 3 \times 1.5$ km, with 10 layers, where each cells has an areal dimension of $\sim 50 \times 100$ m and a height varying from 1 to 12 m, depending on the horizon.

In order to account for the permeability anisotropy caused by fractures, described in the previous section, we oriented the grid blocks in a direction approximately parallel to the S_{Hmax} direction of approximately 116° (Figure 18).

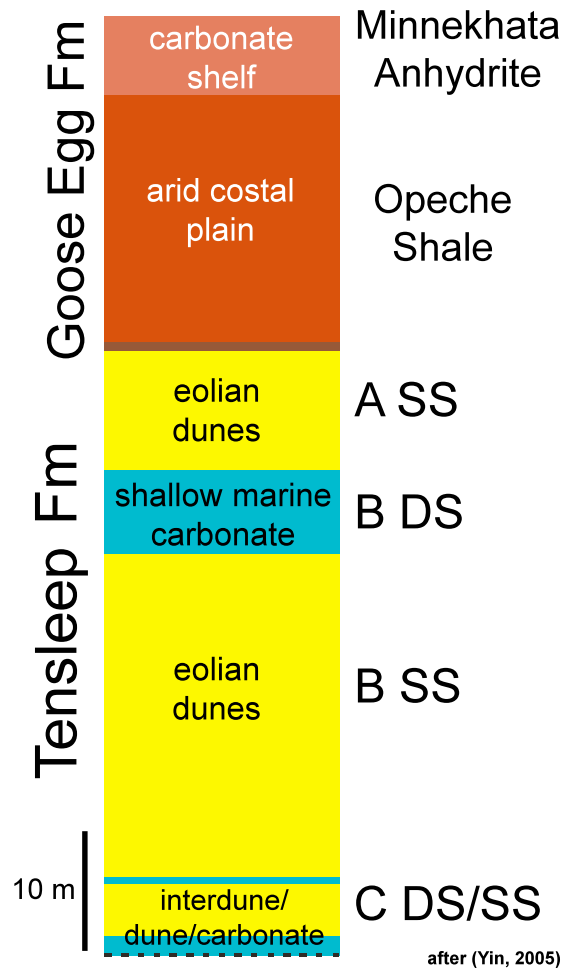


Figure 17: Schematic stratigraphic column of reservoir (Tensleep Fm.) and caprock (Goose Egg Fm.). SS = sandstone, DS = dolostone.

We used the sequential Gaussian simulation (SGS) method [43] to produce equally probable realizations of porosity and permeability that reflect the data variability and spatial statistics. Hard data from wells was incorporated in the interval where it existed, such as porosity data from density, neutron and sonic logs as well as from four cores. Soft data was incorporated as well, including porosity-permeability correlations from

core measurements, and porosity and permeability distribution from the reservoir lithofacies defined by Yin [44] for the Teapot Dome Tensleep Sandstone (see example in Figure 19). The spatial variability of the properties was incorporated into the SGS algorithm using semivariograms modeled considering the porosity distribution from well logs in each of the defined layers.

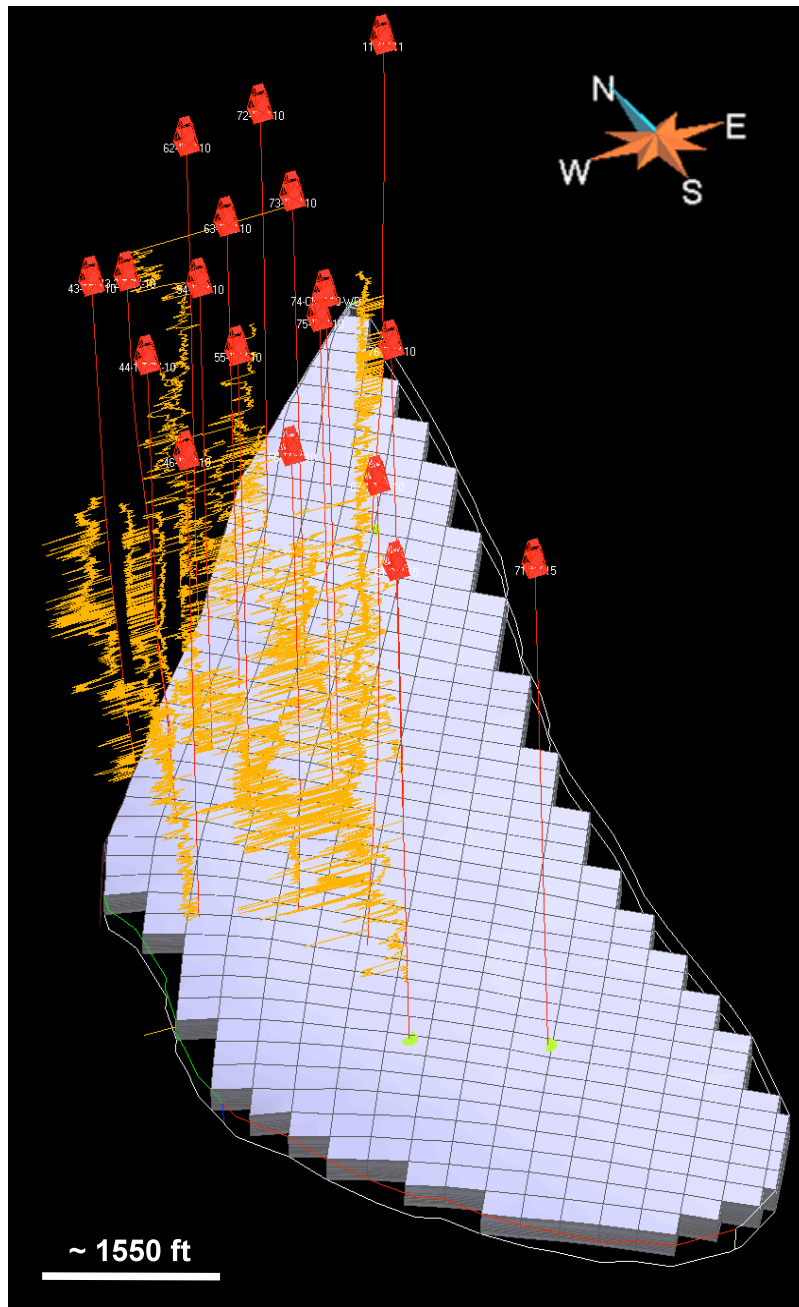


Figure 18: 3D grid built in Gocad [45] showing wells in the area and porosity logs.

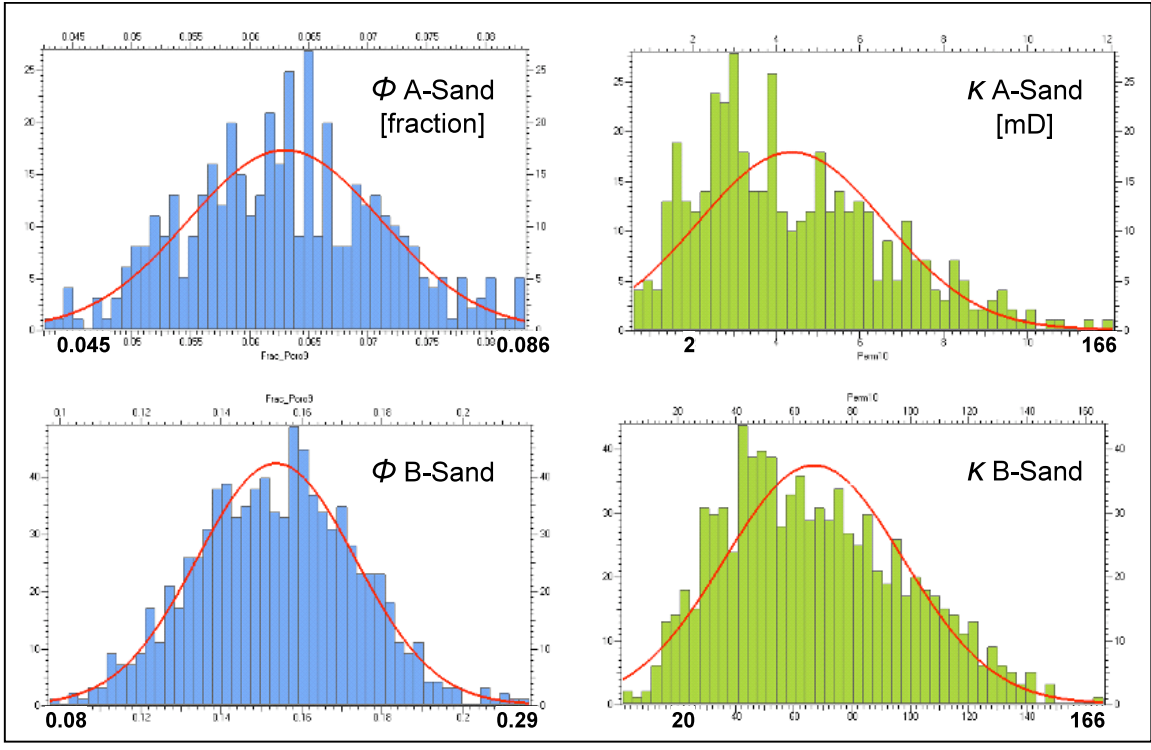


Figure 19: Example of porosity (blue) and permeability (green) geostatistical distribution for A-SS & upper B-SS intervals.

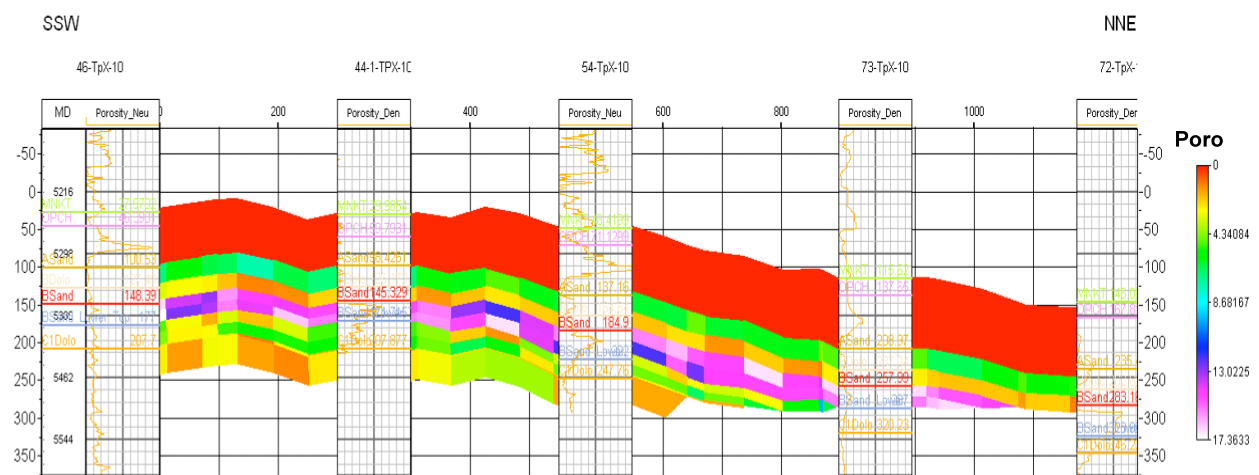


Figure 20: SSW – NNE Cross section showing the porosity distribution on the grid, porosity log, and well tops.

Induced Seismicity to Enhance Permeability in Low Permeability Saline Aquifers

Introduction & Background

Deep saline formations have great potential for geologic sequestration of CO₂. Such formations are widespread in many parts of the U.S. and in theory could easily be accessed from point sources of CO₂, such as power plants, factories, refineries, cement plants, etc. As typical of deep mature basins, many deep saline formations of the mid-continental U.S. appear to have low to moderate porosity and permeability compared to those encountered in large oil reservoirs, resulting in limited injectivity and storage capacities [46].

A demonstration CO₂ sequestration project has been carried out in the Michigan Basin, the Otsego County Test Site (Figure 21), as part of an ongoing project of the Midwest Region Carbon Sequestration Partnership (MRCSP), funded by the Department of Energy/National Energy Technology (DOE/NETL). Potential targets for sequestration include several Paleozoic reservoirs. In particular we focus on the Silurian Bass Island dolomite (BILD) at approximately 1050 m depth. The source for this project is the associated CO₂ removed from the Antrim Shale gas. It is separated at 6 centralized gas-processing plants in the Otsego and adjacent counties, which averages ~1.2 million metric tons per year. A preliminary simple fluid flow simulation indicates that under the present condition ~50% of this CO₂ could be stored in the BILD.

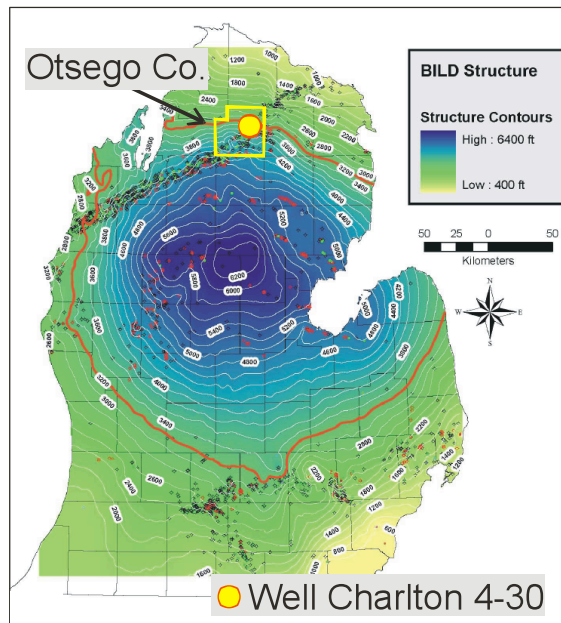


Figure 21: Structural map of Bass Island dolomite (injection interval) in Michigan. The yellow square indicates the Otsego County and the location of the test well Charlton 4-30 is indicated with the yellow dot. Modified from Barnes *et al.* [47].

For this reason, we proposed an injection-induced microseismicity stimulation experiment to enhance the permeability and injectivity of the target reservoir. Microseismic stimulation is initiated by increasing the fluid pressure thus reducing the effective normal stress on optimally-oriented faults and fractures triggering slip and creating high-permeability pathways within the reservoir. This technique is a frequent and safe practice for imaging hydraulic fracturing operations in the oil and gas industry and enhancing permeability in geothermal resources.

The field experiment consisted of injecting several hundred tonnes of CO₂ for forty days into the Bass Island dolomite (at well 4-30). Array of seismometers were deployed in two monitoring wells to record the induced events. The monitoring wells are the State Charlton C3-30, approximately 150 m (~500 ft) away at the injection depth and the State Charlton 2-30 at approximately 550 m away (Figure 22).

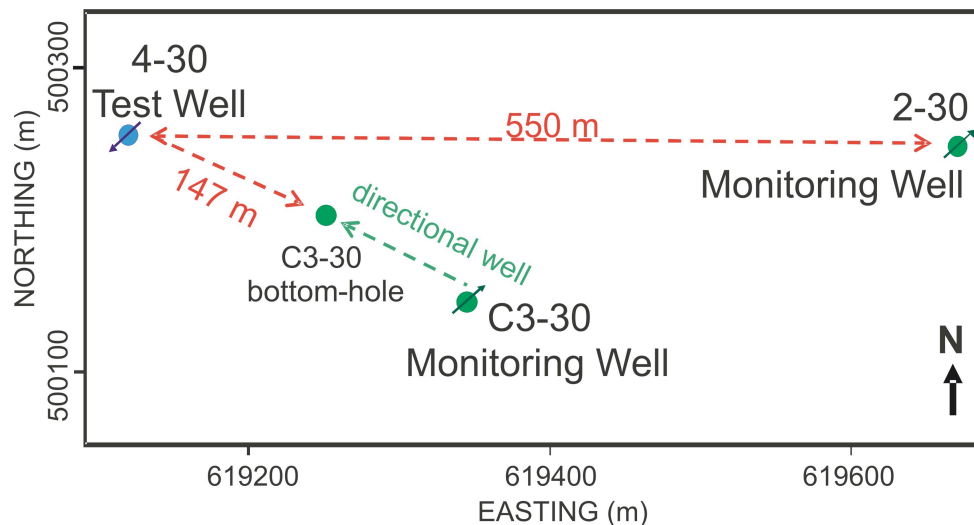


Figure 22: Experiment setup showing injection (4-30) and monitoring wells

Due to the very small magnitude (≤ 1) of the triggered events, they cannot be detected with surface seismometers and require a borehole array. Microseismic monitoring of this stimulation will provide valuable information on the resultant fluid-flow network of the reservoir.

Results

Geomechanical Characterization

We performed a preliminary geomechanical characterization analyzing FMI, density and sonic logs from the well State Charlton 4-30 and State Charlton 3-30 as well as a leak-off test and pore pressure measurements from wells in the vicinity.

The magnitude of the vertical stress (S_v) was obtained by integration of rock densities, taken from the density logs, from the surface to the top of the BILD (1048 m). The least principal stress, S_3 , which is usually the minimum horizontal principal stress (S_{hmin}), can be obtained from the analysis of hydraulic fracturing via either minifrac or

extended leak-off tests. Due to the lack of such data in the two mentioned wells we used the fracture gradients from a deep well in central Michigan described by Haimson [48]. The maximum horizontal stress (S_{Hmax}) magnitude was obtained by modeling wellbore failure features (drilling-induced tensile fractures in this case), as well as the magnitudes of S_v , S_{hmin} , pore pressure (P_p), and rock strength values.

The orientation of the horizontal principal stresses in a vertical well, the State Charlton 4-30, is determined from the drilling induced fractures orientations, since they propagate parallel to S_{Hmax} . Under normal drilling conditions, the occurrence of these drilling-induced tensile fractures (in a vertical well) usually indicates a strike-slip faulting stress state [49]. More than 80 drilling-induced tensile fractures were analyzed in the FMI log of well State Charlton 4-30 over a depth range of 580 – 1080 m and the average maximum horizontal stress (S_{Hmax}) direction obtained is $55^\circ \pm 10^\circ$ Az. This value is very consistent with the regional S_{Hmax} directions in the area, which are summarized in Figure 23.



Figure 23: Regional Stress map modified from Reinecker et al. [50]. The red arrow indicates the S_{Hmax} direction determined in the present study.

The rock strength used in the horizontal stresses magnitude estimations was determined from empirical relationships for carbonate rocks [51]. The BILD rock strength varies from 58 MPa to 72 MPa whether we use relationship 1 or 2 respectively.

$$UCS = 143.8 \exp(-6.95\phi) \quad (1)$$

$$UCS = 135.9 \exp(-4.8\phi) \quad (2)$$

In summary the analysis of the studied wells indicates a Strike Slip faulting stress state (see Figure 24) where $S_{Hmax} \approx 33$ MPa, $S_v = 26.6$ MPa, $S_{hmin} \approx 17.9$ MPa, and S_{Hmax}

orientation = $55^\circ \pm 10^\circ$. The pore pressure used in this analysis is $P_p = 10.8$ MPa, slightly over hydrostatic.

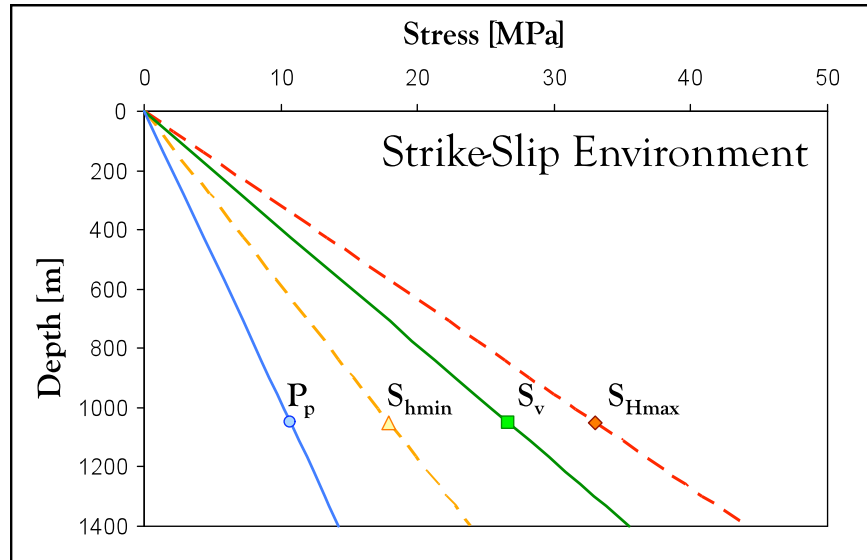


Figure 24: Stress summary plot for well State Charlton 4-30. At 1048 m depth (top of Bass Island dolomite): $P_p = 10.8$ MPa (blue dot), $S_{Hmax} \approx 33$ MPa (red diamond), $S_v = 26.6$ MPa (green square), $S_{hmin} \approx 17.9$ MPa (yellow triangle).

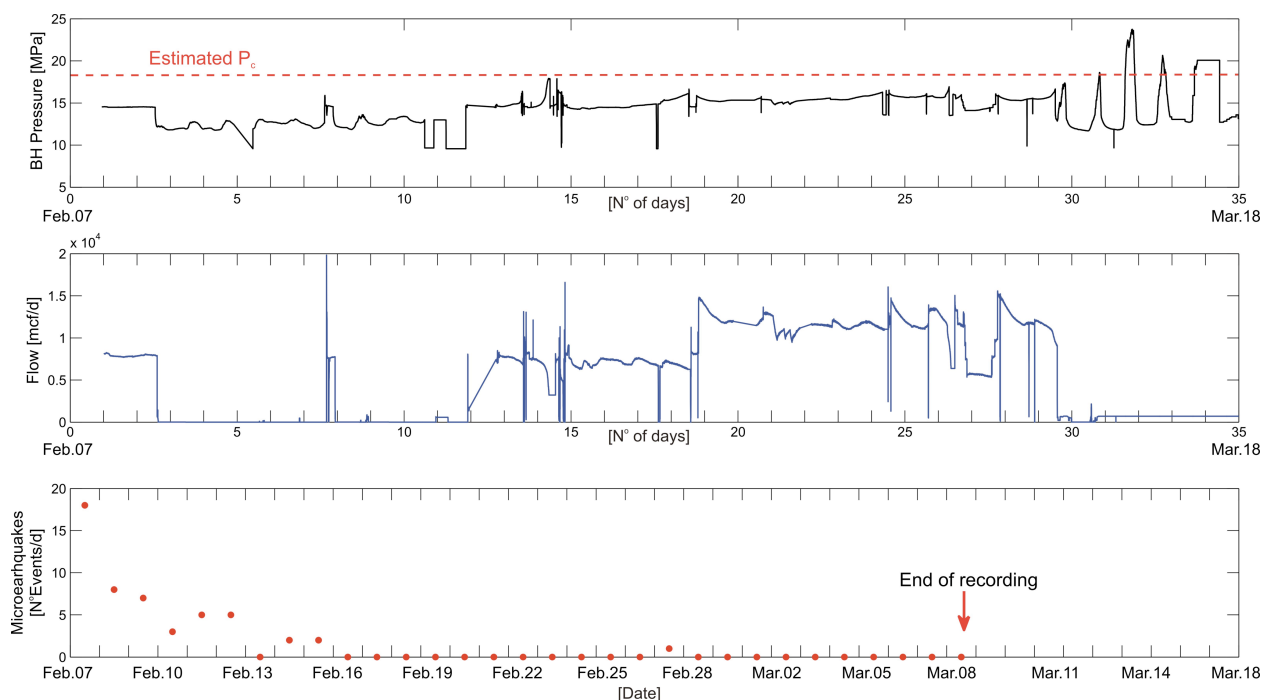


Figure 25: Preliminary estimated bottom hole pressure (top) and well head measured flow rate (middle) data at well 4-30; total number of events per day (bottom) recorded in the two monitoring wells.

Injection Experiment - Preliminary Data

The injection experiment consisted of injecting ~10,000 metric tons of supercritical CO₂ into the BILD over a period of 40 days. The microseismic monitoring lasted for the first 30 days. In Figure 25 we can observe the following preliminary data as a function of time: bottom hole pressure (estimated from well head pressure data), flow rate and total number of microearthquakes per day. At the time of writing of this report we are awaiting for the recorded bottom hole data and the final microseismicity report, which will provide us accurate location and times of occurrence of the events.

References

1. EIA, *Annual Energy Outlook 2007 with Projections to 2030*, DOE/EIA-0383, 2007. Available at [http://www.eia.doe.gov/oiaf/archive/aeo07/pdf/0383\(2007\).pdf](http://www.eia.doe.gov/oiaf/archive/aeo07/pdf/0383(2007).pdf)
2. Radovic, L.R., Menon, V.C., Leon, C.A., Kyotani, T., Danner, R.P., Anderson, S., and Hatcher, P., On the Porous Structure of Coals: Evidence for an Interconnected but Constricted Micropore System and Implications for Coalbed Methane Recovery, *Adsorption*, **3**, 221-232, 1997.
3. Metz, B., Davidson, O., de Connick, H. C., Loos, M., and Meyer, L. A. (eds.), *IPCC special report on Carbon Dioxide Capture and Storage*, Prepared by working group III of the Intergovernmental Panel on Climate Change, Cambridge University Press, Cambridge, 442, 2007. Available at <http://www.ipcc.ch/ipccreports/srccs.htm>
4. Reeves, S., Geological Sequestration of CO₂ in Deep, Unmineable Coalbeds: An Integrated Research and Commercial-Scale Field Demonstration Project, Paper SPE 71749, *presented at the*

- 2001 Annual Technical Conference and Exhibition, New Orleans, Louisiana, September 30-October 3, 2001.
5. Mavor, M.J., Gunter, W.D., and Robinson, J.R., Alberta: Multiwell Micro-Pilot Testing of CBM Properties, Enhanced Methane Recovery and CO₂ Storage Potential, *Proceedings of the SPE Annual Technical Conference*, Paper SPE 90256, Houston, Texas, 2004.
 6. Reeves, S., Taillefert, A., Pekot, L., and Clarkson, C., The Allison Unit CO₂-ECBM Pilot: A Reservoir Modeling Study, *Topical Report (DE-FC26-0NT40924)*, U.S. Dept. of Energy, February 2003.
 7. Winschel, R., Enhanced Coal Bed Methane Production and Sequestration of CO₂ in Unmineable Coal Seams, *presented at Coal-Seq V*, Houston, Texas, 2006.
 8. Van Bergen, F., Field Experiment of CO₂-ECBM in the Upper Silesian Basin of Poland, update with MOVECBM results, *presented at Coal-Seq VI*, Houston, Texas, April 10-11, 2008.
 9. Fujioka, M., Field Experiment of CO₂-ECBM in Ishikari Basin of Japan, *presented at Coal-Seq VI*, Houston, Texas, April 10-11, 2008.
 10. Connell, L., Detournay, C., Coupled Flow and Geomechanical Processes during CBM and ECBM, *presented at Coal-Seq VI*, Houston, Texas, April 10-11, 2008.
 11. Reeves, S., and Oudinot, A., The Allison Unit CO₂-ECBM Pilot, A Reservoir and Economic Analysis, *Proceedings of the International Coalbed Methane Symposium*, Tuscaloosa, Alabama, 2005.
 12. Sawyer, W.K., Paul, G.W., and Schraunfnagel, R.A., Development and Application of a 3D Coalbed Simulator, Paper CIM/SPE 90-119, *presented at the 1990 International Technical Conference of CIM/SPE*, Calgary, Canada, June 10-13, 1990.
 13. Law, D. H.-S., van der Meer, L. G. H., Gunter, W. D.: "Comparison of Numerical Simulators for Greenhouse Gas Storage in Coalbeds, Part IV; History Match of Field Micro-Pilot Test Data", prepared for the 7th International Conference on Greenhouse Gas Control Technologies, Vancouver BC, Canada, September 5-9, 2004.
 14. Harpalani, S., and Schraunfnagel, R., Shrinkage of Coal Matrix with Release of Gas and its Impact on Permeability of Coal, *Fuel*, **69**, 551-556, 1990.
 15. Kelemen, S.R., Kwiatek, L.M., Lee, A.G.K., Swelling and Sorption Response of Selected Argonne Premium Bituminous Coals to CO₂, CH₄, and N₂, *Proceedings of the International Coalbed Methane Symposium*, Tuscaloosa, AL, 2006.
 16. Harpalani, S., and Chen, G., Influence of Gas Production Induced Volumetric Strain on Permeability of Coal, *Geotechnical and Geological Engineering*, **15**, 303-325, 1997.
 17. Palmer, I., and Mansoori, J., How Permeability Depends on Stress and Pore Pressure in Coalbeds: A New Model, Paper SPE 52607, *SPE Reservoir Evaluation and Engineering*, **1**, 539-544, December 1998.
 18. Levine, J.R., Model Study of the Influence of Matrix Shrinkage on Absolute Permeability of Coal Bed Reservoirs, *Coalbed Methane and Coal Geology*, R. Gayer and I. Harris (eds.), Geological Society Special Publication No. 109, 197-212, 1996.
 19. USGS, Gas Desorption and Adsorption Isotherm Studies of Coals in the Powder River Basin, Wyoming and Adjacent Basins in Wyoming and North Dakota, *Open-File Report 2006-1174*, Reston, Virginia, 2006.
 20. Jessen, K., Tang, G-Q., and Kovscek, A.R., Laboratory and Simulation Investigation of Enhanced Coalbed Methane Recovery by Gas Injection, *Transportation in Porous Media*, **73**, 141-159, 2008.
 21. Robertson, E.P., Christiansen, R.L., Modeling Permeability in Coal Using Sorption-Induced Strain Data, Paper SPE 97068, *presented at 2005 SPE Annual Technical Conference and Exhibition*, Dallas, Texas, October 9-12, 2005.
 22. Mastalerz, M., Rupp, J.A., Melnichenko, Y., Radlinski, A., and Morse, D., Evaluating the Effects and Mechanisms of CO₂ sorption in Illinois Basin Coals, *presented at Coal-Seq VI*, Houston, Texas, April 10-11, 2008.
 23. Lin, W., Tang, G.-Q., Kovscek, A.R.: Sorption-Induced Permeability Change of Coal During Gas Injection Process. Paper SPE 109855 *presented at the SPE Annual Technical Conference and Exhibition*, Anaheim, CA 11-14 Nov. 2007.

24. Tang, G-Q., Lin, W., Chaturvedi, T., and Kovscek, T., A Laboratory Investigation of CO₂ Injection for Enhanced Methane Recovery for Coalbeds, *presented at Coal-Seq V*, Houston, Texas, 2005.
25. Ross, H., Zoback, M., and Hagin, P., CO₂ Sequestration and Enhanced Coalbed Methane Recovery: Reservoir Characterization and Fluid Flow Simulations of the Powder River Basin, Wyoming, *presented at GCEP Research Symposium*, October 1-3, 2007.
26. IPCC, Carbon Capture and Storage, Cambridge University Press, UK, 2005.
27. Zuber et al., A comprehensive reservoir evaluation of a shale reservoir – The New Albany Shale, Society of Petroleum Engineers Paper 77469, 2002.
28. Schlumberger, Shale Gas White Paper, 2007, http://www.slb.com/media/services/solutions/reservoir/shale_gas.pdf
29. Curtis, Fractured shale-gas systems, AAPG Bulletin, v. 86, no. 11, p. 1921-1938, 2002.
30. Montgomery, Barnett Shale: A new gas play in the Fort Worth basin, *Petroleum Frontiers*, vol. 20, no. 1 2004.
31. Nuttall et al, Analysis of Devonian black shales in Kentucky for potential carbon dioxide sequestration and enhanced natural gas production, Kentucky Geological Survey. 2005.
32. Palmer et al., Modeling shear failure and stimulation of the Barnett Shale after hydraulic fracturing” SPE Paper 106113, 2007.
33. Ross, H.E, CO₂ sequestration and enhanced coalbed methane recovery in unmineable coalbeds of the Powder River Basin, Wyoming, Ph.D. Thesis, Stanford University, 2007.
34. Reeves, The Allison Unit CO₂-ECBM Pilot – A Reservoir and Economic Analysis, International Coalbed Methane Symposium, 2005.
35. Townend, J., and M.D. Zoback, How faulting keeps the crust strong, *Geology*, 28 (5), 399-402, 2000.
36. Rogers, S., Critical stress-related permeability in fractured rocks. Fracture and in situ stress characterization of hydrocarbon reservoirs. M. Ameen. London, The Geological Society, 209, 7-16, 2002.
37. Lorenz, J. C., and S. P. Cooper, Analysis of fracture characteristics and distribution of 48-X-28 well: Rocky Mountain Oilfield Testing Center Report, 31 p., 2004.
38. Schwartz, B., T. H. Wilson, and D. H. Smith, Fracture pattern Dome, Wyoming, Eastern Section AAPG Abstracts with Program, September 18- 20, Morgantown, West Virginia, 2005.
39. Lorenz, J.C, Summary of Published Information on Tensleep Fractures, 2007: http://eori.uwyo.edu/downloads/Tensleep_FractureStudy1.doc
40. Friedmann, S.J.and Stamp, V.W., Teapot Dome: Characterization of a CO₂-enhanced oil recovery and storage site in Eastern Wyoming: *Environmental Geosciences*, v. 13, no. 3 (September 2006), pp. 181-199, 2006.
41. Zhang, Q., D. Nummedal, and P. Yin, Stratigraphy, sedimentology and petrophysics of the Tensleep Sandstone at Teapot Dome and in outcrop: Rocky Mountain Section AAPG Annual Meeting Abstracts and Program, Jackson, Wyoming, 2005.
42. Yin, P., Characterization of Tensleep Sandstone reservoirs: Rocky Mountain Section AAPG Annual Meeting Abstracts and Program, Search and Discovery article 50024, 2005: <http://www.searchanddiscovery.com/documents/2005/yin2/images/yin2.pdf>
43. Isaaks, E. H., The application of Monte Carlo methods to the analysis of spatially correlated data: Ph.D. thesis, Stanford University, Stanford, California, 213 p., 1990.
44. Yin, P., 2005b <http://www.searchanddiscovery.com/documents/2005/yin2/images/yin2.pdf>
45. Earth Decision - Gocad 2.1.6 Software
46. Lucier, A., Zoback, M.D., Gupta, N. and Ramakrishnan, T.S., Geomechanical aspects of CO₂ sequestration in a deep saline reservoir in the Ohio River Valley region: *Environmental Geosciences*, 13 (2), 85–103, 2006.
47. Barnes, D.A., Wahr, A., Harrison, W.B. III, Grammer, G.M., and Gupta, N., in press Geological Carbon Sequestration Potential in Devonian Saline Aquifers of the Michigan Basin, AAPG/EMD/DEG Special Publication on Geological Sequestration of CO₂.
48. Haimson, B.C., Crustal Stress in the Michigan Basin: *Journal of Geophysical Research*, 83, 5857-5863, 1978.
49. Zoback, M.D., Barton, C.A., Brudy, M, Castillo, D.A., Finkbeiner, T., Grollimund, B.R., Moos, D.B., Peska, P., Ward, C.D. and Wiprut, D.J., Determination of stress orientation and magnitude

- in deep wells: International Journal of Rock Mechanics and Mining Sciences 40, 1049-1076, 2003.
50. Reinecker, J., Heidbach, O., Tingay, M., Sperner, B. & Müller, B., The 2005 release of the World Stress Map, 2005 (available online at www.world-stress-map.org).
 51. Chang, C., Zoback, M.D. and Khaksar, A., Empirical relations between rock strength and physical properties in sedimentary rocks: Journal of Petroleum Science and Engineering 51, 223-237, 2006.

Gas Sorption and Coal Permeability

Our study has two features. First, laboratory experiments measured the change of the permeability of coal samples as a function of pore pressure and injected gas composition at constant effective stress. Second, adsorption solution theory described adsorption equilibria and aided interpretation. The gases tested include pure methane (CH₄), nitrogen (N₂), and carbon dioxide (CO₂), as well as binary mixtures of N₂ and CO₂ of different composition. The coal pack was initially dry and free of gas, then saturated by each test gas at a series of increasing pore pressures at a constant effective stress until steady state. Thus, the amount of adsorption varied while the effective stress was held constant. Results show that (i) permeability decreases with an increase of pore pressure at fixed injection gas composition and (ii) permeability change is a function of the injected gas composition. As the concentration of CO₂ in the injection gas increases, the permeability of the coal decreases. Pure CO₂ leads to the greatest permeability reduction among all the test gases. However, 10% to 20% by mole of N₂ helps to preserve permeability significantly. According to the mixed-gas adsorption isotherms, adsorption and the selectivity of a particular gas species on coal surfaces is a function of pressure and the gas composition. Therefore, we conclude that loading coal surfaces with adsorbed gas at constant effective stress causes permeability reduction. Finally, gas adsorption and permeability of coal are correlated simply to extend the usefulness of study results.

Introduction

Contrary to conventional natural gas resources in sandstone reservoirs that exist mainly as free gas in the pore spaces, gas in coal beds exists in the coal seams mainly as an adsorbed layer on the internal coal surface. Coal beds are known as a naturally fractured, dual porosity/permeability system, consisting of primary and secondary storage and mass transfer systems [1], Fig. 1. The primary porosity system (PPS) refers to the pore space in the coal matrix. It accounts for the majority of the coal bed porosity, and contains the vast majority of the gas-in-place volume. Thus, the coal matrix contains the majority of the adsorbed gas in coal beds. The secondary porosity system (SPS) refers to the natural fractures/cleats in the coal beds. Studies of some coals from the San Juan Basin show that “the coals comprise closely spaced (0.3 - 1 mm apart), wide (10 - 60 mm) cleats with narrow (5 - 20 mm wide) microcleats in between, all of which are open and non-partially mineralized”. [2] The free gas in coal beds resides in the fractures/cleats and large pores in the coal beds. The fracture/cleat system is the major contributor to permeability for fluid flow in coal beds.

Primary techniques typically recover less than half of the methane resource in a coal bed. [3] Also, primary methods have the disadvantage of producing significant water, potentially causing environmental problems and a drop of the local water table. Injecting N₂ and/or CO₂ increases the ultimate recovery of coal bed methane. [3,4] Such gas injection processes are referred to as enhanced coal bed methane recovery (ECBM). N₂-

and CO₂-ECBM processes engender different recovery mechanisms. With the injection of N₂, the partial pressure of methane in the coal seams decreases. Accordingly, methane desorbs from the coal surface and is driven to production wells by the injected N₂. Nitrogen is used as an injection gas mainly because of the availability of N₂ in the atmosphere. However, anthropogenic carbon dioxide leads to the extra benefit of sequestering CO₂ in coal beds. Carbon dioxide adsorbs to coal preferentially with respect to methane. Thus, injecting CO₂ in coal beds results in desorption of methane and storage of CO₂ in the coal beds. The estimated worldwide CO₂ storage capacity of coal beds ranges from 225 to 964 Gt (giga tons).[5,6]

The permeability of coal beds evolves during primary and ECBM operations. It is believed that two factors induce evolution of coal bed permeability.[7] The first is the change of effective stress,[8] and the second is gas sorption, either adsorption or desorption, Fig. 1. For example, the change of permeability during the primary recovery process is the result of two competitive effects. First, as pore pressure decreases under a constant overburden pressure, the effective pressure increases and permeability decreases due to fracture/cleat compression, i.e. closure of the fractures/cleats, Fig.1 (a). Permeability of the coal bed decreases. Second, as the pore pressure decreases, methane desorbs from the matrix of the coal bed causing shrinkage of the matrix and opening of cleats, Fig. 1(b). Permeability of the coal bed increases. During CO₂ -ECBM, the replacement of CH₄ with CO₂ causes expansion of the coal matrix and a decrease in the coal bed permeability.

Experimental

We investigate coal pack permeability as a function of gas sorption at constant effective stress by conducting gas-flow experiments through a coal pack at varying pore pressure, hence, different total gas adsorption. A constant difference between overburden and pore pressure means no change in the effective stress and eliminates the role of stress on the permeability change for this portion of our work.

The experimental apparatus is illustrated schematically in Fig. 2. The apparatus includes two high pressure gas vessels for injected gas and overburden pressure supply, a coal holder system, a pressure regulator for measuring the pressure drop across the coal pack and a flow meter for measuring the gas flow rate. A soap bubble flow meter verifies effluent rate measurement.

The heart of the setup is the coal holder system (Fig. 2). Dry ground coal, or a composite coal core, was packed tightly into a rubber sleeve surrounded by a second perforated aluminum sleeve. Ground coal was compacted to form a semi-consolidated porous medium. A coal pack instead of a coal core was used at first because of the difficulty to drill a core out from the highly fractured, fragile coal samples. A coal pack is a simplified uniform and homogeneous model of a real coal bed consisting of matrices and fractures. Gas sorption occurs mainly in the matrices of coal beds. A coal pack is

similar to a coal matrix, and enables us to investigate the permeability evolution without the need to address fractures at the very beginning of the study.

The permeability and porosity of the ground-coal pack were 36 md and 0.21 , respectively, and assumed to be uniformly distributed. The aluminum sleeve is perforated to allow confining pressure to be exerted uniformly on the coal pack. There was a second larger aluminum sleeve that covered the coal pack and formed an annulus to hold the overburden pressure supplied by high-pressure nitrogen.

The ground coal is identical to Powder River Basin samples employed in our previous study.[9] The coal originates from a coal bed at a depth of $900 - 1200 \text{ ft}$ below the ground surface. Average in-situ pressure[10] and temperature[11] are estimated between 2480 to 3450 kPa (360 to 500 psi) and 28 to $32 \text{ }^\circ\text{C}$. The coal sample as received was not preserved at formation conditions, was extensively fractured and broken into small pieces, filled with formation water, and contained some clay or shale. The small size of intact pieces precluded the use of core samples. The large shale pieces were removed and the coal was ground to a particle size of about 60 mesh . This exposed the internal surface area of the coal. The ground samples were preserved in desiccators under vacuum to avoid surface oxidation. The mean size of the coal particles was 0.25 mm .

Figure 3 presents the pure component sorption isotherms measured previously for this sample.[9] Measurement details are available in the original reference. Note that the CO_2 adsorbs more strongly than CH_4 that in turn adsorbs more strongly than N_2 . This sample also displays characteristic hysteresis among adsorption and desorption isotherms.

Coal plugs were cut from a second sample from the Powder River Basin also from the Wyodak-Anderson coal zone. Three coal plugs that were each 7 cm in length and 2.8 cm in diameter were butted end to end to form a composite core. The core was vacuumed at $30 \text{ }^\circ\text{C}$ to evacuate the moisture content ($S_{wi} = 0$). The permeability to helium was 1.7 md and the porosity was 0.07 . As the low permeability attests, the degree of open communicating fractures in the flow direction was minimal.

Experiments were performed at a series of increasing pore pressures and constant effective stress for different gas compositions. First, the coal sample was saturated overnight with gas at a given pore pressure. After that, the gas injection was shut in and the system was held static for more than 2 hours to make sure that equilibrium was achieved. The test gas flowed through the coal pack at different pressure gradients with the flow rate and the pressure gradient recorded when steady flow rate was reached. Permeability of the coal pack to gas was calculated according to the compressible form of Darcy's Law,

$$k_g = \frac{2000\mu_g q_a p_a L}{A[(p_1 + p_2)(p_1 - p_2)]} \quad (1)$$

where, k_g is the coal permeability to gas in md , μ_g is the gas viscosity in cp , q_a is the gas flow rate at atmosphere pressure in cm^3/s , P_a is the standard atmospheric pressure in atm , L is the length of the coal pack in cm , A is the cross sectional area of the coal pack in cm^2 , P_1 and P_2 are the inlet and outlet pressure of the coal holder in atm . Standard error propagation of the most significant experimental uncertainties (flow rate and pressure drop) shows that the range of uncertainty in permeability measurements is roughly 5%.

The pore pressure was then increased and the gas injection process and the permeability measurement repeated. The range of the pore pressure in the experiments was 50 to 1100 psi . Six to nine pressure points were selected for each gas composition. The overburden pressure was changed correspondingly to the pore pressure to ensure that the effective stress was always 400 psi . After finishing with one gas composition, the coal pack was vacuum evacuated and another gas was tested. The compositions of the injection gases used in the experiments were pure CH_4 , pure N_2 , pure CO_2 , 25% CO_2 + 75% N_2 , 50% CO_2 + 50% N_2 , 75% CO_2 + 25% N_2 , and 85% CO_2 + 15% N_2 binary mixtures. For the pure gases, bottled, bone-dry, high purity gases were used. The CO_2 and N_2 mixtures were made in the lab from the high purity gases according to partial pressure and mass. The temperature was constant at room temperature (22 $^{\circ}C$) for all experiments.

Results

The results of the experiments on ground coal samples are shown compactly in Fig. 4. The figure plots permeability versus pore pressure. Pore pressure is always increasing. Experimental data points and the fits to the permeability reduction trends are plotted on the same figure. All the data for different gas compositions were fit to an exponential curve:

$$k = k_0 p^b \quad (2)$$

where k_0 is the initial permeability of the coal pack measured using helium at atmospheric pressure. The value of the exponent, b , the minimum value of k/k_0 , and the average relative error for the curve fit are shown in Table 1. All of the average relative errors for the curve fit are less than 10%, except for the pure CO_2 case. In fact, the plot shows a fairly good curve fit for the CO_2 data. The high average relative error for pure CO_2 is due to the small absolute value of the permeability.

Figure 4 shows that the permeability of the coal pack decreases as the pore pressure increases for all gas compositions. The permeability decreases with pressure are more significant at pressures below 150 psi . The degree of permeability change is a function of the gas composition. The permeability reduction is negligible for pure N_2 , greater for pure CH_4 and the greatest for pure CO_2 . Consistent results were observed for the N_2/CO_2 binary mixtures. As the CO_2 concentration in the mixture increases, the permeability

reduction is greater. These results are consistent with the experimental adsorptions such as those shown in Fig. 3. As the pressure increased, the amount of adsorption increased of pure N₂, CH₄, and CO₂. Additionally, CO₂ was more strongly adsorbed on coal surface in comparison to CH₄ and N₂.

From the results of the permeability and adsorption experiments, it is concluded that as the amount of gas adsorbed increased, the permeability decreased. More of the pore space was occupied by adsorbed gas as pressure increased. Therefore, the permeability decreased with the increase of pore pressure, at a constant effective stress. At the same pore pressure, as the fraction of CO₂ increases in the injected gases, there is an increasing amount of gas adsorbed, which caused greater permeability reduction.

Note that the permeability did not change drastically for the gas mixtures where CO₂ concentrations were 25%, 50% and 75%, whereas the permeability changed dramatically for the mixture of 85% CO₂. Therefore, some nitrogen concentration in the injection gas (around 25% for the coal pack used in the experiments) helps to preserve the permeability, thus injectivity, during ECBM.

Additional permeability measurements were conducted on whole cores as a counterpoint to the significant permeability changes reported in Fig. 4. We concentrated on pure CH₄ and CO₂ results and explored the role of hysteresis on coal permeability. Results are presented in Figs. 5 and 6 for CH₄ and CO₂, respectively. Similar to the ground coal experiments, the pore pressure was increased step wise and the system allowed to reach steady state. Once a pressure of about 800 psi was achieved, pore pressure was decreased and the system again allowed to reach steady state.

The role of sorption hysteresis is apparent in both Figs. 5 and 6. As pressure is decreased, the coal surface does not release gas as readily as it was adsorbed, Fig. 3. Thus, the permeability versus pressure during desorption remains below the curve for adsorption until pressure is quite low. The most notable results, however, are the degree of permeability reduction for CO₂ in coal. In the ground coal experiments, the permeability reduced to one hundredth of the initial permeability at moderate pressure. In Fig. 6, the permeability of the composite coal core reduced to one tenth of the initial permeability. The initial permeability and porosity of the composite coal core are smaller than the coal pack, 36 *md* v.s. 1.7 *md*, and 0.21 v.s. 0.07. These differences in the evolution of permeability may be related to different adsorption and/or geomechanical properties of powdered versus intact coal samples. More study of intact, unground coal samples is clearly warranted.

Gas Adsorption on Coal

The experimental results showed that, the permeability of the coal pack decreased as the pore pressure increased at constant effective stress, for all of the gas compositions tested, Fig. 4. Another observation is that as the pore pressure increased, the total adsorption increased.[9] These observations lead us to correlate permeability reduction

with the amount of adsorption. It is thus necessary to consider multicomponent adsorption as described next.

Gas adsorption is a complex process. Knowledge and prediction of the competitive adsorption of gases on coal surfaces is important to understand the mechanisms of enhanced coal bed methane recovery, and to design CO₂ sequestration in coal beds to maintain acceptable permeability. In the literature, many numerical isotherm models were developed to describe gas adsorption on solid. Those isotherms use three different approaches: the Langmuir, occupied site approach, the Gibbs, multicomponent equilibrium approach, and potential theory.[12] The Langmuir approach is based on the model that the coverage of a surface is related to the equilibrium among occupied and available sites. The partial molar Gibbs free energy approach equates the chemical potential for each component in the adsorbed solution and the vapor phase at equilibrium. And the potential theory views the adsorption system as a gradual concentration of gas molecules towards the solid surface due to a potential field. The Langmuir and extended Langmuir isotherm[12], ideal adsorbed solution model[13], and real adsorbed solution theory[13,14] are among the most popular adsorption isotherms.

Langmuir and Extended Langmuir Isotherms: Among the numerous isotherms, the isotherm based on the Langmuir approach is the most widely used. The amount of pure gas adsorbed is calculated by the Langmuir equation:

$$v = \frac{v_m B p}{1 + B p}, \quad (3)$$

where v is the standard state volume of the adsorbed gas in SCF/t , v_m is the maximum amount of adsorption in SCF/t , B is the Langmuir constant in psi^{-1} , and P is the adsorption pressure.

For gas mixtures, the extended Langmuir equation is

$$v = \frac{v_{mi} B_i P_i}{1 + B_i P_i}, \quad (4)$$

where i represents component i , and P_i is the partial pressure of component i . Tang et al[9] showed that the Langmuir isotherm adequately modeled pure gas adsorption for the Powder River Basin coal samples used in this study. Arri et al. concluded that the extended Langmuir isotherm provided a reasonable correlation of the experimental data for mixed-gas adsorption[15].

Ideal Adsorbed Solution Model: The ideal adsorbed solution (IAS) model is another model used to calculate the amount of adsorption of gas mixtures from known isotherms of pure components. It is assumed that all of the adsorption sites have the same heat of

adsorption and that a modified form of Raoult's law, Eq. (5), is valid. Thus, the adsorbed solution is assumed to be ideal and described by

$$py_i = p_i^0 (\Pi)x_i, \quad (5)$$

where y_i is the mole fraction of component i in the free gas phase, x_i is the mole fraction of component i in the adsorbed solution, Π is spreading pressure, and p_i^0 is the equilibrium pressure for pure component i adsorption corresponding to the solution spreading pressure Π . Using the IAS model, the moles of the adsorbed gases are calculated by solving a set of seven equations and seven unknowns, given the knowledge of the adsorption pressure, the gas phase composition, and the parameters for pure gas adsorption[12]. Myers and Prausnitz [13] showed that the results calculated using this model had good agreement with experimental data for gases at moderately low pressure.

Real Adsorbed Solution Model: At low pressure, pure gas and an adsorbed solution are considered to be ideal; however, they may diverge from ideality as pressure increases. Mixtures of real fluids do not form ideal solutions, even though mixtures of similar liquids exhibit behavior close to ideality[16]. Therefore, the vapor and adsorbed solution phase are not ideal gas and solution. Accounting for the nonideality in an adsorption calculation is expected to improve the accuracy of the prediction. Eq. (6) equates the fugacity of each phase in comparison to Eq. (5) that equates partial pressure:

$$py_i\hat{\phi}_i = f_i^0 (\Pi)\gamma_i x_i, \quad (6)$$

where $\hat{\phi}_i$ is the fugacity coefficient of component i in the vapor phase accounting for the nonideality of the vapor phase, γ_i is the activity coefficient of component i in the solution phase accounting for the nonideality of the adsorbed solution phase, and f_i^0 is the equilibrium fugacity for pure component i corresponding to spreading pressure Π .

Figures 7 and 8 show the total moles of gas adsorbed and the composition of the adsorbed phase calculated using the extended Langmuir isotherm and the IAS model. Recall that all predictions are based on the measured pure component isotherms, Fig. 3. The Langmuir constants used in calculation are as listed in Table 2. In Fig. 7 and Fig. 8, solid lines represent IAS predictions whereas dashed lines represent predictions using the extended Langmuir model.

At low pressure (below 100 psi) in Fig. 7, the total moles of the adsorbed phase calculated using the two isotherms are virtually the same. At low pressure, the fraction of sites for adsorption that are occupied is low and the adsorbed phase is close to an ideal solution. At high pressure, the IAS model estimates greater total moles of the adsorbed phase. Another observation is that as the fraction CO₂ in the injected gas increases in Fig.

8, the difference between the results of the two models decreases. The mole fraction of CO₂ in the adsorbed phase predicted from the extended Langmuir isotherm is completely insensitive to pressure. The IAS model predicts that the affinity of the surface for CO₂ decreases with pressure.

Another variable that illustrates differences among the extended Langmuir and IAS models is the selectivity coefficient or separation factor, $s_{i,j}$

$$s_{i,j} = \frac{x_i/y_i}{x_j/y_j}, \quad (7)$$

For the Langmuir approach, the selectivity coefficient reduces to Eq. (8). The selectivity is a constant related to the Langmuir constants for given gas species, regardless of the injection gas composition and pressure.

$$s_{i,j} = \frac{v_{mi}B_i}{v_{mj}B_j}, \quad (8)$$

For the ideal adsorbed solution theory, the selectivity coefficient of CO₂ over N₂ reduces to the ratio of the equilibrium pressure of N₂ over the equilibrium pressure of CO₂,

$$s_{i,j} = \frac{p_j^0}{p_i^0}, \quad (9)$$

Figure 9 shows the Langmuir model gives a single constant separation factor, while the IAS model predicts a decrease in CO₂ selectivity as pressure increases or percentage of CO₂ in the injection gas increases. A constant mole fraction of CO₂ in the adsorbed phase and a constant selectivity at varying pressure appears to be a physically incorrect prediction. On the other hand, the results obtained from the IAS model are consistent with the experimental trends of Hall et al.[17] summarized in Fig. 10. From this point of view, the ideal adsorbed solution theory is superior in comparison to the Langmuir isotherm.

Discussion

There is no straightforward method to relate the adsorption with the permeability reduction. One way to do so is to calculate the volume occupied by the adsorbed phase to predict the change of the coal porosity. Then the change of porosity and the change of permeability are correlated.

Volume of the Adsorbed Phase: After calculating the moles of adsorption using the above isotherms, the volume occupied by the adsorbed molecules was estimated by multiplying the molecular volume of each gas and the moles of adsorption of each gas:

$$V_{adsorption} = \sum_{i=1}^{N_c} n_i N_A V_{molecule,i}, \quad (10)$$

where, n_i is the moles of component i in the adsorbed phase, N_A is the Avogadro's number, and $V_{molecule,i}$ is the molecular volume of component i . Three molecular models were assumed: (a) Spherical model, in which the molecules of the gases are assumed to be spheres of diameter d_i :

$$(V_{molecule,i})_{spherical} = \frac{4}{3} \pi (d_i / 2)^3, \quad (11)$$

where, d_i is the kinetic diameter of the molecules of gas i . The kinetic diameter of the molecules of N₂, CH₄, and CO₂ are 3.64 Å, 3.8 Å, and 3.3 Å respectively; (b) Cylindrical model, in which the gas molecules are assumed to be cylinders with a cross-sectional area of ς_i and height of d_i :

$$(V_{molecule,i})_{cylindric} = \varsigma_i d_i, \quad (12)$$

where, ς_i is the molecular cross-sectional area of the molecules of gas i . The molecular cross-sectional area of N₂, CH₄, and CO₂ is 16.2 Å², 17.7 Å², and 19.5 Å² respectively[18]; (c) SRKb model, in which the volume of the gas molecules was assumed to equal to the hard-sphere term, b , in the Soave-Redlich-Kwong cubic equation of state[19].

$$(V_{molecule,i})_{SRKb} = b = \frac{0.08664 RT_c}{P_c}, \quad (13)$$

where, b is molar volume in $cm^3/mole$, R is the universal gas constant equaling 83.144 $cm^3\text{-bar/mol-K}$, T_c is the critical temperature in K , and P_c is the critical pressure in bar . The values of b , T_c and P_c are available in the literature[19]. This model is similar to that recommended by Hall et al.[17] to account for the volume of the adsorbed phase during measurement of isotherms.

Porosity Reduction versus Permeability Reduction: We correlated the adsorbed volume to the porosity change of the system as

$$\frac{\phi}{\phi_0} = \frac{\pi r^2 L \phi_0 - V_{adsorption}}{\pi r^2 L \phi_0}, \quad (14)$$

where, ϕ_0 is the initial porosity of the coal pack measured using helium at atmospheric pressure, r is the radius of coal pack, L is the length of the coal pack. Permeability reduction is defined as

$$R_k = \frac{k}{k_0}, \quad (15)$$

where, k is the measured permeability of the coal pack after gas injection, k_0 is the initial permeability of the coal pack measured using helium at atmosphere pressure.

Fig. 11 shows the relation between the inferred change of porosity and the measured change of permeability. See also Tables 1 and 2. The change of porosity was calculated using Eq. (14). The amount of adsorption for each component was calculated based on the modified IAS model, and the volume of the adsorbed molecules was calculated using the SRKb molecular model. The prediction based on the spherical and cylindrical molecular models are qualitatively similar to that of the SRKb model, and thus, are not shown here for reasons of brevity. In the modified IAS model, fugacity is used to account for the nonideality of the vapor phase while the adsorbed solution was considered ideal. In the next section, we relax the assumption of ideal solution and considers activity coefficient models.

All experimental data falls below a cubic relationship between porosity and permeability [19]

$$\frac{k}{k_0} = \left(\frac{\phi}{\phi_0}\right)^3 \quad (16)$$

indicating a dependence on the porosity ratio with a power greater than 3.

In Fig. 11, the results for all gases do not fall onto the same trend. Instead, the mixtures of 25% CO₂, 50% CO₂, and 75% CO₂ behave similarly; the points for pure N₂, pure CH₄, and 85% CO₂ follow a second trend; and the points for pure CO₂ present a third trend. Possible brief explanations for the observations follow.

First, the initial permeability of the coal pack was measured using helium. It is assumed that at low pressure the coal pack achieves its helium permeability for all gas types. The initial permeability of the coal pack to each test gas may not be the same.

Second, all of the experiments reported here required a significant period of time to complete. During the course of experiments and between a given gas composition, the

coal pack was occasionally opened to view the integrity of the coal pack as well as to ascertain the state of the rubber sleeve. If the coal pack had settled, additional ground coal was added to the injection end. While every effort was taken to minimize disturbance to the pack, inevitably some change occurred.

Third, Table 3, indicates that CO₂ is not supercritical at experimental conditions of 22 °C whereas N₂ and CH₄ are supercritical. Correspondingly, adsorbed CO₂ exhibits properties more similar to a condensed liquid phase than to a dense gas phase. At the large surface loadings characteristic of an adsorbed liquid phase, CO₂ may not be distributed uniformly across all surfaces. Preferential blocking of the most permeable pathways by adsorbed CO₂ may yield significant permeability reduction.

Even though explanations are offered, the true reasons for the observations in Fig. 11 need further investigation. We plan to conduct additional experiments on whole cores to develop data for validation of mixed gas adsorption models. There are gaps to fill in the theoretical part of the study as well. For example, the mechanisms underlying the so-called “swelling” of coal matrix are not well understood. The layout of the adsorbed molecules and the volume occupied by the adsorbed phase are not clear. Further, the relationship between porosity and permeability when significant swelling occurs is anything but straightforward.

Summary

N₂ and CO₂ injection are commonly considered for enhancing coal bed methane recovery. Mechanisms for evolution of permeability are a change of effective stress on the coal and sorption of gas species onto coal surfaces that reduces the pore volume available to support flow. Experiments were performed to investigate the adsorption related permeability change of a coal pack with the injection of pure and binary gas mixtures at room temperature. The following specific observations are made.

1. For pure gases, at the same pore pressure, permeability reduction is greatest for CO₂ followed by CH₄, and N₂. That is, permeability reduction correlates with the total pure gas adsorption at any pore pressure.
2. When injecting N₂ and CO₂ binary mixtures, at the same pore pressure, permeability decreases with an increase of CO₂ in the injected gas.
3. When injecting N₂ and CO₂ mixtures, permeability is maintained by employing N₂ within the mixture. About 10 ~ 20% by mole fraction N₂ is sufficient to maintain permeability at the experimental conditions.
4. The ground coal samples display greater permeability reduction in comparison to consolidated coal cores. The latter exhibit less than an order of magnitude reduction in permeability to CO₂ as pressure is increased from atmospheric to roughly 800 psi.

This observation may be related to the amount of surface area in the sample available for gas adsorption.

5. Among many isotherms in the literature for predicting gas adsorption, the Langmuir isotherm gives good prediction of pure gas adsorption. While the question remains open about the best technique for predicting multi-component adsorption, the ideal adsorbed solution model, and the real adsorbed solution extension predict that gas composition and pressure affect the selectivity of a gas species for the surface. In this sense, the predictions appear to be more realistic as compared to the extended Langmuir approach.
6. The variation of porosity and of permeability for the tests conducted does not have a unique correlation. More experimental investigation is needed to fill the theoretical gaps to fully understand this observation.

References

1. Harpalani, S. and R.A. Schraufnagel: "Shrinkage of coal matrix with release of gas and its impact on permeability of coal", *Fuel*, 69:551–556, May 1990.
2. Gamson, P., B. Beamish, and D. Johnson: "Coal microstructure and secondary mineralization: Their effect on methane recovery", *Coalbed Methane and Coal Geology*, (109):165 – 179, 1996.
3. Stevens, S.H., D. Spector, and P. Riemer: "Enhanced coalbed methane recovery using CO₂ injection: Worldwide resource and CO₂ sequestration potential," paper SPE 48881, presented at the 1998 SPE International Conference and Exhibition in China held in Beijing, China (2-6 November 1998).
4. Stevens, S.H.: "Geological sequestration of CO₂ in deep, unmineable coalbeds: An integrated research and commercial-scale field demonstration project," paper SPE 71749, 2001 SPE Annual Technical Conference and Exhibition, New Orleans, Louisiana, USA (30 September – 3 October, 2001).
5. Tsotsis, T.T., H. Patel, B.F. Najafi, D. Racherla, M.A. Knackstedt, and M. Sahimi: "Overview of laboratory and modeling studies of carbon dioxide sequestration in coal beds", *Ind. Eng. Chem. Res.*, 43:2887 – 2901, 2004.
6. White, C.M., B.R. Strazisar, E.J. Granite, J.S. Hoffman, and H.W. Pennline: "2003 critical review: Separation and capture of CO₂ from large stationary sources and sequestration in geological formations—coalbeds and deep saline aquifers", *J. Air Waste Manage. Assoc.*, 53:645, 2003.
7. Harpalani, S. and X. Zhao: "The unusual response of coal permeability to varying gas pressure and effective stress," *Rock Mechanics as a Guide for Effective Utilization of Natural Resources*, Khair (ed.), page 65–72, 1989.
8. McKee, C.R., A.C. Bumb, and R.A. Koenig.: "Stress-dependent permeability and porosity of coal", *Proceedings 1987 Coalbed Methane Symposium*, page 16 – 19, 1989.
9. Jessen, K., G.Q. Tang, and A.R. Kovscek: "Laboratory and simulation investigation of enhanced coalbed methane recovery by gas injection, *Transport in Porous Media*, to appear, 2008 [DOI:10.1007/S11242-007-9165-9](https://doi.org/10.1007/S11242-007-9165-9).
10. Colmenares, L. B.: *Rock Strength Under True Axial Loading, Seismotectonics of Northern South America, and Geomechanics and Coal Bed Methane Production in the Powder River Basin*, Ph.D. Thesis, Stanford University, Stanford, CA (2004).
11. Moore, W. R.: "Geothermal Gradient of the Powder River Basin, Wyoming," presented at the AAPG Annual Meeting, Salt Lake City, UT U.S.A. 11-14 May 2003.
12. Yang, R.T.: "Gas separation by adsorption processes", Butterworths Publishers, Johannesburg, South Africa, pages 26–51, 1987.
13. Myers, A.L. and J.M. Prausnitz: "Thermodynamics of mixed-gas adsorption", *AIChE*, 11:121–127, 1965.
14. Gamba, G., R. Rota, G. Storti, S. Carra, and M. Morbidelli: "Adsorption solution theory models for multicomponent adsorption equilibria," *AIChE*, 35(6):959 – 966, 1989.

15. Arri, L.E., W.D. Yee, and M.W. Jeansonne: "Modeling coalbed methane production with binary gas sorption", paper SPE 24363 presented at the SPE Rocky Mountain held in Casper, WY U.S.A., 18-21 May 1992.
16. Prausnitz, J. M.: Molecular Thermodynamics of Fluid-Phase Equilibria", pages 213 – 326, 1999.
17. Hall, F.E., C.-H. Zhou, K.A.M. Gasem, R.L. Robinson Jr., and D. Yee: "Adsorption of pure methane, nitrogen, and carbon dioxide and their binary mixtures on wet Fruitland coal", paper SPE 29194 presented at the Eastern Regional Conference and Exhibition, Charleston, WV U.S.A., 8-10 November 1994.
18. Adamson, A.W., and Gast, A.P.: Physical Chemistry of Surfaces 6th Ed., John Wiley & Sons, New York, 1997.
19. Reid, R.C., J. M. Prausnitz, and B.E. Poling. The Properties of Gases and Liquids 4th Ed., McGraw-Hill, Inc., New York, 1987.

Table 1 – Parameters for permeability and pressure correlation.

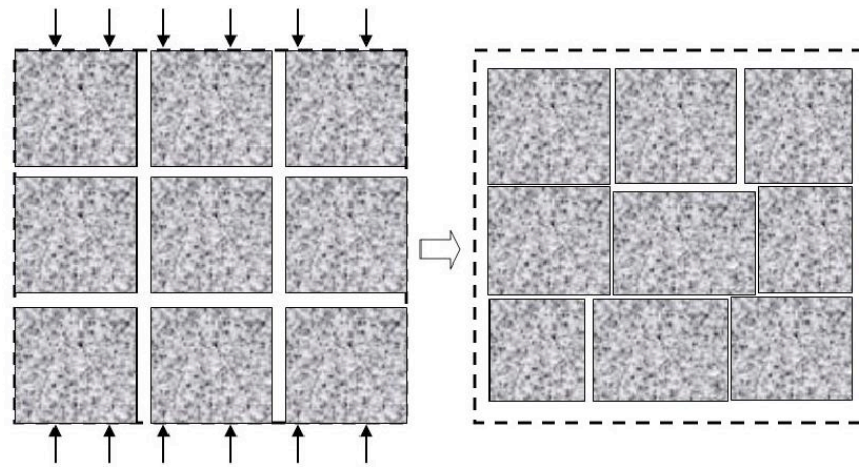
| Injection Gas Composition | b | Minimum k/k ₀ | Average Relative Error % |
|--|---------|--------------------------|--------------------------|
| 100% N ₂ | -0.0982 | 0.5159 | 5.21 |
| 100% CH ₄ | -0.1624 | 0.3304 | 6.29 |
| 100% CO ₂ | -0.7468 | 0.0047 | 47.1 |
| 25% CO ₂ + 75% N ₂ | -0.1367 | 0.4001 | 3.16 |
| 50% CO ₂ + 50% N ₂ | -0.1564 | 0.3546 | 2.31 |
| 75% CO ₂ + 25% N ₂ | -0.1666 | 0.3321 | 1.38 |
| 85% CO ₂ + 15% N ₂ | -0.2817 | 0.1475 | 9.09 |

Table 2 – Langmuir constants used in adsorption prediction (for the Powder River Basin coal samples used in this study).

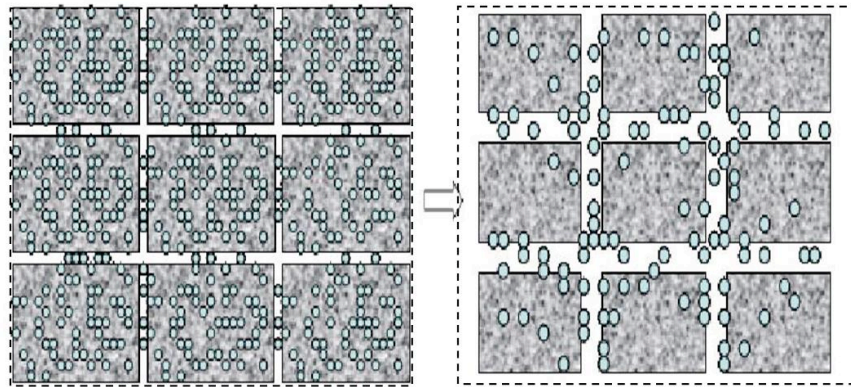
| Gas Species | v _m , SCF/t | B, psi ⁻¹ |
|-----------------|------------------------|----------------------|
| N ₂ | 263.16 | 0.0025 |
| CH ₄ | 666.70 | 0.0035 |
| CO ₂ | 1666.70 | 0.0071 |

Table 3 – Critical temperature and critical pressure for pure N₂, CH₄, and CO₂[19]

| Gas Species | T _C , °C | p _C , psi |
|-----------------|---------------------|----------------------|
| N ₂ | -146.95 | 491.67 |
| CH ₄ | -82.75 | 667.17 |
| CO ₂ | 30.95 | 1070.38 |



(a)



(b)

Figure 1 — Dual structure of coal and mechanisms of coal permeability change: (a): permeability evolution of coal due to change of effective stress and (b) permeability evolution of coal due to sorption of gases

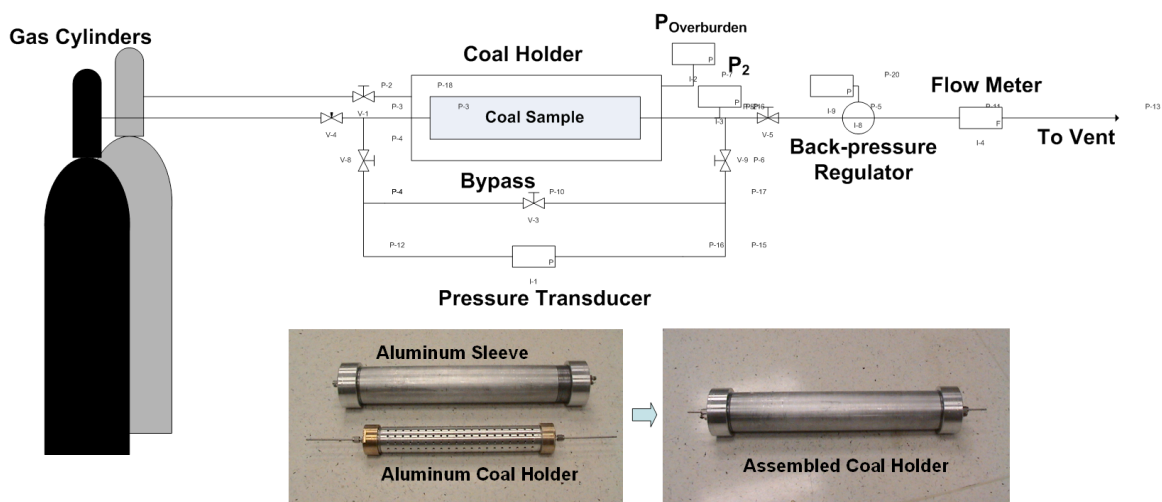


Figure 2 — Schematic of experimental setup for measuring the permeability of a coal pack, at constant effective stress, varying pore pressure; and photographs of the disassembled and assembled coal holder

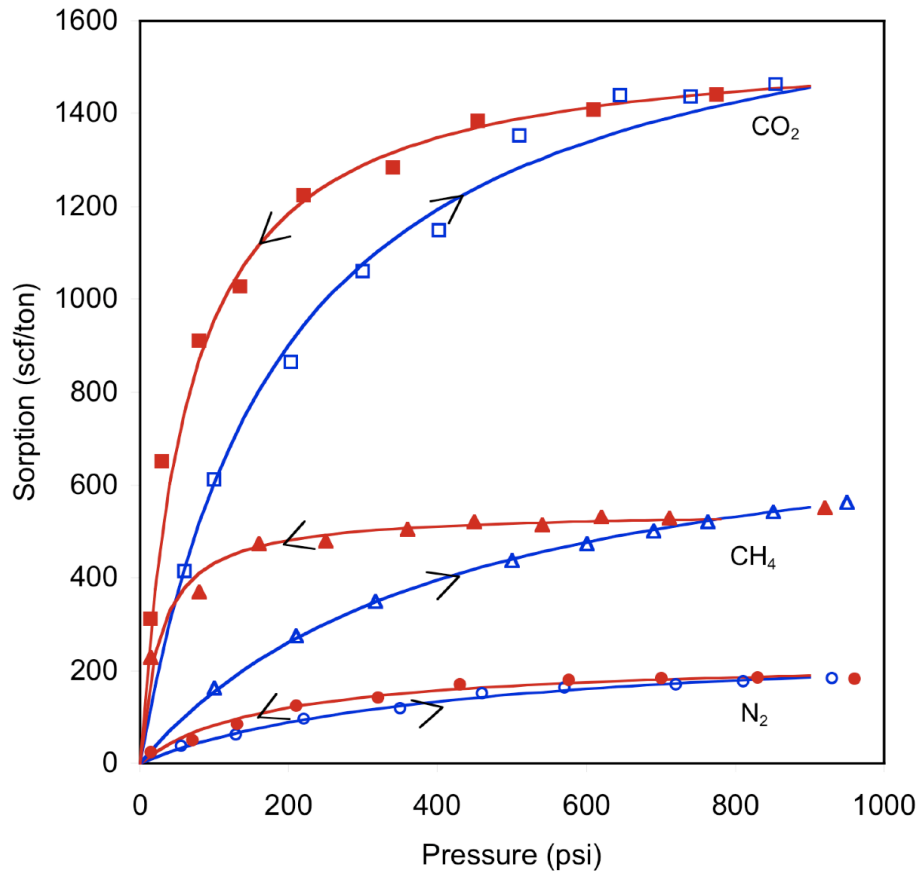


Figure 3 — Sorption characteristics of Power River Basin (Wyoming) coal: Adsorption indicated with open symbols and desorption with closed symbols, measurements conducted at 22 °C

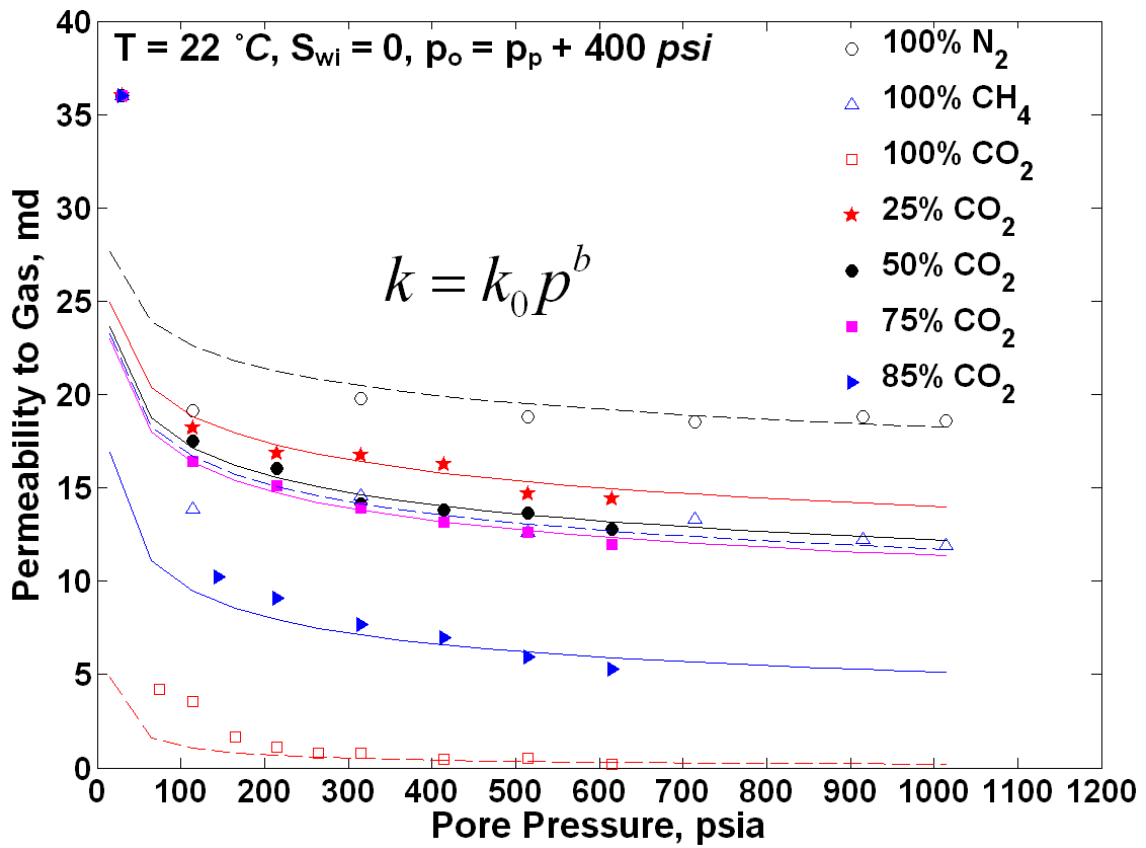


Figure 4 – Absolute permeability of the dry coal pack after injection of gases at varying pressure, effective stress is 400 psi in all cases.

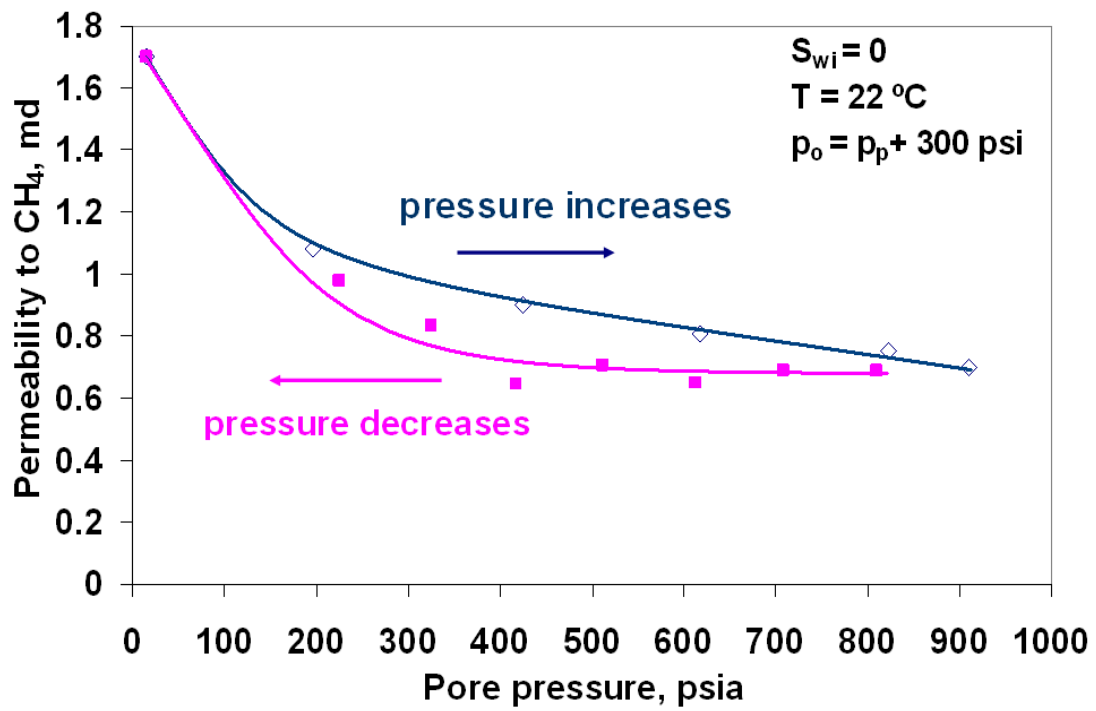


Figure 5.—Permeability of dry composite coal core to methane. Arrows indicate increasing/decreasing pressure. Effective stress equals 300 *psi*

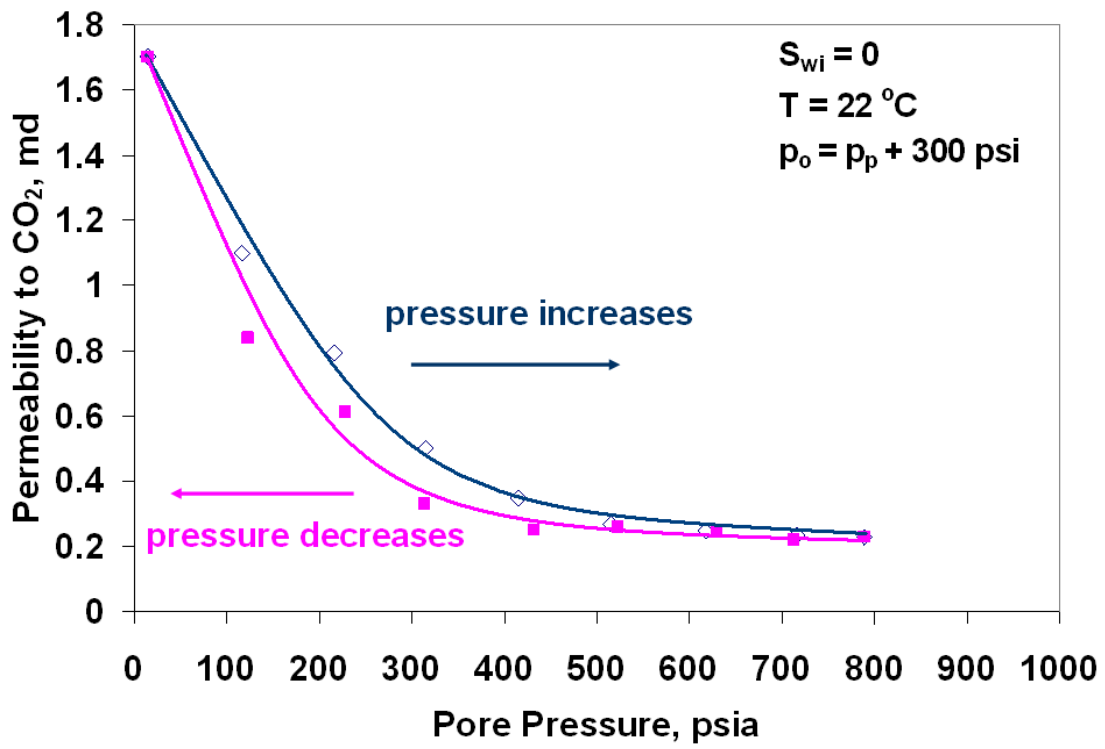


Figure 6—Permeability of dry composite coal core to carbon dioxide. Arrows indicate increasing/decreasing pressure. Effective stress equals 300 *psi*

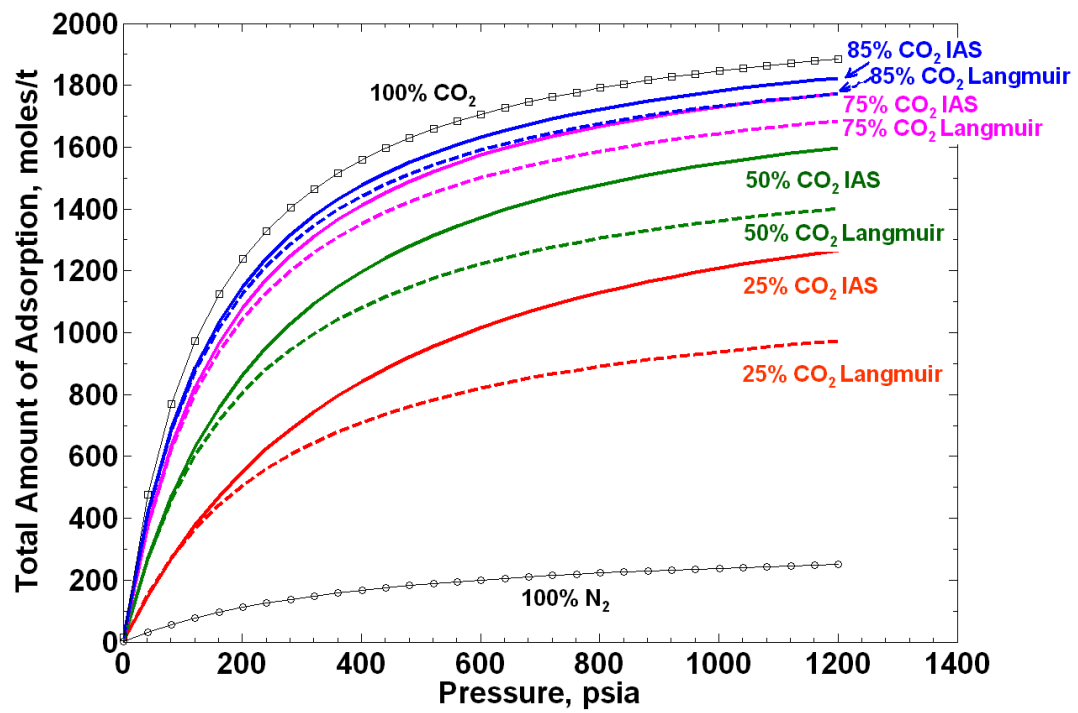


Figure 7—Total adsorption predicted by the extended Langmuir isotherm (dashed lines) and the IAS model (solid lines), bounded by the measured (symbols) pure adsorption of N₂ and CO₂.

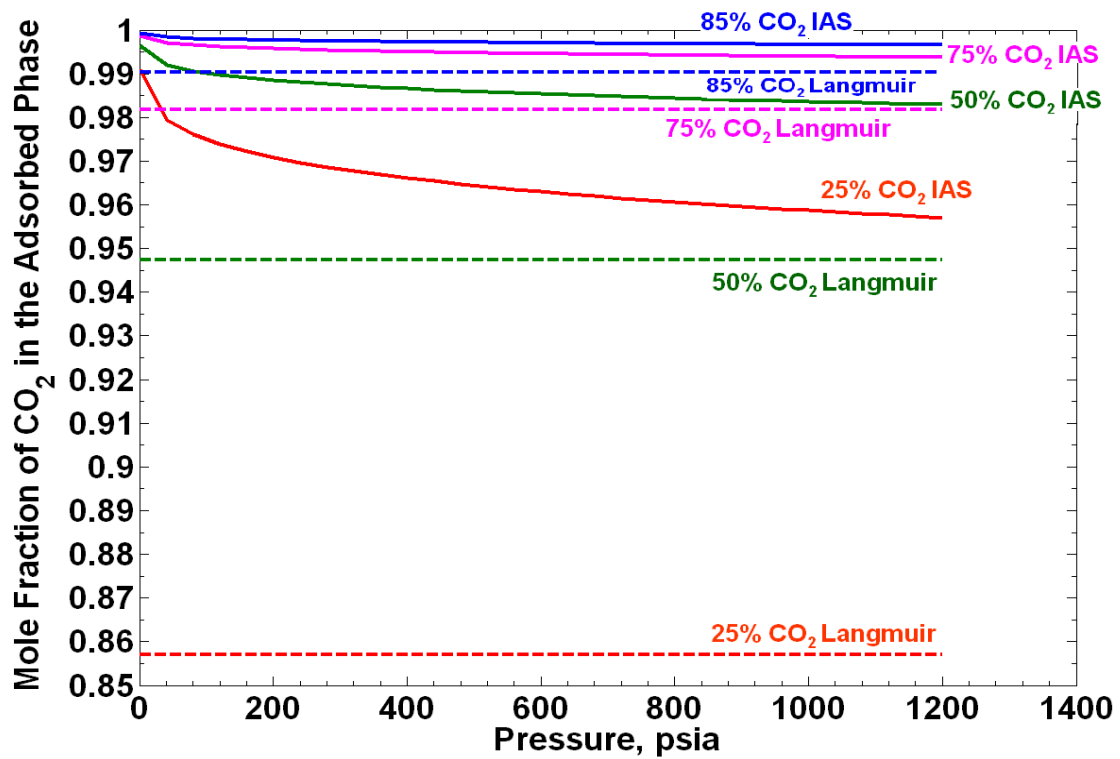


Figure 8—Mole Fraction of CO₂ in the adsorbed phase calculated using the extended Langmuir (dashed lines) isotherm and IAS model (solid lines)

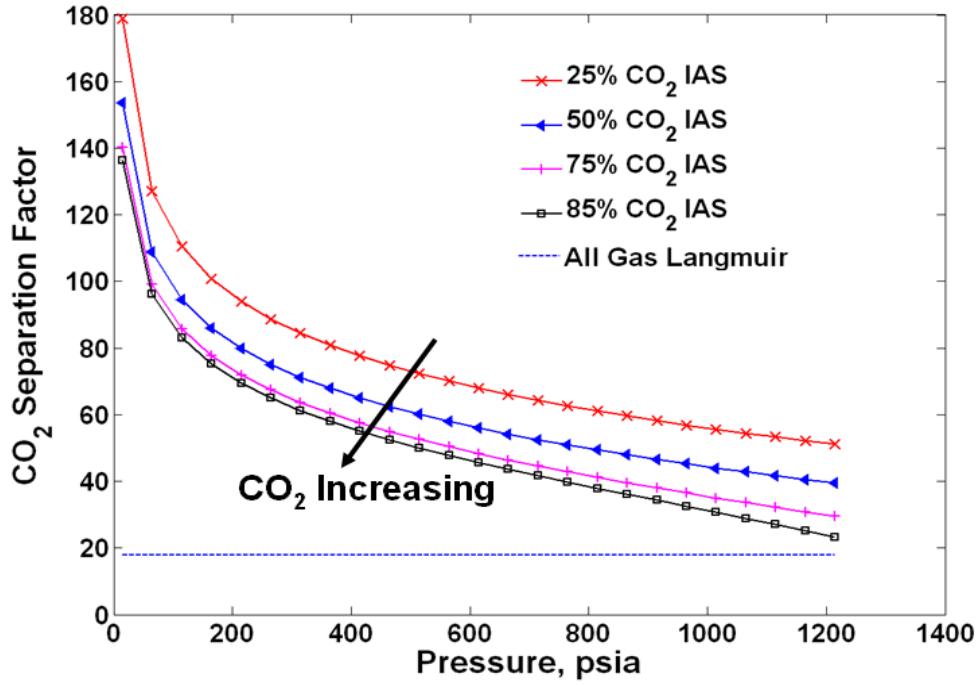


Figure 9 — Separation factor of CO₂ over N₂. Predictions are based on the extended Langmuir (dashed line) isotherm and the IAS (solid lines) model. The arrow indicates increasing CO₂ in the gas mixture.

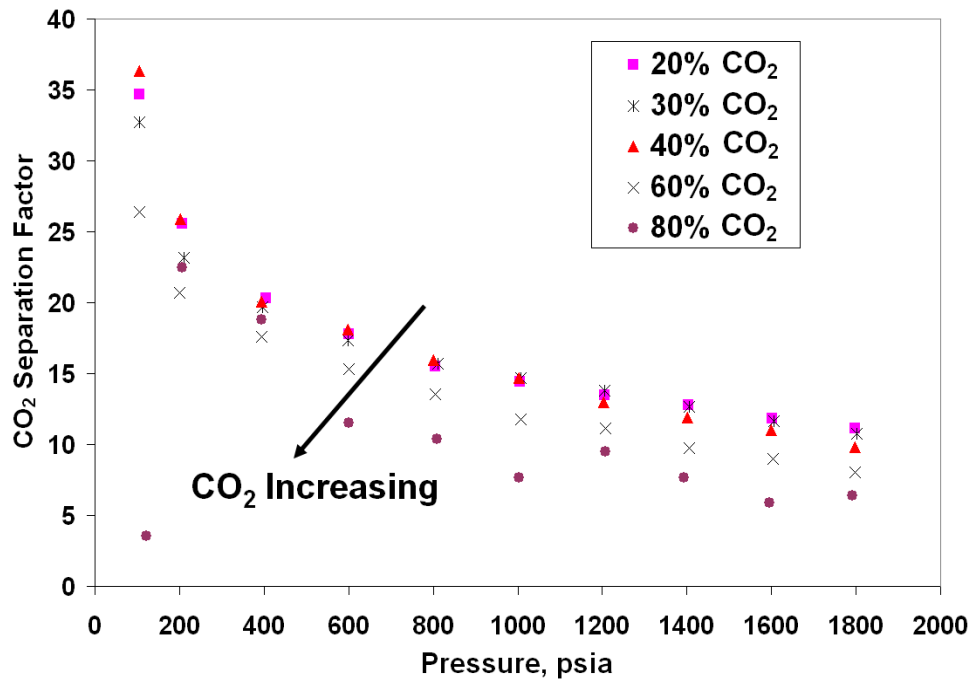


Figure 10 — Separation factor of CO₂ over N₂. Adsorption of CO₂/N₂ binary mixtures on wet Fruitland coal at 115°F, experimental data of Hall et. al.[17] The arrow indicates increasing CO₂ in the gas mixture.

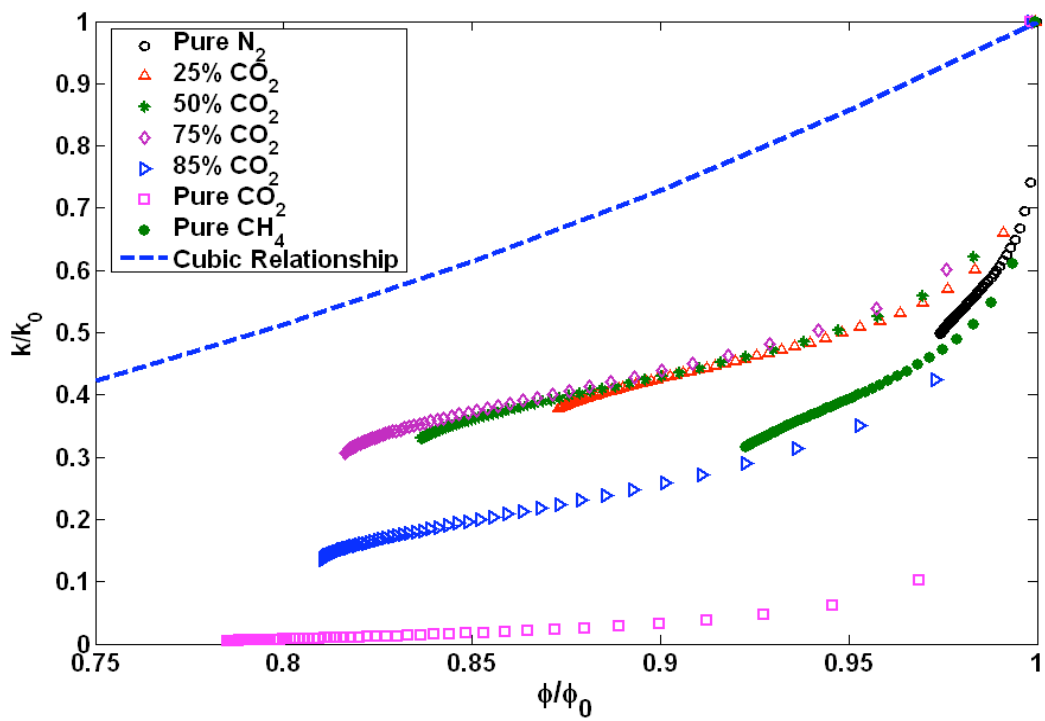


Figure 11 — Correlation between the inferred change of porosity and the measured change of permeability.

Multicomponent Sorption Modeling During Convective Transport in Coalbeds

The dynamics of CO₂ movement and any accompanying enhanced coalbed methane (ECBM) recovery are determined in large part by the sorption behavior of mixtures of CH₄, CO₂ and N₂ on the coal surface. Conventional flow simulation tools use the extended Langmuir model for predicting the sorption behavior of the gas mixtures that form during a displacement process. In previous work, we demonstrated the applicability of this approach for binary CH₄/CO₂ and CH₄/N₂ displacements by comparison to lab-scale experiments. The extended Langmuir model was, however, unable to describe the behavior of ternary CH₄/CO₂/N₂ displacements. Adsorption hysteresis is a complicating factor also. We have investigated the accuracy of ternary gas displacement calculations. We find that a sorption model more sophisticated than the extended Langmuir model is needed to represent the dynamics of multicomponent systems. We use the Ideal Adsorbate Solution model (IAS) and compare the predicted behavior to standard calculations and experimental results.

Initially, we describe the implementation of the IAS model into our dual-porosity flow simulator. The IAS model requires an iterative scheme as opposed to the explicit calculation from the extended Langmuir model. Accordingly, the IAS model is more computationally expensive than traditional approaches. The predicted displacement behavior substantially agrees with the experimental observations in comparison to the inaccurate predictions from the traditional approach for a series of ternary CH₄/CO₂/N₂ displacements.

Accurate tools for prediction of displacement performance processes are instrumental in design and implementation of carbon dioxide sequestration schemes. The results and analysis presented in this paper, demonstrate that more sophisticated thermodynamic models must be used in flow simulators of gas mixture in coal when mixtures of CO₂ and N₂ are used to displace CH₄ from coalbeds.

Introduction

The increasing concentration of CO₂ in the earth's atmosphere has motivated a wide range of initiatives aimed at reducing greenhouse gas emissions and developing less carbon intensive energy sources. Storage of CO₂ in coal seams is a potentially attractive carbon sequestration technology for at least two reasons. First, injection of CO₂ or mixtures of CO₂ and N₂, enhances methane production from coalbeds. Only about one-half of the gas originally in place in a coalbed is estimated to be recovered following primary operations. This leaves a large target in place for enhanced recovery operations. Second, coals of various ranks all generally adsorb a greater amount of CO₂ in comparison to CH₄ and thus geological sequestration of CO₂ in coalbeds has the potential to be carbon neutral or perhaps a carbon sink. In short, CO₂ is sequestered, while CH₄ recovery from coal is enhanced, thus costs are either partially or completely offset while increasing production of CH₄.

Gas flow in coal, however, is a result of a delicate interplay among pressure gradients, coal permeability, and adsorption phenomena. Although some gas within coal exists as bulk phase within pores and cleats (fractures), most gas is on the surface of coal in an adsorbed state at liquid-like density. Because of adsorption, a coalbed may contain more methane than a conventional gas reservoir of comparable size, pressure, and temperature. Effective methods, however, to release fully methane from a coalbed have yet to be developed.

Nitrogen is one choice for ECBM due to its availability. Nitrogen serves to reduce the partial pressure of methane in the free gas within pores and this causes CH₄ to desorb from coal surfaces. CO₂ also has advantages as an injection gas. CO₂ is a more effective displacement agent as it adsorbs more strongly to coal surfaces than either CH₄ or N₂. The adsorption properties of CO₂ may also help to limit premature breakthrough at production wells.

In practice, injection gases for ECBM may be mixtures of CO₂ and N₂. N₂ generally leads to a more rapid production response than does CO₂, but CO₂ leads to more complete displacement. Another advantage of gas mixtures is that changes in coalbed permeability are mitigated by inclusion of some N₂ with injected CO₂. Our experiments reported elsewhere [1], show that a small fraction of N₂, 10 to 20% by mole, helps to preserve coalbed permeability significantly.

The possible importance of gas mixtures for ECBM as well as our inability to describe previous ternary gas displacement experiments [2] in coal packs with the extended Langmuir equation motivates us to study the representation of multicomponent gas adsorption in the context of gas flow through dual porosity porous media. To the best of our knowledge, this is the first attempt describing the impact of using a sophisticated, multicomponent sorption model for predicting the displacement behavior of ECBM processes.

The remainder of this section is organized in the following fashion. Next, we lay out in some detail the vapor-adsorbate IAS model. Subsequently, we describe the incorporation of adsorption/desorption hysteresis into adsorption models and then turn to displacement calculations. A variety of example calculations illustrate improved predictive capabilities. Discussion and summary sections round out the section.

Sorption modeling

Various models have been proposed and investigated for modeling multicomponent sorption on coal [3]. Initially we consider the extended Langmuir approach [4] that predicts the adsorption of multicomponent gas mixtures solely from pure component data. Due to its simplicity, it is the most commonly applied sorption model in simulation of ECBM recovery processes [5]. According to the extended Langmuir model, the specific amount n_i (scf/ton or mol/kg) of a given species adsorbed onto the coal surface in equilibrium with a bulk gas phase of composition \mathbf{y} is calculated from

$$n_i = \frac{V_{m,i} b_i y_i p}{1 + \sum_k b_k y_k p}, \quad (1)$$

where $V_{m,i}$ and b_i are Langmuir parameters for the adsorption of the pure species, p is the pressure and y_i is the mole fraction of component i in the bulk gas phase. The extended Langmuir approach is straight forward to implement in single or dual porosity ECBM simulators and provides for a pressure-explicit calculation of the adsorbed amounts with no iterative scheme required.

Various investigators [e.g. 3] have demonstrated that the extended Langmuir approach is fairly accurate in modeling sorption behavior of binary gas mixtures on coal, but that the model fails to reproduce experimental observations for ternary gas mixtures (e.g. CH₄/CO₂/N₂) of relevance to ECBM processes.

The inaccuracy of the extended Langmuir approach is especially evident in the work of Tang *et al.* [2] who applied this adsorption model in flow simulations to interpret experimental observations from displacements of CH₄ by mixtures of CO₂ and N₂ in packs of dry, ground coal from the Powder River basin.

Next we consider the approach of Myers and Prausnitz [6] who applied the assumption of an ideal adsorbate solution (IAS) to formulate a thermodynamically consistent model for multicomponent sorption. The IAS model is derived from the general theory of vapor-adsorption equilibrium where the fugacity of a component in the vapor phase must be equal to the fugacity of a component in the adsorbate phase. This is an analogy to vapor-liquid equilibrium calculations that are standard for miscible injection processes. At isothermal conditions, equality of fugacity is written for each component i in a mixture as [6]:

$$y_i p \varphi_i \{ \mathbf{y}, p \} = x_i f_i^o \{ \Pi \} \gamma_i \{ \mathbf{x}, \Pi \}, \quad (2)$$

where φ_i is the fugacity coefficient of component i in the gas phase evaluated at the pressure p and overall gas phase composition \mathbf{y} . On the right hand side of Eq. 2, f_i^o is the pure component fugacity of component i evaluated at the spreading pressure (Π) of the adsorbate mixture and γ_i is the activity coefficient of component i evaluated at the composition (\mathbf{x}) and spreading pressure of the adsorbate mixture.

The spreading pressure of the adsorbed phase can not be measured directly but is evaluated by integration of the Gibbs adsorption isotherm [7]. For pure component sorption, this integration leads to

$$\Pi_i^* = \frac{\Pi A}{RT} = \int_0^{\Pi} n_i \times d \ln f_i, \quad (3)$$

where A is the surface area, R is the gas constant, T is the temperature, n_i is the specific amount adsorbed and f_i is the fugacity of the pure gas phase. We have kept the subscript i in Eq.(3) for clarity. The integral of Eq. 3 is evaluated from experimental observations of n versus p combined with an equation of state based calculation of the fugacity.

The IAS model [6] is derived by assuming that the gas phase behaves like an ideal gas and that the adsorbate phase behaves like an ideal mixture. With on these assumptions Eqs. (2) and – (3) are rewritten as

$$y_i p = x_i p_i^o \quad (4)$$

and

$$\Pi_i^* = \int_0^{p_i^o} n_i \times d \ln p, \quad (5)$$

where p_i^o is the pressure corresponding to a pure adsorbate phase at the spreading pressure of the true adsorbate phase. In this work we simplify Eq. (5) further by assuming that the pure component adsorption behavior is represented sufficiently accurately by the Langmuir isotherm. This assumption allow us to rewrite the integral for each component as

$$\Pi_i^* = V_{m,i} \times n(1 + b_i \times p_i^o). \quad (6)$$

The amount of component i adsorbed on the coal surface at the reference state p_i^o is denoted n_i^o and is calculated directly from the pure component isotherm. The total specific amount of gas adsorbed on the coal surface (n_t) in equilibrium with a gas mixture is given by

$$n_t = \left(\sum_i \frac{x_i}{n_i^o} \right)^{-1}, \quad (7)$$

whereas the specific amounts of components in the adsorbate phase are given by

$$n_i = x_i \times n_t \quad (8)$$

Finally, at equilibrium, the spreading pressure evaluated for each component at the corresponding reference pressure (p_i^o) must be equal

$$\Pi_i^* = \Pi_j^* \quad (9)$$

Given the pressure (p) and composition (y) of the gas phase, Eqs. 4 and 9 are solved iteratively for the unknown adsorbate composition by the following steps:

1. Guess n_c-1 adsorbate mole fractions ($\sum(x_i) = 1$)
2. Evaluate the pure component reference pressures (p_i^o) for all components from Eq. 4.
3. Evaluate the spreading pressure for each component from Eq. 5 (or 6) from pure component sorption data.
4. Evaluate the departure from equilibrium using Eq. 9
5. Update n_c-1 adsorbate mole fractions and repeat from step 2 until equilibrium is reached.

We use a Newton-Raphson approach for updating the unknown adsorbate mole fractions. Once the equilibrium mole fractions are known, n_i^o is evaluated directly from pure component sorption data (or Langmuir isotherm) and the total amount of gas adsorbed onto the coal surface is subsequently evaluated from Eq. (7). Finally, the adsorbed amount of component i is evaluated from Eq. (8).

The adsorption equilibrium compositions predicted by the IAS model and the extended Langmuir model are compared for the CH₄-CO₂ binary system in Figs 1 and 2. In this comparison, we have used the pure component Langmuir constants reported for adsorption by Tang *et al.* [2] (see Table 1). These constants were shown to reproduce accurately the experimental observations of pure component sorption on ground coal samples at 22°C from atmospheric pressure up to around 1000 psia.

Figure 1 reports the equilibrium composition of the adsorbate phase as a function of the gas phase composition at 600 psia and 22°C for the CH₄-CO₂ binary. The IAS model predicts that the CO₂ adsorbs more strongly to the coal surface than does the extended Langmuir approach. Accordingly, we expect a difference in the predicted displacement behavior when CO₂ is injected to displace CH₄ in a coal pack.

A major difference between the extended Langmuir model and the IAS model is that the first model predicts a constant selectivity $S_{i,j}$ with

$$S_{i,j} = \frac{x_i / y_i}{x_j / y_j} = \frac{V_{mi} \times b_i}{V_{mj} \times b_j} \quad (10)$$

whereas the IAS model predicts that the selectivity is a function of the gas phase composition as shown in Fig. 2.

The difference in the predicted selectivity for the CH₄-CO₂ system indicates that displacement calculations with CO₂ displacing CH₄ based on the IAS model are more strongly self sharpening. This behavior and the consequences for numerical calculations for ECBM processes are discussed in more detail in the subsequent section on displacement calculations.

Sorption hysteresis

Several investigators of the sorption behavior of gases on coal have reported observations of hysteretic behavior in the adsorption-desorption isotherms [2,8,9]. Seri-Levy and Avnir [10] demonstrated by numerical calculations that heterogeneity in the surface geometry is sufficient to introduce adsorption-desorption hysteresis loops.

Here we propose a self-consistent approach for predicting scanning loops based on bounding adsorption and desorption curves and compare predictions with the observations of Tang *et al.* [2]. We use the pure component Langmuir isotherm as a starting point for estimating scanning loops and assume that the loading and unloading curves of pure components are adequately represented by this isotherm. Let n_a and n_d denote the specific amount of a component that is adsorbed on the coal surface during a bounding loading and unloading curve respectively. If the partial pressure of the component reaches a maximum (p_{max}) and is then decreased before the bounding curves (n_a and n_d) meet, the amount of adsorbate on the coal surface follows the path of a scanning curve (n_s) as the pressure is decreased. To predict the behavior of the sorption along a scanning curve we need to determine the parameters of the Langmuir isotherm (V_m , b) for that particular path. To find the V_m and b for a given scanning curve, we use the following relations

$$n_s(p_{max}) = n_a(p_{max}) \quad (11)$$

or

$$\frac{V_{ms} \times b_s \times p_{max}}{1 + b_s \times p_{max}} = \frac{V_{ma} \times b_a \times p_{max}}{1 + b_a \times p_{max}}, \quad (12)$$

$$\left. \frac{\partial n_s}{\partial p} \right|_{p_{max}} = \alpha \left. \frac{\partial n_d}{\partial p} \right|_{p_{max}} + (1 - \alpha) \left. \frac{\partial n_a}{\partial p} \right|_{p_{max}} \quad (13)$$

where

$$\frac{\partial n}{\partial p} = \frac{V_m \times b}{(1 + b \times p)^2} \quad (14)$$

α is a parameter of interpolation between the slopes of the bounding curves that sets the slope of the scanning curve at p_{max} . The interpolation parameter α is expressed as

$$\alpha = \frac{n_d(p_{max})}{n_a(p_{max})} \quad (15)$$

Given a set of bounding curves, scanning curves (Langmuir constants) are generated from solving Eqs. 12 and 13 for the unknowns (V_{ms} and b_s) given value of p_{max} . Two scanning curves with $p_{max} = 420$ psia and $p_{max} = 600$ psia are compared with the experimental observations of Tang *et al.* for adsorption and desorption of CH₄ and a ground coal sample at 22°C in Fig. 3. The proposed approach for generating scanning curves from bounding adsorption and desorption curves is in good agreement with the observed behavior. We note that the 420 psia scanning curve is reproduced if the 600 psia scanning curve is used as a bounding desorption curve.

Displacement calculations

In this section, we compare the displacement behavior predicted from simulations using the extended Langmuir model and the IAS models with the experimental observations of Tang *et al.* [2] for a set of ternary displacements. We have modified our dual porosity 1D simulator described in Tang *et al.* [2] to include longitudinal dispersion and the option of using the IAS model for predicting sorption behavior. In addition, we have implemented the hysteresis model described in the previous section.

In dimensionless form, the conservation equation for each component is

$$\frac{\partial}{\partial \tau} \left(C_i + \frac{1-\phi}{\phi} A_i \right) + \frac{\partial}{\partial \xi} \left(v_D C_i - \frac{1}{Pe} \frac{\partial C_i}{\partial \xi} \right) = 0 \quad (16)$$

where C_i is the molar density of component i , A_i is the molar density of component i in the adsorbed phase. The dimensionless variables of Eq. (16) are defined by

$$\tau = \frac{v_{inj} \times t}{\phi \times L}, \xi = \frac{x}{L}, v_D = \frac{v}{v_{inj}}, Pe = \frac{L v_{inj}}{K_l} \quad (17)$$

where v_{inj} is the injection velocity, ϕ is the porosity and L is the length of the system. The Peclet number (Pe) is based on a longitudinal dispersion coefficient (K_l) that includes contributions from molecular diffusion and mechanical dispersion according to the

formulation of Perkins and Johnston [11] for unconsolidated sand and bead packs given by

$$K_l = D + 1.75vd_p, \quad (18)$$

where D is the apparent diffusion coefficient in the porous medium, v is the average interstitial velocity and d_p is the particle diameter. The longitudinal dispersion coefficient was estimated based on the experimental settings of Tang *et al.* [2] reported in Table 2. From these parameters, the Peclet number is approximately 500. It is important to note that the Peclet number can not be estimated directly from effluent data as for miscible displacements without sorption. Additional experimental observations are needed to characterize the dispersion in a coal pack from displacements with non-adsorbing gases unless an exact representation of the sorption behavior of the gases (mixtures) used in a displacement experiment is known.

Binary displacement calculations

To investigate the performance of the IAS model and its ability to reproduce experimental observations relative to the extended Langmuir model, we start by considering the binary displacement experiments reported by Tang *et al.* [2]

In the first comparison, CH₄ is displaced by injection of pure CO₂ at 600 psia and 22°C. Figure 4 reports the predicted effluent concentration as a function of the pore volumes of gas injected (PVI). Two simulations with each sorption model are compared with the experimental observations in Fig.4. In the first set of simulations, the Langmuir parameters from the pure component adsorption isotherms were used assuming that information about the de-sorption isotherm of CH₄ was not available, and in the second set of example calculations, the hysteresis model presented above was used based on the bounding adsorption and desorption curves reported in Table1. From Fig. 4, it is evident that the de-sorption isotherm of CH₄ must be known or estimated from bounding curves to accurately reproduce the experimental observations. A second finding from the initial calculation investigation was a significant difference in the grid resolution needed when the IAS model was used relative the extended Langmuir model. This difference is shown in Fig. 5 and Fig. 6 that reports the results of a grid refinement study for fixed Peclet numbers. The lower selectivity of the coal towards CO₂ predicted by the Langmuir approach results in less self-sharpening displacement behavior. This, in turn, renders the displacement calculation more sensitive to numerical diffusion and increases the number of grid cells need to approach a converged solution. For the Langmuir approach, we use 640 grid cells to reach convergence whereas the IAS model requires 160 grid cells only. The stronger selectivity towards CO₂ predicted by the IAS model required that the estimated Peclet number of 500 was reduced by a factor of 5 to reproduce the experimental observations. Similarly, the Peclet number for the simulation with the extended Langmuir model was increased by a factor of 2.5. In the remainder of the

calculation examples, we use 640 cells when the Langmuir model is used and 160 grid cells when the IAS model is used in the simulations. We use different Peclet numbers discussed above for simulations with the different models.

In a second comparison, we repeated the exercise above when pure N_2 is used to displace CH_4 . Figure 7 reports the predicted effluent concentrations based on the Langmuir approach with and without hysteresis. For the IAS model, behavior similar to that of the Langmuir approach was observed and has been omitted. Figure 7 illustrates, again, the need for knowledge about CH_4 desorption behavior either from experimental observations or by estimation from bounding curves.

Figure 8 compares the effluent concentrations predicted by the IAS model and the Langmuir model for the second displacement example and shows that both models are capable of reproducing the experimental observation for this binary system with sufficient accuracy.

Ternary displacement calculations

Next we consider the performance of the two sorption models when applied to ternary displacement calculations. Three ternary displacement experiments were presented in the work of Tang *et al.* [2]. These displacement experiments used mixtures of CO_2 and N_2 to displace CH_4 from the coal pack at 600 psia and $22^\circ C$. The injection compositions used in the experiments were 24/76, 46/54 and 85/15 mole % CO_2 and N_2 .

Figure 9 reports the predicted displacement behavior from the two sorption models with (dotted lines) and without (full lines) sorption hysteresis included in the calculations for the first ternary displacement (24/76 - CO_2/N_2 injection stream). The experimental observations of Tang *et al.* [2] are shown as symbols. From these displacement calculations, it is evident that the extended Langmuir approach is in large disagreement with the experimental observations and predicts a breakthrough time of the injected gas that is 0.25 PVI later than what is observed from the experiment. On the other hand, the arrival of the CO_2 at the outlet is predicted to occur 0.5 PVI earlier than what is observed from the experiment. The timing of the effluent concentrations predicted from simulations using the IAS model is in much better agreement and captures more completely the features of the experimental observations. Discrepancies are still noticed. The improvement in the overall predictive capability of the IAS model, however, is clearly demonstrated from this example.

The predicted behavior and the experimental observations are compared for the second ternary system (46/54 – CO_2/N_2 injection stream) in Fig. 10. Figure 10 reports the same two sets of calculations as in the previous example (with and without hysteresis). In this second calculation, the difference between the accuracy of the IAS and Langmuir approach relative to the experimental observations is more significant. The simulation based on the extended Langmuir approach underestimated the arrival of injected N_2 at the outlet by approximately 0.5 PVI while at the same time predicts that the injected CO_2

arrives at the outlet 0.25-0.5 PVI too early. The timing of the arrival of the two fronts at the outlet is more accurately captured by the IAS model. In addition, the IAS model predicts the formation of a N₂ rich bank in far better agreement with the experiment than does the Langmuir model. As for the previous calculation example, the inclusion of hysteresis in the displacement calculations improves the agreement with the experimental observation.

Predicted effluent concentrations and experimental observations for the third ternary example (85/15 – CO₂/N₂ injection stream) are compared in Fig. 11. As for the previous displacement, the timing of arrival of the N₂ bank predicted by the Langmuir approach is in significant error (~0.5 PVI) whereas the arrival of the injected CO₂ is captured more accurately. The IAS model predicts arrival times of both the N₂ bank and the breakthrough of the injected CO₂ with better accuracy. Both approaches show some departure from the experimental observations with respect to the maximum concentration of N₂ in the N₂ rich bank.

Discussion

In the previous sections, we have discussed the implementation of a more sophisticated sorption model in a dual porosity ECBM simulator. We have presented a self consistent approach for incorporating the hysteresis observed in the pure component adsorption/desorption isotherms into predictions for multicomponent gas mixtures. Hysteretic effects may be important in ternary ECBM calculation due to the formation of a N₂ bank downstream of the injected CO₂. That is, N₂ in the injection gas first adsorbs and then is caused to desorb by the advancing CO₂. The underlying assumption of the presented approach is that hysteresis in multicomponent systems is represented by experimental observations for pure component sorption data. This is clearly an approximation and the quality of this approach should be tested against adsorption/desorption experiments for binary and ternary mixtures.

A notable point evident in the displacement calculations is that the match between experiment and calculation improves as physically realistic complexity is added to the model for adsorption. That is, the details of multicomponent adsorption are evident in the elution behavior of the various gas species. The greatest improvement in the match for ternary systems is achieved as the adsorption model is switched from extended Langmuir to IAS. This improvement likely originates from the fact that IAS predicts that the selectivity of a gas species for a coal surface is a function of pressure and the composition of the gas phase.

Although the IAS model is shown to improve the predictive capabilities in the presented calculation examples relative to the extended Langmuir model, some discrepancies are still noted between simulation results and experimental observations. This is most likely a result of the assumption of ideal adsorbate behavior and ideal gas behavior used in the IAS model. At the elevated pressure of the experiments (600 psia),

the gas phase depart from ideal gas behavior, especially gas mixtures with CO₂. Additionally, the adsorbate phase may depart from the behavior of an ideal solution. Both effects can be included in the simulations by using the general form of the equilibrium relations including the gas phase fugacity coefficients and the adsorbate phase activity coefficients. This is a future direction for our research.

The calculation of gas-phase nonideality is straight forward and readily available from standard equations of states. Activity coefficient models, however, for adsorbed mixtures require additional experimental work to determine model parameters and are as a consequence less popular. Examples of activity coefficient models for mixed gas adsorption modeling are given by Talu *et al.* [7].

Summary

In the previous sections we investigated the performance of the IAS model for prediction of ternary ECBM displacement processes. Based on the examples and analysis we conclude that

1. The IAS model has been implemented in a dual porosity simulator and tested for two binary and three ternary displacements.
2. Sorption hysteresis must be included in displacement calculations to improve the predictive capabilities of both the extended Langmuir and the IAS approach.
3. The IAS model and the extended Langmuir model differ significantly in the predicted selectivity of CO₂ for binary CH₄/CO₂ displacements. Consequently, the sensitivity of displacement calculations with the two models with respect to numerical diffusion is different. The Langmuir model is more sensitive to grid-size effects and more difficult to converge.
4. For all ternary displacement calculations, the IAS model predicts more accurately the timing of composition fronts arriving at the outlet.

References

1. Lin, W, Tang, G.-Q., and Kovscek, A. R.: "Sorption-Induced Permeability Change of Coal During Gas-Injection Processes" SPE 109855, presented at the SPE Annual Technical Conference and Exhibition held in Anaheim, CA U.S.A., 11-14 Nov. 2007
2. Tang G.-Q., Jessen K., and Kovscek A. R.: "Laboratory and Simulation Investigation of Enhanced Coalbed Methane Recovery by Gas Injection", SPE 95947, presented at the 2005 SPE Annual Technical Conference and Exhibition held in Dallas, TX U.S.A., 8-12 October 2005.
3. Clarkson, C. R. and Bustin, R. M.: "Binary Gas Adsorption/Desorption Isotherms: Effect of Moisture and Coal Composition Upon Carbon Dioxide Selectivity Over Methane," *Int. J. Coal Geology* 42 (2000) 241-271.
4. Markham, E. C. and Benton, A. F.: "The Adsorption of Gas Mixtures by Silica," *J. Am. Chem. Soc.* (Feb. 1931) 497-507.

5. Wei, X. R., Wang, G.X., and Massarotto, P.: "A Review of Recent Advances in the Numerical Simulation for Coalbed Methane Recovery Process," paper SPE 93101 presented at the Asia Pacific Oil & Gas Conference and Exhibition, Jakarta Indonesia, 5-7 Apr. 2005.
6. Myers A.L. and Prausnitz J.M. "Thermodynamics of Mixed-gas Adsorption", AIChE J., 11, 121 (1965).
7. Talu O. , Li, J. and Mayers A.L. "Activity Coefficients of Adsorped Mixtures", Adsorption, 1, 103-112 (1993).
8. Nodzeriski, A.: "Sorptions and desorption of gases (CH₄, CO₂) on hard coal and active carbon at elevated pressures", Fuel Vol. 77, No. 11, pp. 1243-1246, 1998.
9. Chaback et al. "Sorptions Irreversibilities and Mixture Compositional Behavior During Enhanced Coal Bed Methane Recovery Processes" SPE 35622; 1996.
10. Seri-Levy, A. and Avnir, D. "Effects of Heterogeneous Surface Geometry on Adsorption," Langmuir 9 (1993) 3067-3076.
11. Perkins, T.K. and Johnston, O.C.: "A Review of Diffusion and Dispersion of Porous Media", SPE Journal, March 1963, pp. 70-84.

Table 1: Langmuir adsorption constants from Tang *et al.*[2]

| | Adsorption | | Desorption | |
|-----------------|--------------------------|------------|--------------------------|------------|
| | V _m (SCF/ton) | b (1/psia) | V _m (SCF/ton) | b (1/psia) |
| CH ₄ | 811 | 0.00237 | 543 | 0.0382 |
| CO ₂ | 1760 | 0.00521 | 1560 | 0.0158 |
| N ₂ | 272 | 0.00242 | 226 | 0.00574 |

Table 2: Parameters for estimation of the Peclet number.

| | |
|---|-------|
| Size of coal particles, cm | 0.025 |
| Pack length, cm | 25.0 |
| Pack diameter, cm | 4.25 |
| Total porosity, % | 37 |
| Flow rate, cm ³ /minute | 0.5 |
| Apparent diffusion coefficient cm ² /s | 5E-06 |

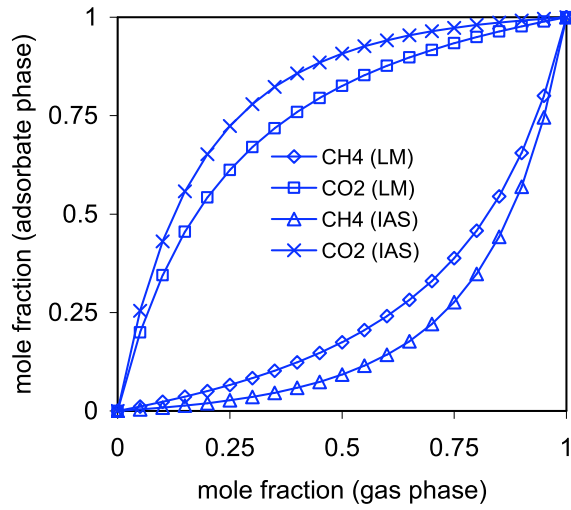


Figure 1: Composition of adsorbate phase as a function of gas phase composition for CH₄-CO₂ mixtures at 600 psia and 22°C.

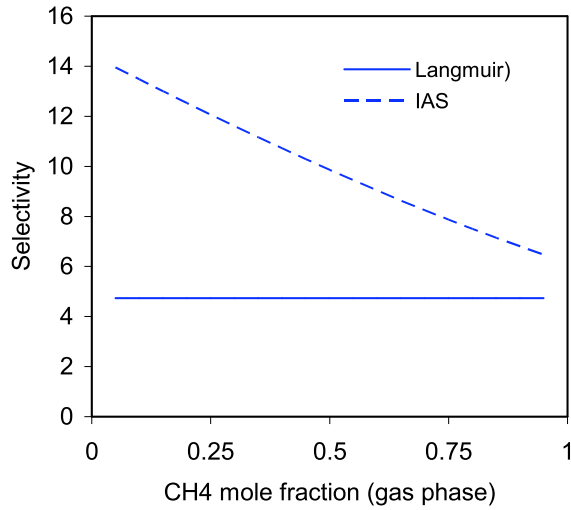


Figure 2: Selectivity of the CH₄-CO₂ binary at 600 psia and 22°C predicted by the IAS and Langmuir models.

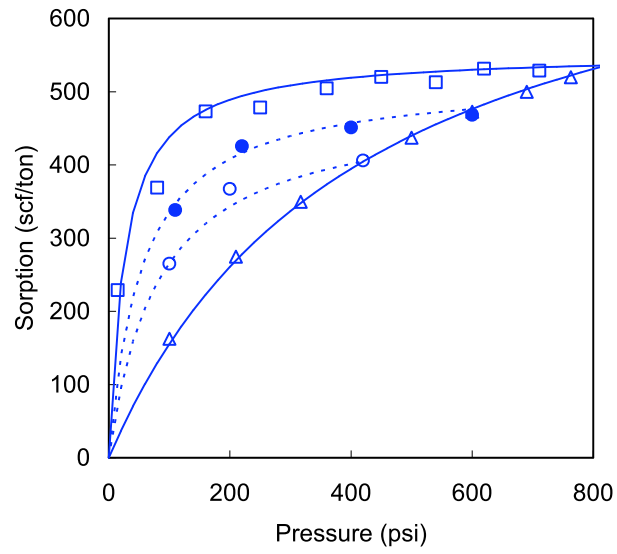


Figure 3: Comparison of hysteresis model and experimental observations of Tang *et al.* [2] for CH₄ at 22°C. Full lines represent Langmuir isotherms for the bounding curves based on experimental observations and broken lines are scanning curves generated from the hysteresis model.

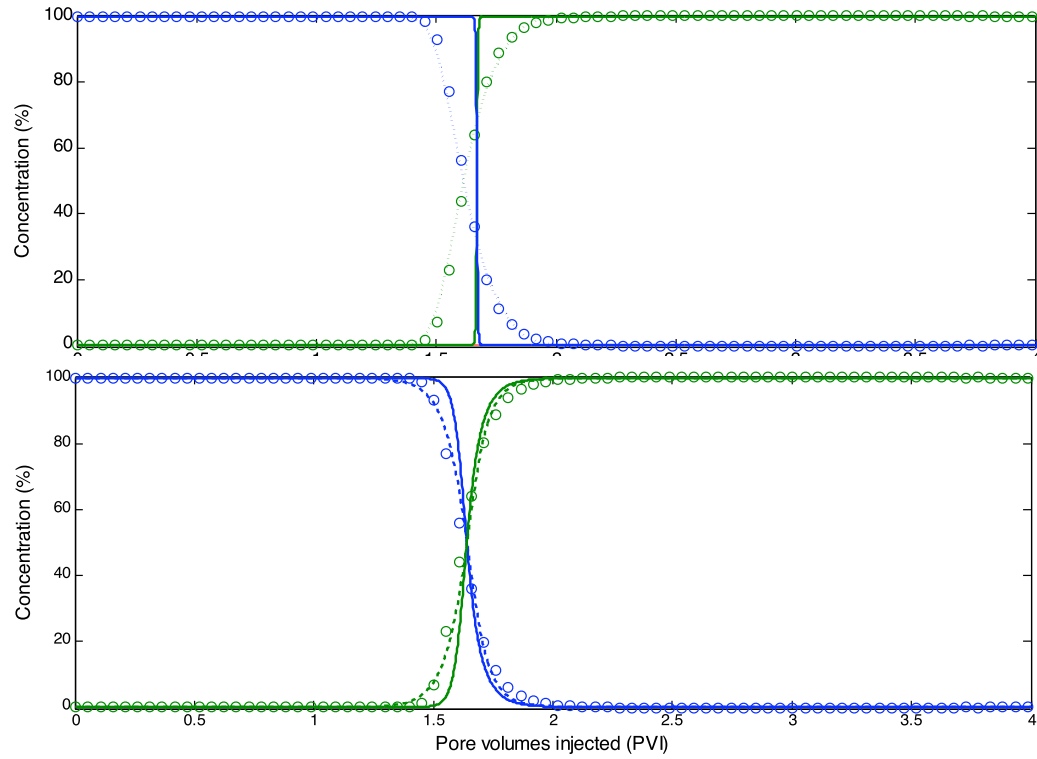


Figure 4: Comparison of the predicted effluent concentration from the Langmuir model (top panel) and IAS mc (bottom panel). Simulations were performed with (broken lines) and without (full lines) hysteresis included. F CO₂ displaces CH₄ at 600 psia and 22C. Experimental data (symbols) from Tang *et al.*[2]

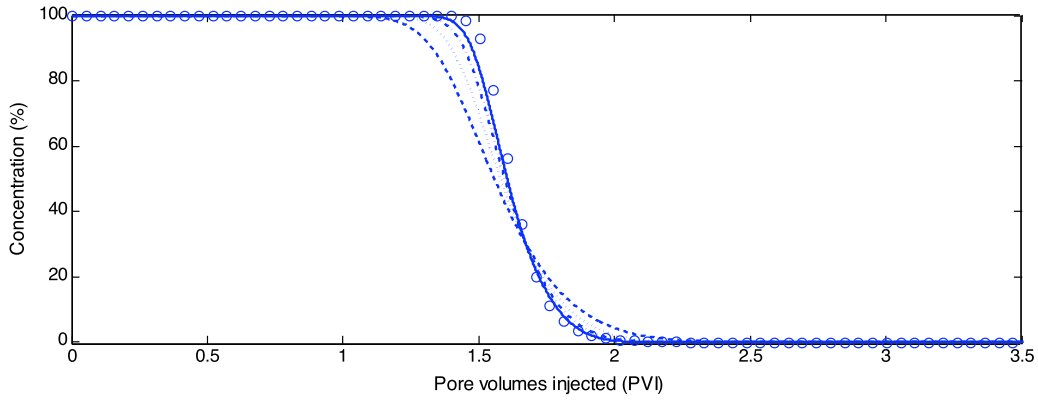


Figure 5: Convergence behavior of simulations (80, 160, 320 and 640 cells) with the Langmuir model ($Pe = 1250$) for displacement of CH_4 by pure CO_2 at 600 psia and 22C. Experimental data (symbols) from Tang *et al.* [2].

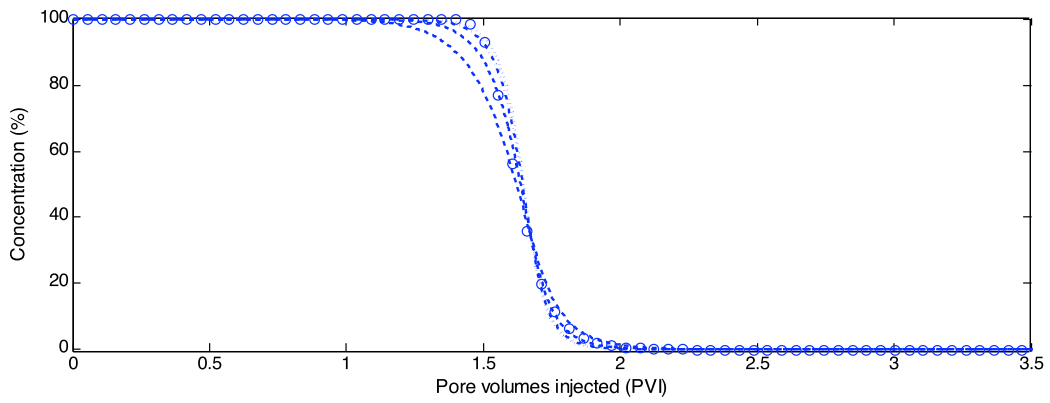


Figure 6: Convergence behavior of simulations (20, 40, 80 and 160 cells) with IAS model ($Pe = 100$) for displacements of CH_4 by pure CO_2 at 600 psia and 22C. Experimental data (symbols) from Tang *et al.* [2].

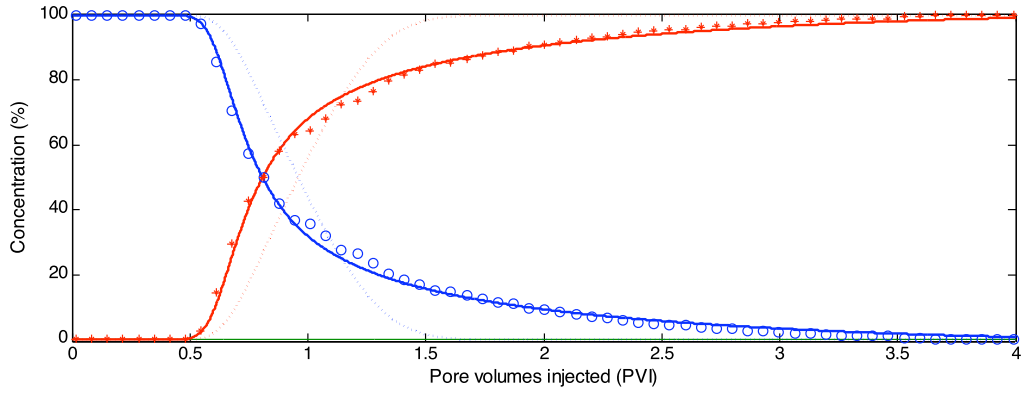


Figure 7: Comparison of the predicted effluent concentration from the Langmuir model with (full lines) and without (dotted lines) hysteresis included in the displacement calculation. Pure N_2 displaces CH_4 at 600 psia and 22C. Experimental data (symbols) from Tang *et al.*[2]

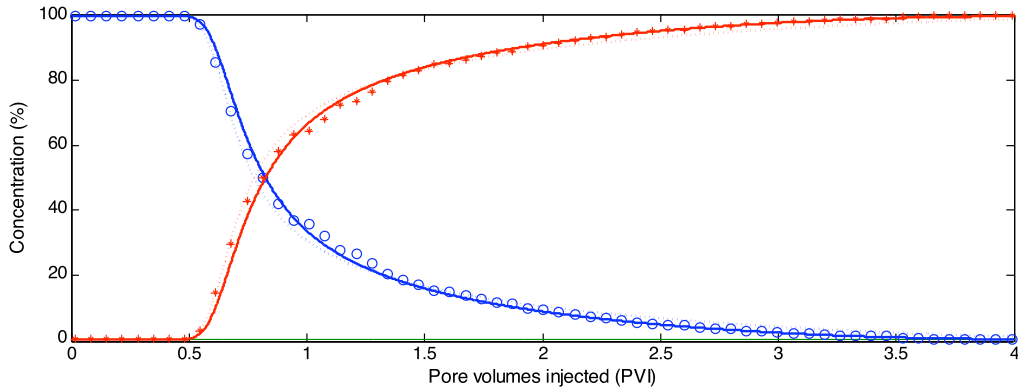


Figure 8: Comparison of predicted effluent composition from the IAS (dotted line) and LM (full lines) sorption models with experimental observations (symbols) from Tang *et al.*[2]. Pure N_2 displaces CH_4 at 22C and 600 psia.

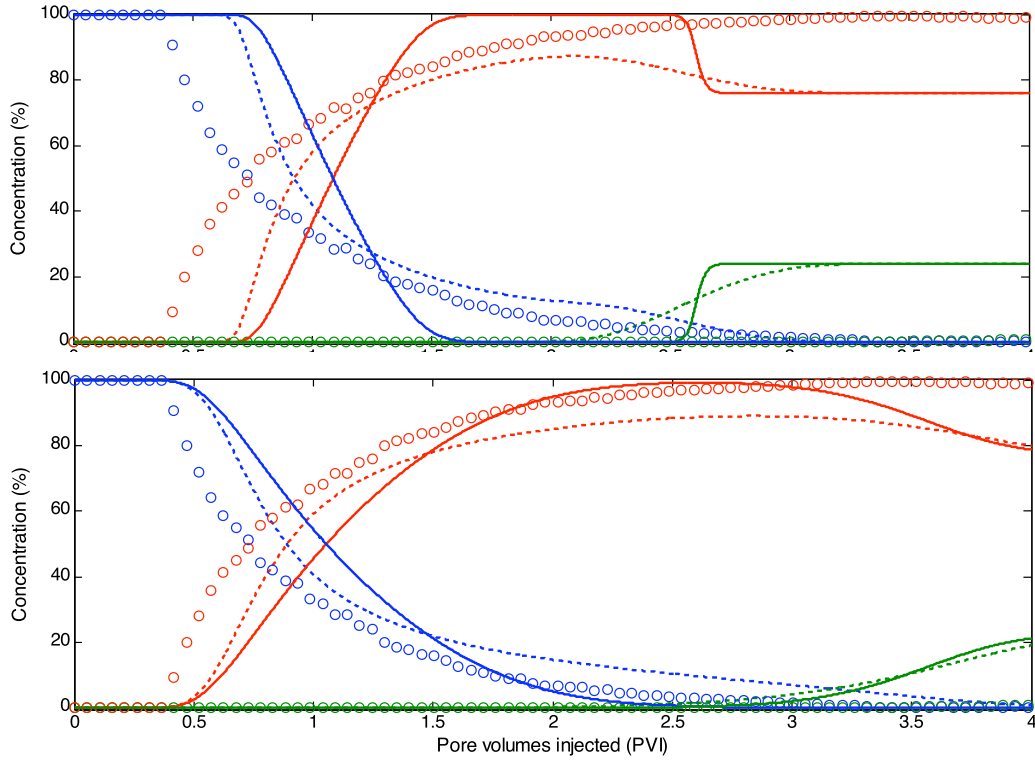


Figure 9: Ternary displacement A: 24% CO₂ and 76 % N₂ displaces pure CH₄ at 600 psia and 22C. Top panel: Langmuir model including hysteresis (dotted lines) and Langmuir model without hysteresis (full lines). Bottom panel: IAS model including hysteresis (dotted lines) and IAS model without hysteresis (full lines). Experimental observations (symbols) from Tang *et al.* [2].

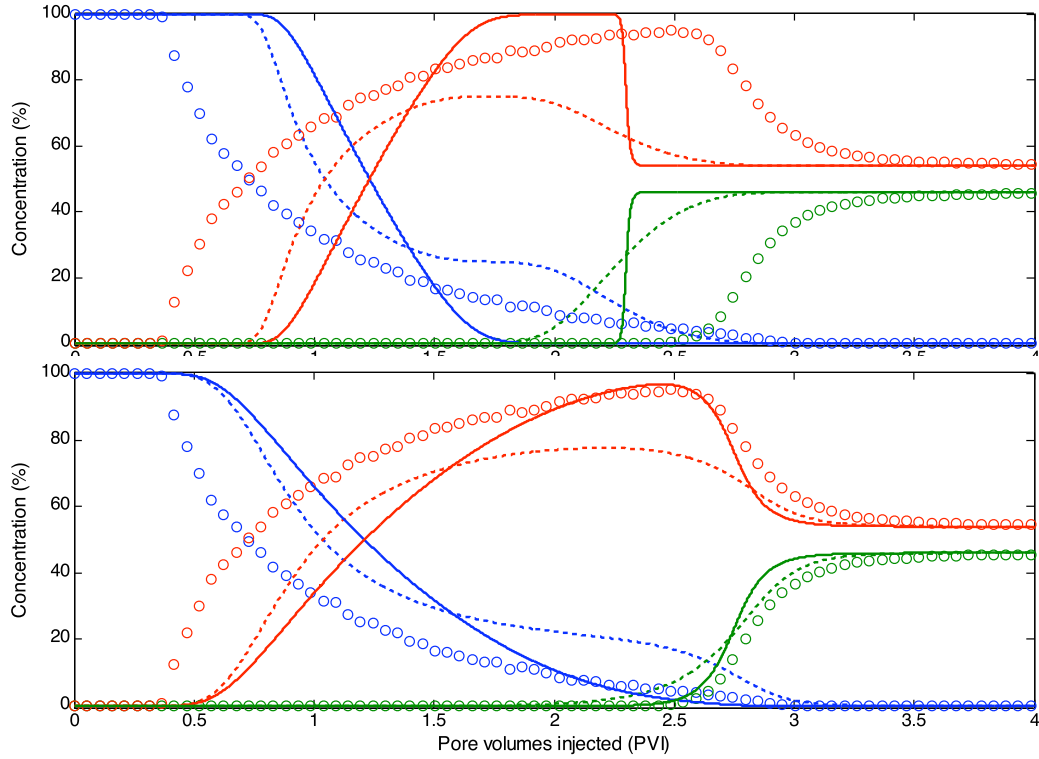


Figure 10: Ternary displacement B: 46% CO₂ and 54 % N₂ displaces pure CH₄ at 600 psia and 22C. Top panel: Langmuir model including hysteresis (dotted lines) and Langmuir model without hysteresis (full lines). Bottom panel: IAS model including hysteresis (dotted lines) and IAS model without hysteresis (full lines). Experimental observations (symbols) from Tang *et al.* [2].

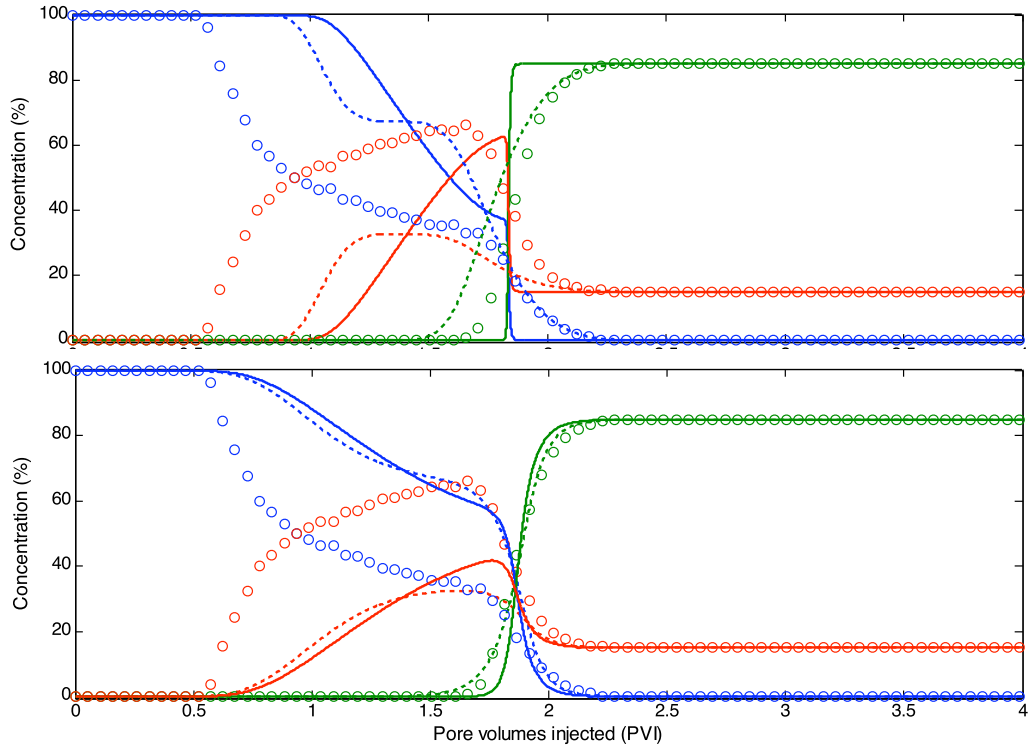


Figure 11: Ternary displacement C: 85% CO₂ and 15 % N₂ displaces pure CH₄ at 600 psia and 22°C. Top panel: Langmuir model including hysteresis (dotted lines) and Langmuir model without hysteresis (full lines). Bottom panel: IAS model including hysteresis (dotted lines) and IAS model without hysteresis (full lines). Experimental observations (symbols) from Tang et al. [2].

Multicomponent Sorption Modeling of Diffusive Transport in Coal Matrix

The internal structure of coal displays a variety of length scales. While gases are delivered to the coal matrix through cleats (fractures), the penetration of the matrix by CO₂ and the ultimate release of CH₄ from the matrix is governed by diffusion. We have begun a study of CO₂- N₂-CH₄ diffusion and simultaneous adsorption in coal matrix. Our work above has shown some benefits of CO₂- N₂ mixture injection. Ternary mixture diffusion is thus relevant to CO₂ sequestration enhanced coal bed methane (CO₂-ECBM) recovery. We have formulated, for the first time, a consistent model to incorporate adsorption along with diffusion of multicomponent (ternary) mixtures. Diffusive transport is based on Fickian diffusion and integrated with Maxwell-Stefan (MS) diffusion theory for multicomponent diffusion coefficients. The Maxwell-Stefan (MS) diffusion formulation deals rigorously with the interactions between multicomponent gas molecules. Other diffusive multicomponent simulation models assume the linearized theory of diffusion. We avoid this deficiency by formulating the Fickian diffusivities as functions of MS diffusivities and composition. The extended Langmuir approach is used to model the adsorption phenomenon in ternary gas mixtures. This assumption shall be relaxed at a later date. The model is found to be consistent qualitatively with simplified cases (single/two component).

Introduction

The literature describing gas transport in coal does not communicate that we have a genuine understanding of the penetration of CO₂ into the coal matrix as well as the enhanced production of methane. This lack of understanding originates partly because of the complicated pore structure of coalbed matrices and the difficulty in constructing multicomponent diffusion models coupled with adsorption. There are intricate networks of micro and macro pores, as well as the coupled physical mechanisms that take place as CO₂ is injected into coal seams. Broadly categorizing, physical mechanisms relevant to CO₂-ECBM recovery are multicomponent diffusion and adsorption. It is this interplay between the adsorption properties of coal surfaces and the advance of individual gas species that makes the theoretical and numerical modeling of this process such a difficult task. Coalbed heterogeneity and sorption induced permeability changes are some of the other factors that contribute towards the complexity of the ECBM procedure.

The ensuing work develops a coupled adsorption-diffusion model for multicomponent systems, starting with a binary system using the extended Langmuir approach and then gradually adding to the complexity, by incorporating ternary systems and using the IAS model in later stages. The aim of these simulation runs is to analyze and better understand the complex physical mechanisms of fracture to matrix transfer governing CO₂-ECBM recovery.

Multicomponent Adsorption and Diffusion

There is lack of substantial research in the form of published literature, experimental study and numerical modeling of multicomponent diffusive transport phenomena for the following reasons.

- The physics of multicomponent diffusion are complex and the resulting mathematical formulation required to solve numerically these non linear coupled partial differential equations makes the task look even more daunting.
- For non-ideal n_c component mixtures, there are (n_c-1) independent diffusion fluxes expressed by the generalized Fick's Law and $(n_c-1)^2$ diffusion coefficients[1,2]. In the past, attempts to measure multicomponent diffusion coefficients have been limited and most of the correlations provide an “effective diffusivity” that does not work well for many non-ideal cases.
- The pore structure of coal is highly heterogeneous and complex, with the pore size varying from a few Angstroms to over a micrometer in size. Consequently depending upon the pore size, different mechanisms for diffusion of an adsorbing gas tend to dominate.
- The non linear interplay between adsorption and diffusion makes the analytical solution of the governing equations almost impossible. In the absence of adsorption and assuming the “linearized theory of diffusion”, one can solve for the unknown concentrations.

Numerical Modeling–Approach

To begin the development of the model for gas diffusion in a coal matrix, we decompose the problem into special cases and proceed by adding gradually to the complexity. To the extent possible, results are compared to existing analytical solutions. The sensitivity of results to grid size, time step, and diffusivity coefficient is examined for each case, although not shown here. Cases examined to date include:

- one-dimensional, single-component diffusion without adsorption
- one-dimensional, single-component diffusion with Langmuir-type adsorption
- one-dimensional, binary system with adsorption described by the extended Langmuir equation
- one-dimensional, multicomponent diffusion with adsorption described by the extended Langmuir equation

Binary Mixture Diffusion-Adsorption: Once the numerical simulation for a single component undergoing simultaneous diffusion and adsorption was verified, complexity was increased by considering gas mixtures. The next step was to model a binary adsorption-diffusion system such as CO₂ and methane (CH₄). The CO₂ diffuses into the matrix while CH₄ desorbs and diffuses out in a direction countercurrent to the flow of CO₂. In the initial simulation runs, the Langmuir isotherm has been used and later compared against the IAS model.

The governing equations are mass balances for each species

$$\phi \frac{\partial C_1}{\partial t} + (1-\phi) \frac{\partial \left(\frac{\alpha_1 \beta_1 p_1}{1 + \beta_1 p_1 + \beta_2 p_2} \right)}{\partial t} = \phi D_{12} \frac{\partial^2 C_1}{\partial t^2} \quad (1)$$

$$\phi \frac{\partial C_2}{\partial t} - (1-\phi) \frac{\partial \left(\frac{\alpha_2 \beta_2 p_2}{1 + \beta_1 p_1 + \beta_2 p_2} \right)}{\partial t} = \phi D_{21} \frac{\partial^2 C_2}{\partial t^2} \quad (2)$$

where C_1 and C_2 are the free gas concentration of CO₂ and CH₄, respectively, α and β are the Langmuir constants (Eqs 1, 2) and D_{12} , D_{21} are the Fickian binary diffusion coefficients. As the diffusion is countercurrent, the Fickian diffusivities are equal in magnitude and assumed to be constant. Initially the coalbed is saturated with CH₄ and CO₂ is maintained at constant injectant concentration at one end of the domain while a no flux boundary condition is enforced at the other end. Coal has greater affinity towards CO₂ and as a result it preferentially adsorbs into the coalbed while with decreasing partial pressure, CH₄ desorbs and is recovered as a free gas.

The gases are assumed to behave as ideal and as a result the partial pressure, p_i of component i in the free gas phase is

$$p_i = C_i RT \quad (3)$$

Eqs. 1 and 2 are coupled non-linear partial differential equations in C_1, C_2 and therefore an iterative procedure has to be used to compute these values over each grid location and for each time step. A non-linear Newton- Raphson technique has been implemented and for each grid position, the Jacobian (J) given by Eq. 4 iterated until the residual tolerance is reached. The composition at a particular time step serves as the initial guess value for the same location, for the next time step.

$$J = \begin{pmatrix} 1 + \left(\frac{1-\phi}{\phi} \right) \frac{(\alpha_1' + \alpha_1' \beta_2' C_{2,i})}{(1 + \beta_1' C_{1,i} + \beta_2' C_{2,i})^2} & - \left(\frac{1-\phi}{\phi} \right) \frac{(\alpha_1' \beta_2' C_{1,i})}{(1 + \beta_1' C_{1,i} + \beta_2' C_{2,i})^2} \\ \left(\frac{1-\phi}{\phi} \right) \frac{(\alpha_2' \beta_1' C_{2,i})}{(1 + \beta_1' C_{1,i} + \beta_2' C_{2,i})^2} & 1 - \left(\frac{1-\phi}{\phi} \right) \frac{\alpha_2' + \alpha_2' \beta_1' C_{1,i}}{(1 + \beta_1' C_{1,i} + \beta_2' C_{2,i})^2} \end{pmatrix} \quad (4)$$

$$\alpha' = \alpha \beta RT \quad (5)$$

$$\beta' = \beta RT \quad (6)$$

where $C_{1,i}$, $C_{2,i}$ are the unknown concentrations at t time-step and grid location i ; α , β are the Langmuir constants.

Figure 1 illustrates the development of concentration profiles of CO_2 and CH_4 with time. The length of the domain is 10 cm and the total time simulated is 200 seconds. Because of the countercurrent diffusion phenomena taking place, the concentration profiles for the two components are quite symmetric. Figure 2 illustrates the effect of adsorption on the transport of methane through the gas phase.

The extended Langmuir adsorption model has been used throughout the simulation study to this time, and though apparently accurate for 2 component systems, it is interesting to *compare* the extended Langmuir model versus the *IAS model* [3]. The separation factor or selectivity ratio, for a binary gas adsorption system is defined as [4]

$$\alpha_{ij} = \frac{(x/y)_i}{(x/y)_j} \quad (7)$$

For the extended Langmuir isotherm, the separation factor is the ratio of adsorption equilibrium constants for the pure component isotherms [4] and is therefore independent of the concentration and total pressure. The assumption, however of a constant separation factor is not necessarily accurate for all systems [4]. An increasing selectivity for the most strongly adsorbed component with decreasing concentration of that component is generally observed [3]. Based upon this theoretical background it is interesting to compare the concentration of the adsorbates as predicted by the two models.

The procedure outlined below is the one developed by Jessen et al. [5]. The IAS model assumed that the gas phase behaves as an ideal gas and that the adsorbate phase behaves like an ideal mixture. Thus the gas phase and adsorbed phase are related by the expression

$$y_i P = x_i p_i^o \quad (8)$$

where p_i^o is the pressure corresponding to a pure adsorbate phase at the spreading pressure of the true adsorbate phase. Eq. 6 is simplified by assuming that the pure component adsorption behavior is represented by the Langmuir isotherm. The integral is simplified as

$$\pi_i^* = V_{m,i} \ln(1 + \beta_i p_i^o) \quad (9)$$

The initial guess for the adsorbate composition given the free gas composition is computed using the Langmuir isotherm expression

$$a_i = \frac{\alpha_i \beta_i p_i}{1 + \sum_{j=1}^{n_c} \beta_j p_j}$$

$$x_i = \frac{a_i}{\sum_{j=1}^{n_c} a_j}$$
(10)

The x_i computed is then substituted in Eq 8 and P_i^0 evaluated which is then used in Eq 9 to calculate the spreading pressure Π , this being done over each iteration until it satisfies the condition

$$\dot{\Pi}_i - \dot{\Pi}_i$$
(11)

This is because finally at equilibrium, the spreading pressure evaluated for each component at the corresponding reference pressure (P_i^0) must be equal. The convergence condition is decided by Eq 11 and once the residual tolerance is reached, the resulting x_i values are those generated using the IAS model. It is interesting to note that the two different adsorption models predict adsorbate compositions that differ quite substantially and this difference is pertinent even at short time scales, thus highlighting the importance of careful selection of an adsorption model (Fig. 3)

Diffusion-Adsorption of Multicomponent Gas Mixtures: In the multicomponent domain, it is the diffusion of gases that is most intriguing. Fick's law of diffusion is widely used to describe the coal bed gas diffusion process because of its simplicity. If used in its actual form then its validity is severely restricted and even misleading in many practical situations where the diffusion coefficients of the fluid species depend on composition. The Maxwell-Stefan (MS) diffusion formulation better applies to multicomponent fluid diffusion and deals rigorously with the interactions between multicomponent gas molecules.

In our case, the simplicity of the Fick diffusion expression to describe the flux of a component has been retained but at the same time the MS approach has been incorporated to describe the transient multicomponent gas diffusion dynamics.

The expression of the molecular diffusion flux of an n_c multicomponent mixture is given by the generalized Fick's law

$$\mathbf{J} = -\mathbf{D} \nabla \mathbf{C} \quad (12)$$

where

$$\mathbf{J} = \begin{pmatrix} J_1 \\ J_2 \\ \vdots \\ J_{n_c-1} \end{pmatrix}, \quad \mathbf{C} = \begin{pmatrix} C_1 \\ C_2 \\ \vdots \\ C_{n_c-1} \end{pmatrix} \quad \text{and} \quad \mathbf{D} = \begin{pmatrix} D_{1,1} & D_{1,2} & \cdots & D_{1,n_c-1} \\ D_{2,1} & D_{2,2} & \cdots & D_{2,n_c-1} \\ \vdots & \ddots & \ddots & \vdots \\ D_{n_c-1,1} & \ddots & \cdots & D_{n_c-1,n_c-1} \end{pmatrix} \quad (13)$$

Eq. 12 in expanded form is

$$J_i = \sum_{j=1}^{n_c-1} D_{i,j} \nabla x_j, \quad i=1, 2, \dots, n_c-1 \quad (14)$$

The diagonal entries $D_{i,i}$; $i=1,2,\dots, n_c-1$ are the main diffusion coefficients and the off diagonal entities $D_{i,j}$; $i,j=1,2,\dots, n_c-1$ ($i \neq j$) are the cross diffusion coefficients, that are generally non zero and not symmetric ($D_{i,j} \neq D_{j,i}$). Also the coefficients can take positive or negative values. The diffusion flux should satisfy the constraint equation [1,2]

$$\sum_{i=1}^{n_c} J_i = 0 \quad (15)$$

Thus, the diffusion flux for the n_c component can be calculated using Eq 15.

Once the diffusion fluxes have been defined, the diffusion coefficients need to be estimated. Diffusion in micropores is strongly temperature and concentration dependent. It is here that Maxwell-Stefan (MS) formulation is integrated with Ficks Law and the binary diffusivities D_{ij} used to compute the Fickian diffusivities. For our ternary system, the elements of \mathbf{D} are given as

$$D_{11} = D_{13}(x_1 D_{23} + (1-x_1) D_{12})/S \quad (16a)$$

$$D_{12} = x_1 D_{23}(D_{13} - D_{12})/S \quad (16b)$$

$$D_{21} = x_2 D_{13}(D_{23} - D_{12})/S \quad (16c)$$

$$D_{23} = (x_2 D_{13} + (1-x_2) D_{12})/S \quad (16d)$$

where

$$S = x_1 D_{23} + x_2 D_{13} + x_3 D_{12} \quad (17)$$

Note that the numerical values of D_{ij} depend on the particular choice of system numbering and do not have any physical significance to i - j interaction. In our case, component 1 is CO₂, component 2 is N₂ and component 3 is CH₄.

The diffusion and adsorption of gases takes place within a linear 1 D geometry initially saturated with CH₄, CO₂, and N₂ at concentrations similar to a coalbed gas. For the 3 component adsorption-diffusion problem, there are two species balance equations (Eqs. 18 and 19) and one overall mass balance relation (Eq. 20).

$$\phi \frac{\partial C_1}{\partial t} + (1-\phi) \frac{\partial}{\partial t} \left(\frac{\alpha_1' C_1}{1 + \beta_1' C_1 + \beta_2' C_2 + \beta_3' C_3} \right) = \phi \left(\frac{\partial}{\partial x} \left(D_{11} \frac{\partial C_1}{\partial x} + D_{12} \frac{\partial C_2}{\partial x} \right) \right) \quad (18)$$

$$\phi \frac{\partial C_2}{\partial t} + (1-\phi) \frac{\partial}{\partial t} \left(\frac{\alpha_2' C_2}{1 + \beta_1' C_1 + \beta_2' C_2 + \beta_3' C_3} \right) = \phi \left(\frac{\partial}{\partial x} \left(D_{21} \frac{\partial C_1}{\partial x} + D_{22} \frac{\partial C_2}{\partial x} \right) \right) \quad (19)$$

$$\phi \frac{\partial (C_1 + C_2 + C_3)}{\partial t} + (1-\phi) \frac{\partial}{\partial t} \left(\frac{\alpha_1' C_1 + \alpha_2' C_2 + \alpha_3' C_3}{1 + \beta_1' C_1 + \beta_2' C_2 + \beta_3' C_3} \right) = 0 \quad (20)$$

The initial conditions (IC) and the boundary conditions (BC) for the transient transport phenomena are that initially the concentration of CO₂ and N₂ (i.e. C_1 and C_2) are low everywhere in the domain and the matrix is rich in CH₄ (i.e., C_3). A CO₂/N₂ mixture is introduced at one end while CH₄ diffuses countercurrent to the flux of boundary gases. These initial and boundary conditions approximate the flow of injection gas through the fracture (cleat) network of a coal. Results are given in Figs 4 to 6.

Summary

Effect of Grid Size

The behavior in the boundary layer is the main concern because of the discontinuity in concentration that exists at the cleat/matrix boundary. Nevertheless, the finite difference approximation appears to be acceptable at the boundary even though the gradients are large.

Effect of MS approach

In order to model successfully and realistically multicomponent diffusion scenario, it is almost essential to incorporate the MS approach. Application of the linearized theory would lead to significant deviation. This is because there is a strong dependence of diffusivity on the concentration in a Langmuirian sorbed phase.

Numerical stability and convergence

The numerical formulation is found to work for a range of MS diffusivity values. The differential equations describing the model are non-linear and must be solved numerically. The continuum equations were solved in the x-coordinate by a semi-implicit finite difference approximation. This leads to a set of coupled discretized system of equations that were solved for different spatial locations integrated in time using the non-linear form of Newton Raphson iteration technique.

References

1. Cussler, E.L.: "Diffusion Mass transfer in fluid systems", Cambridge University Press, U.S.A (1986).
2. Taylor, R. and Krishna, R.: "Multicomponent Mass Transfer", Wiley Series in Chemical Engineering, U.S.A (1993).
3. Myers, A.L., and Prausnitz, J.M.: "Thermodynamics of Mixed-Gas Adsorption", AIChE Jr. 11, 121-127 (1965).
4. Ruthven, D. M.: Principles of Adsorption and Adsorption Processes, New York: Wiley Interscience, 1984.
5. Jessen, K., Lin, W., and Kovscek, A.R.: "Multicomponent Sorption Modeling in ECBM Displacement Calculations", SPE 110258, presented at the 2007 SPE Annual Technical Conference and Exhibition held in Anaheim, CA U.S.A., 11-14 November 2007.
6. Loos, W.P., Verheijen, J.T., and Moulijn, J.A.: "Numerical Simulation of the Generalized Maxwell-Diffusion Model for Multicomponent Diffusion in Microporous Sorbents", presented as a poster at the International Symposium "Zeolite Chemistry and Catalysis", Prague, September 8-13, 1991.

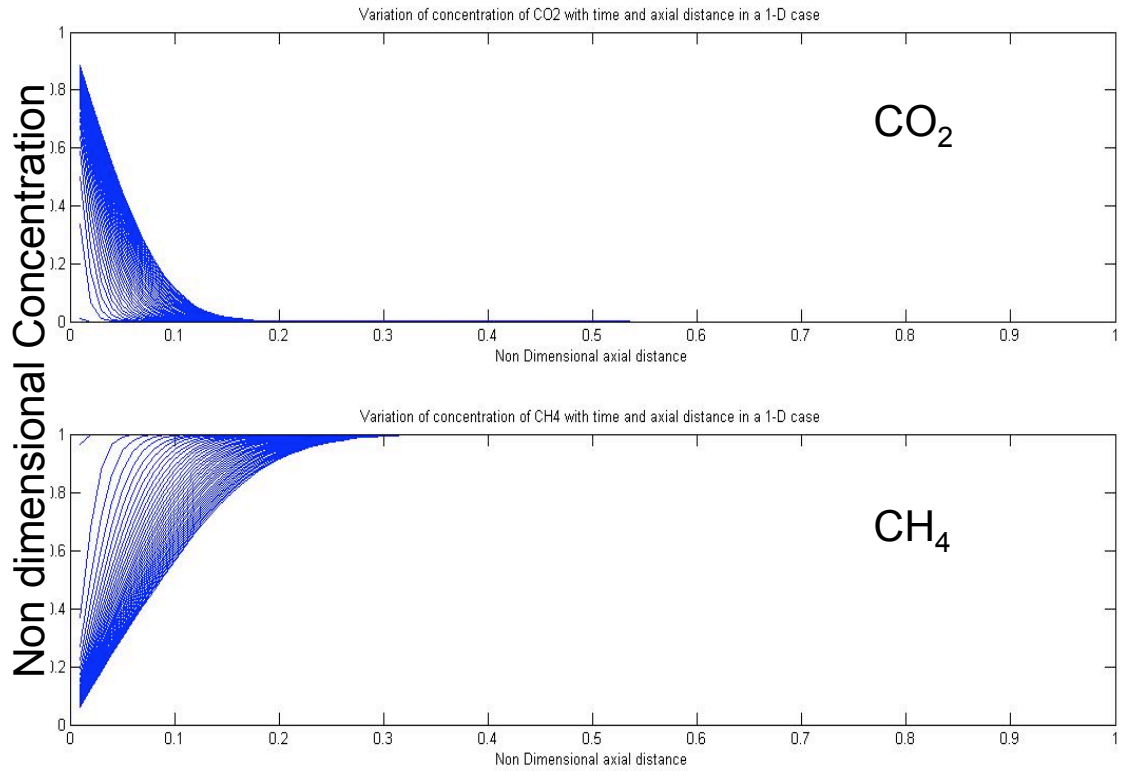


Figure 1: Concentration distributions for a binary system undergoing simultaneous countercurrent diffusion and adsorption as described by the extended Langmuir equation. Profiles are plotted at 5 s intervals. The domain length is 10 cm.

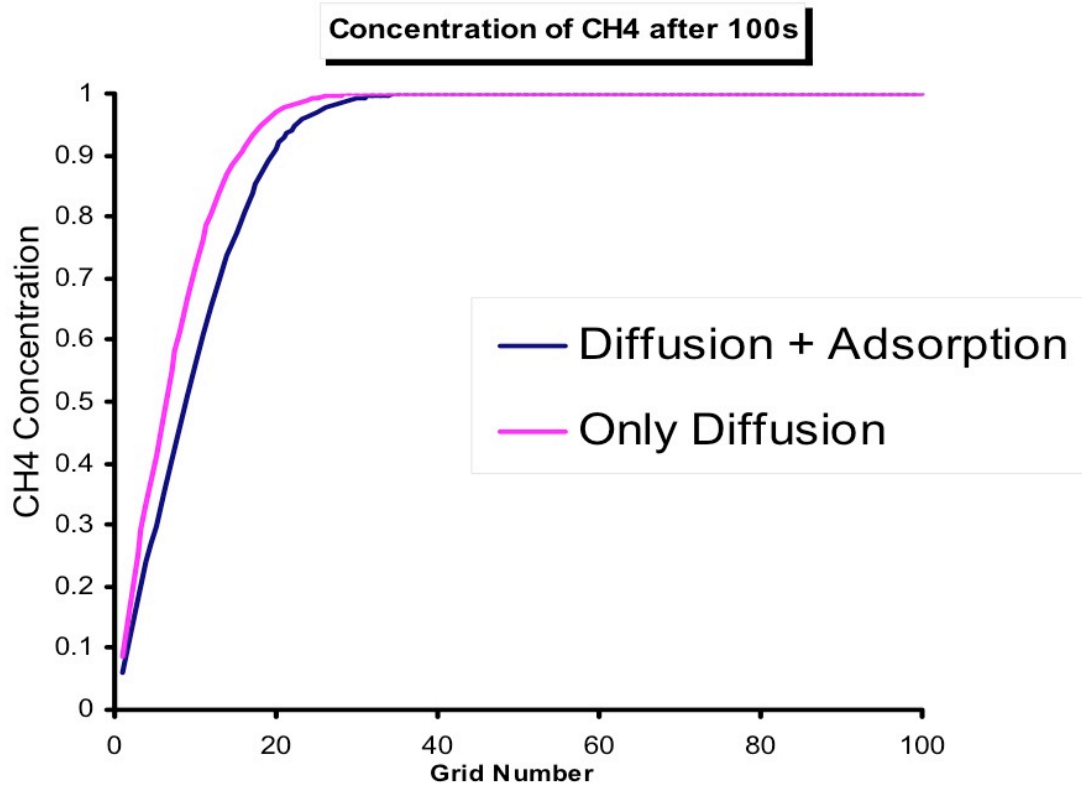


Figure 2: Comparison of methane concentration profiles for cases with and without adsorption to the solid phase. Total elapsed time is 100 s. Other conditions are identical to Fig. 1.

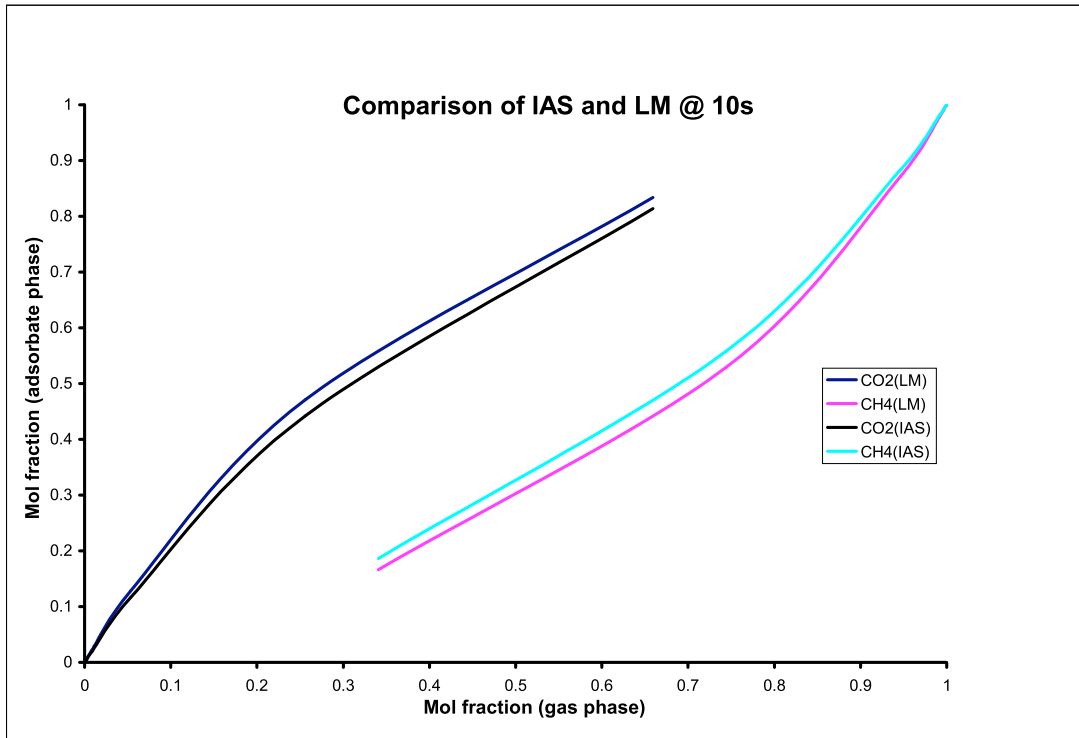


Figure 3: Concentration distributions of the adsorbed phase versus the gas phase for a binary system undergoing simultaneous countercurrent diffusion and adsorption. Multicomponent adsorption is described alternately by the extended Langmuir equation and ideal adsorbed solution (IAS) models. Profiles are plotted at 10 s elapsed time. The domain length is 10 cm.

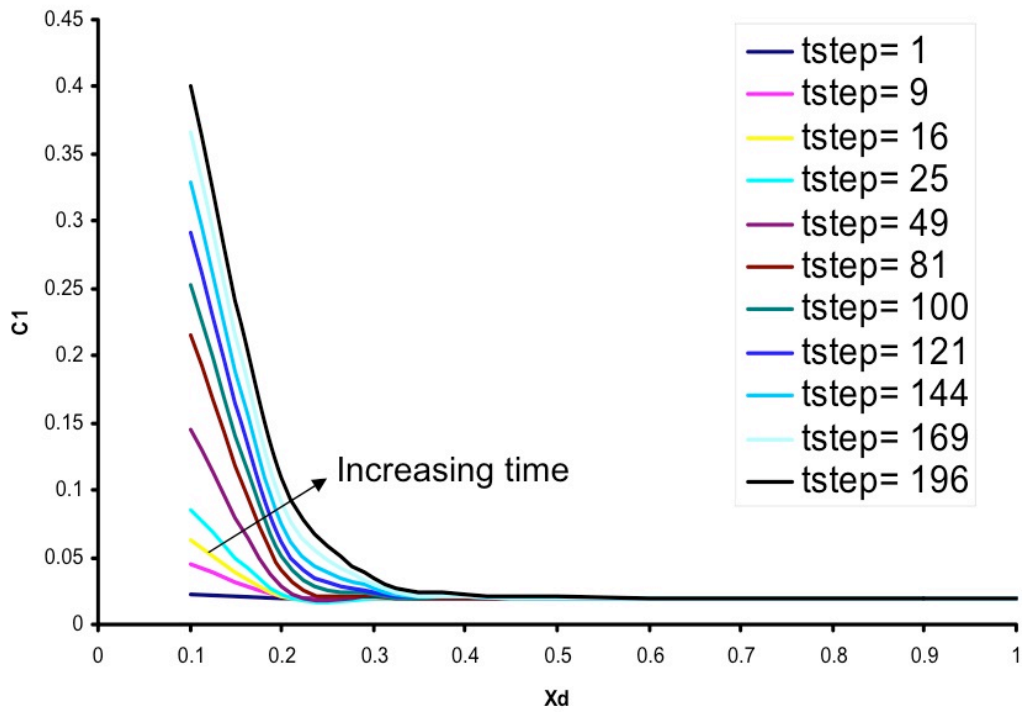


Figure 4: Concentration distribution of gas-phase carbon dioxide for a ternary system undergoing simultaneous countercurrent diffusion with adsorption. Domain size is 10 mm. Input Maxwell-Stefan diffusivities are $D_{13} = 0.02$, $D_{12}=0.03$, and $D_{23}=0.01$ mm²/s.

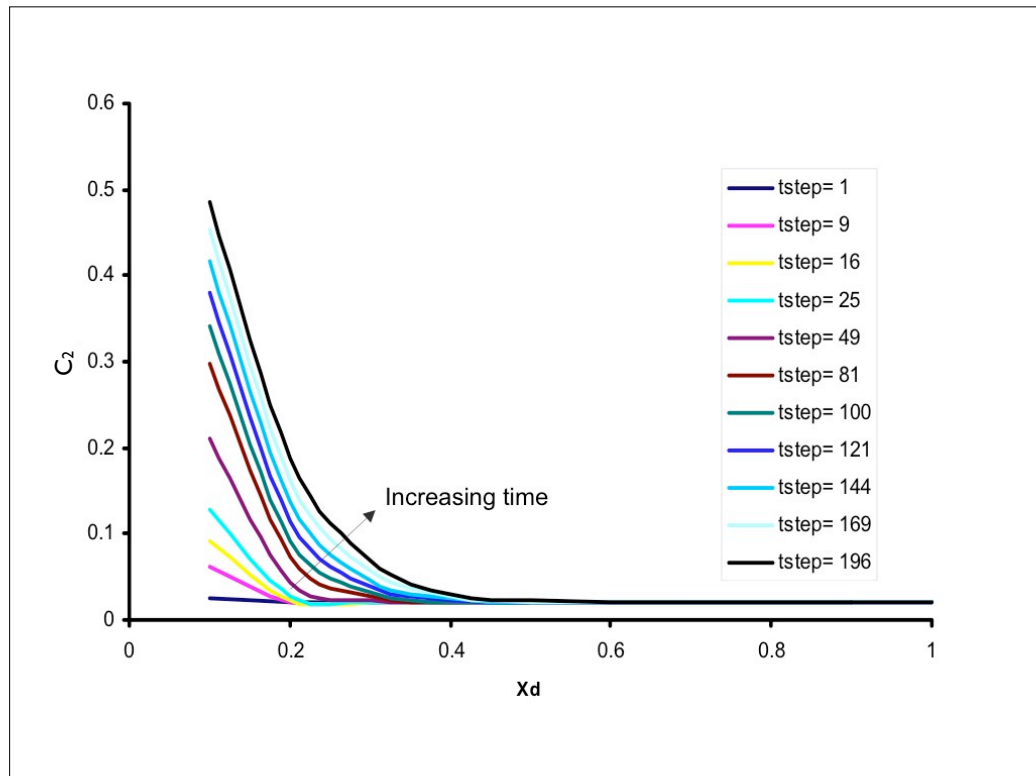


Figure 5: Concentration distribution of gas-phase nitrogen for a ternary system undergoing simultaneous countercurrent diffusion with adsorption. Domain size is 10 mm. Input Maxwell-Stefan diffusivities are $D_{13} = 0.02$, $D_{12}=0.03$, and $D_{23}=0.01$ mm²/s.

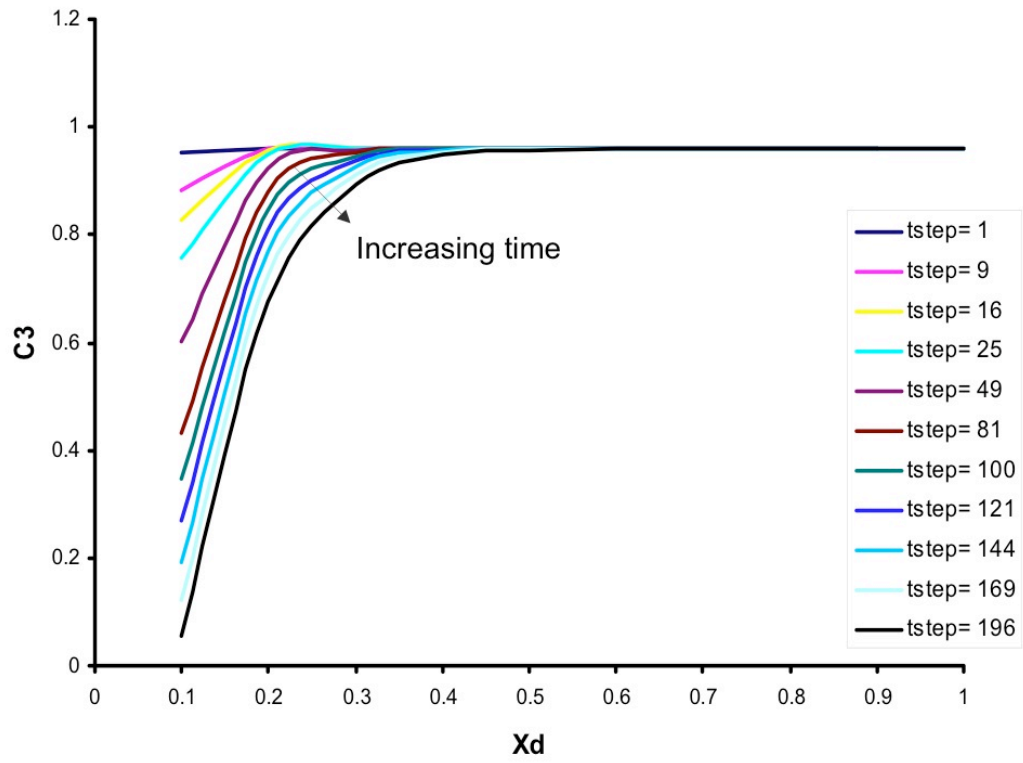


Figure 6: Concentration distribution of gas-phase methane for a ternary system undergoing simultaneous countercurrent diffusion with adsorption. Domain size is 10 mm. Input Maxwell-Stefan diffusivities are $D_{13} = 0.02$, $D_{12}=0.03$, and $D_{23}=0.01$ mm²/s.

Field Study and Analysis of a Coal Bed Fire

Introduction

Uncontrolled subsurface fires in coalbeds account for significant releases of CO₂ to the atmosphere. Coalbed fires are burning in many locations in China, Indonesia, India, and the United States (Stracher and Taylor, 2004). They can be started naturally by forest fires that burn near an outcrop, by lightning strikes, or by spontaneous reactions of pyrites (DeKok, 1989). Forest fires in Indonesia in 1997 and 1998 ignited hundreds of coal fires at outcrops (Brown, 2003). Fires that propagate into the subsurface can also be started by human activities. A subsurface fire near Centralia, Pennsylvania, for example, was started when the local government decided to burn an unregulated trash dump in an abandoned strip mine to reduce trash volume and control rodents in May, 1962. The fire ignited an anthracite outcrop, eventually connected to and spread through underground tunnels, and has been burning since. Fissures created by the coal fire emit assorted hot gases, some of which are toxic. A combination of subsidence and emissions from fissures has caused the town of Centralia to be abandoned by all but a few residents.

A large active coalbed fire in Wuda, China has been documented (Dai et al., 2002). One recent estimated annual loss of coal due to this fire is around 200,000 tons, which is equivalent to a yearly emission of 1.5 Mt of CO₂ (Kunzer et al., 2005). Another published estimate claims that Wuda and other coalbed fires in China can consume up to 200 million tons of coal per year (Rosema et al., 1993) and account for as much as 2–3% of the annual world emission of atmospheric CO₂ from burning fossil fuels (Cassells and van Genderen, 1995; Zhang and Kroonenberg, 1996). Thus, estimates of total CO₂ emissions are large enough to suggest that developing ways to control them might provide an additional way to reduce emissions of CO₂ to the atmosphere.

In this section we outline work done to characterize a subsurface fire at a location in the San Juan Basin near Durango, Colorado. The fire was discovered in 1998 and continues to burn today, but anecdotal evidence from suggests that the fire may have been burning for decades. The research effort described here is an attempt to understand the geometry and flow setting of the fire so that pressure gradients that drive the flow of oxygen to the combustion zone can be estimated. That information should allow an assessment of whether it might be possible to disrupt that flow and extinguish the subsurface fire.

Field Measurements

The following information has been gathered and field observations and measurements have been made:

Local geologic setting. The field site is near Durango, Colorado, on the northwest edge of the San Juan Basin. The coal layer that is burning is in the Fruitland Formation (Fassett, 2000). It is one of three coal layers in the Fruitland separated by shales, sandstone, and clay layers, though at the specific location, the top two coal layers have been eroded away. The coal is overlain by a thin, fractured sandstone (about 0.3 m thick

below about 0.2 m of topsoil) and underlain by the Pictured Cliffs sandstone. The coal layer dips to the southeast at about 11 degrees. The depth to the top of the coal in the zone that is burning now is about 15 m, and the coal layer thickness is approximately 5-7 m.

Surface topography and surface expressions of the fire. Measurements of surface elevation were made by walking the fire area with a pack-mounted GPS. Locations of numerous surface fissures were also measured. Directions of the surface fissures were compared with reported observations of coal cleat directions and the directions of regional fracture sets in the sandstone that lies just below the layer of topsoil (about 30 cm thick). Those observations indicate the most common fissure directions are consistent with the regional stress fracture sets, which suggests that the surface fissures reflect opening of pre-existing fractures in the sandstone. Figure 1 shows measured surface contours and the locations of observed fissures.

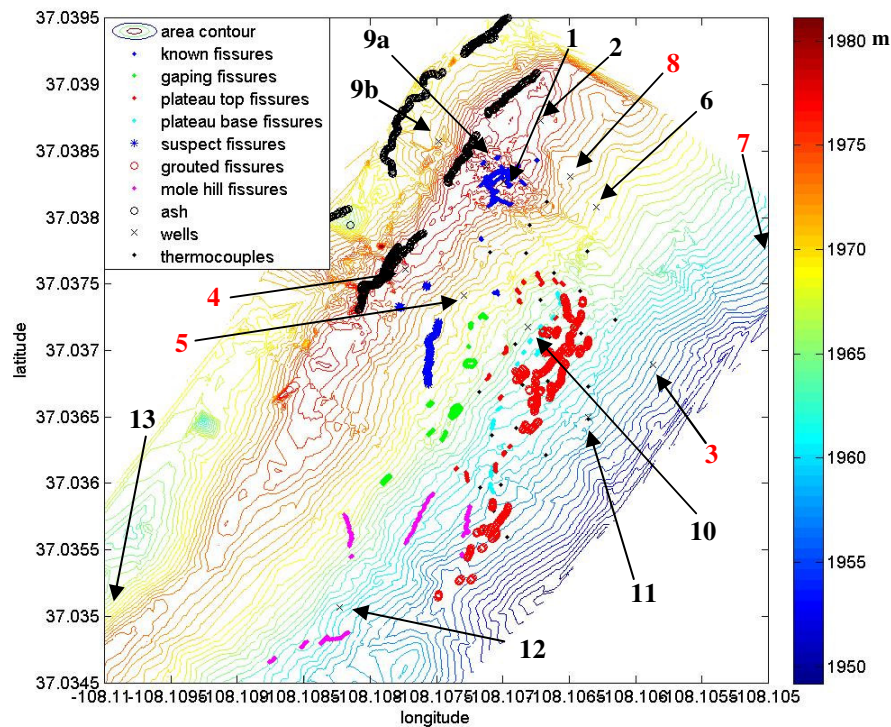


Figure 1. Surface topography and fissure locations. Black dots show the locations of surface ash and “clinkered” sandstones (those that show evidence of thermal alteration). Small black diamonds show locations of previously installed thermocouples, and x’s indicate locations of recently drilled holes, some of which have thermocouples installed.



Figure 2. (a) a gaping fissure with a 6ft adult inside, (b) a molehill fissure showing buckling rocks, and (c) an active narrow fissure.

Three types of fissures have been observed (see Figure 2): gaping fissures, molehill fissures, and narrow fissures. Figure 2a shows an example of a gaping fissure; this particular fissure is wide enough for an adult to climb inside. Typical gaping fissures are 8~12 inches wide at the surface and wider below the topsoil level, and it appears that gaping fissures are connected to each other in the subsurface. These fissures do not show temperatures above ambient. Figure 2b shows an example of a molehill fissure, in which buckling rocks create an acute angle at the apex of the “molehill,” and the ground may or may not be fractured at the peak. At molehill fissures with a visible fracture gases exiting with a temperature as high as 290 °C (550 °F) have been observed. Figure 2c is an example of narrow fissures that cover most of the field. Some of these fissures are active, emitting combustion gases with temperatures as high as 1080 °C (1970 °F), while others, presumably those that are above regions where coal is no longer actively burning and show no temperature anomaly. Presumably any of the fissures that are not actively emitting hot gases could be a source of oxygen to support combustion of unburned coal. Narrow fissures emitting hot gases frequently show precipitation of elemental sulfur and ammonium chloride crystals, an indication that oxygen concentrations in the hot gases are low.

There are two additional features besides the fissures that are observed on the field, and these are deposits of ash and clinkered sandstone rocks. The term, “clinker” is used to describe rocks that show evidence of thermal alteration. In this case the sandstones that are said to be clinkered are reddish in color and extensively fractured. The deposits of ash are found on the NW region of the field, and clinkered rocks are found near the ash. Figure 1 shows that the ash and clinkered rocks are found in an area where the coal would have outcropped had it not been burned.

Drillhole information. Fourteen holes were drilled to determine accurately the depth of the top of the coal, to allow installation of thermocouples, to collect cuttings as indicators of lithology and burned and unburned coal, to allow logs to be run for some holes, and to core one hole. See Figure 1 for hole locations. Two holes (1 and 9a) had to be

abandoned at depths of 8 and 13 m because very high temperatures were encountered. Cuttings were sampled from all of the holes, though holes 1, 10, and 13 showed almost no returns of cuttings, an indication of voids in the subsurface. Holes 3 and 7 showed no evidence of combustion in cuttings, core, or logs. Other holes all showed some ash returns or voids. Hole 7 was cored to a depth of 24 m. It showed a coal seam thickness of about 8 m.

Well logs were obtained for holes 3, 4, 5, 7, and 8. Three instruments, caliper, gamma ray and density logs were run. Because shales in the area show inconsistent trace amounts of radioactive materials, gamma ray logs are typically not as reliable in the San Juan basin as density logs to distinguish different lithologies. Density logs clearly show the interface between coal and sandstone, but distinguish less clearly between coal and ash. Example logs for holes 3 and 4 are shown in Figures 3 and 4. Hole 3 is in an unburned zone. Figure 3 shows that the density log gives a clear indication of the depth and thickness of the coal. Figure 4 shows evidence of an ash zone above a thin zone of unburned coal, which lies just above the Pictured Cliffs sandstone.

Temperature information. Thermocouple measurements in drill holes have been collected intermittently since 2001, and surface infrared measurements have been used to identify fissures that emit hot gases. Those data show that the combustion zone has continued to propagate during the time for which measurements are available. Figures 5 and 6 show the earliest and most recent temperature measurements contoured approximately inside the region for which observations are available. Depths at which the thermocouples emplaced prior to 2007 are not well documented, but even so, the movement of the combustion zone and the increase in temperature in the hottest areas is clear from comparison of Figures 5 and 6.

Effluent gas analyses. Gas samples were collected from drillholes 1, 2, 7, 9, and 13, and the compositions were determined by gas chromatography. The composition data are compared in Figure 7 with similar data for wells located nearby but well away from the combustion zone. The wells outside the coal fire area showed gas compositions that are roughly 50% CO₂ and 50% methane. N₂ was not present in those samples. The gas composition for hole 7, in which no evidence of combustion was found, showed a similar composition. All other samples showed significant quantities of N₂, an indication that air is being drawn into the combustion zone. The spatial distribution of samples containing N₂ suggests that the source of the air for combustion is relatively close to the combustion zone, either fissures that are now inlets for air or possibly former coal outcrops on the northwest side of the coal fire area. Those observations are consistent with flow of air through a variety of inlets driven by the density difference of the hot gases exiting the active fissures.

Carbon isotope data were obtained for a sample from hole 1, which is located close to the zone where the coal is burning now. Those data are compared in Table 1 with similar data for the gas wells shown in Figure 7. Those data indicate that the isotope signature of the CO₂ and CH₄ collected in the gases flowing out of active fissures is quite different

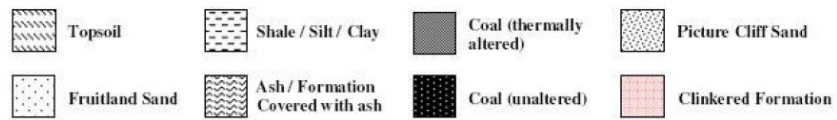
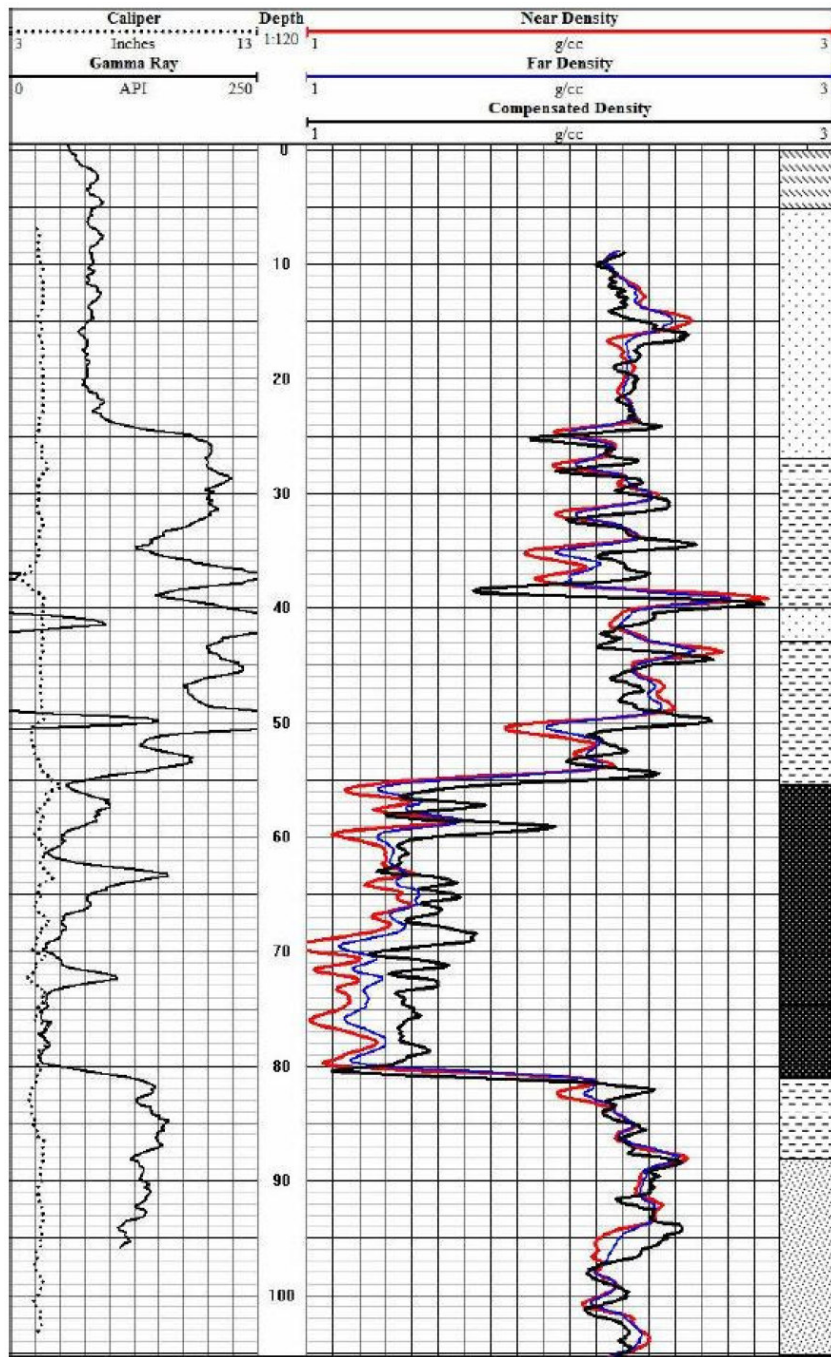


Figure 3. Log data and stratigraphic interpretation for hole 3.

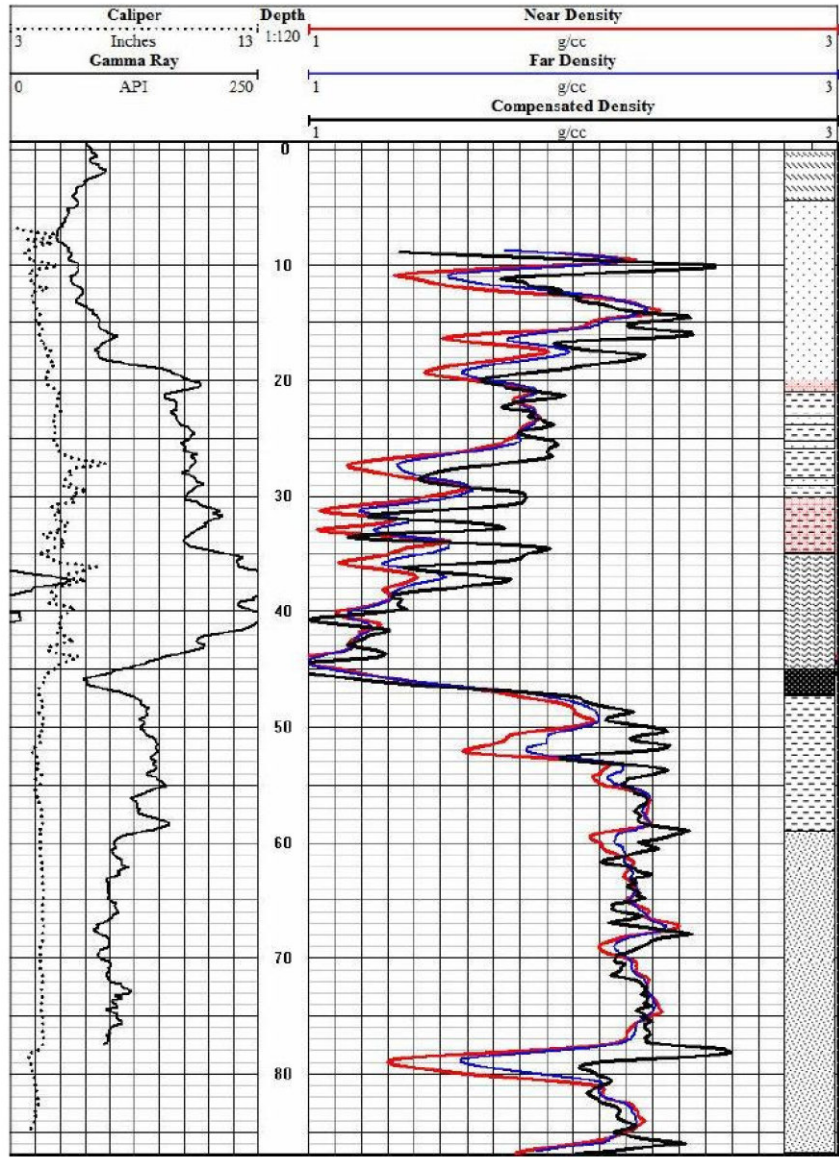


Figure 4. Log data and stratigraphic interpretation for hole 4.

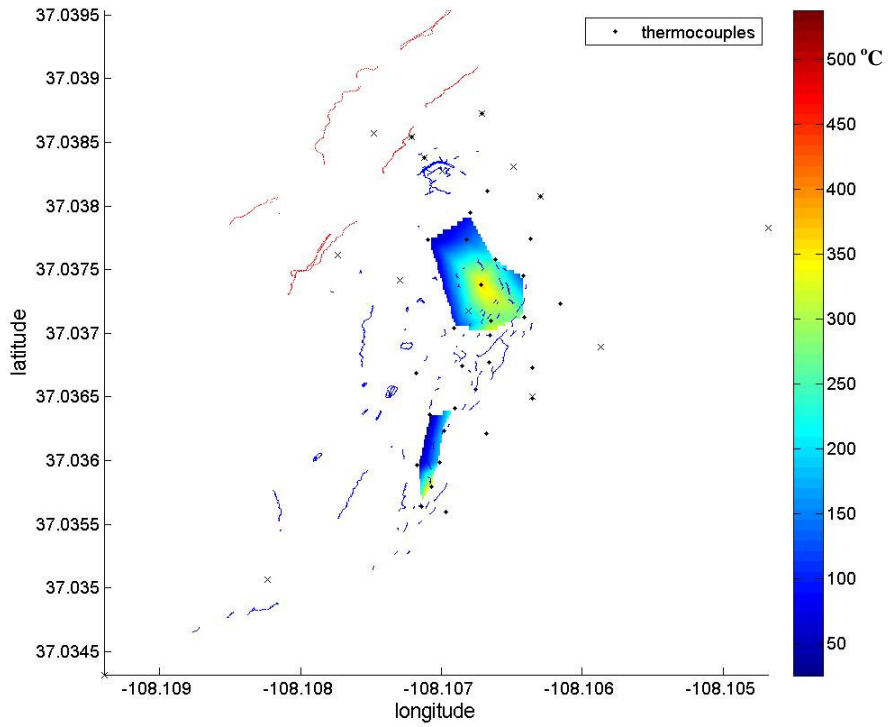


Figure 5. Subsurface temperatures measured in 2001.

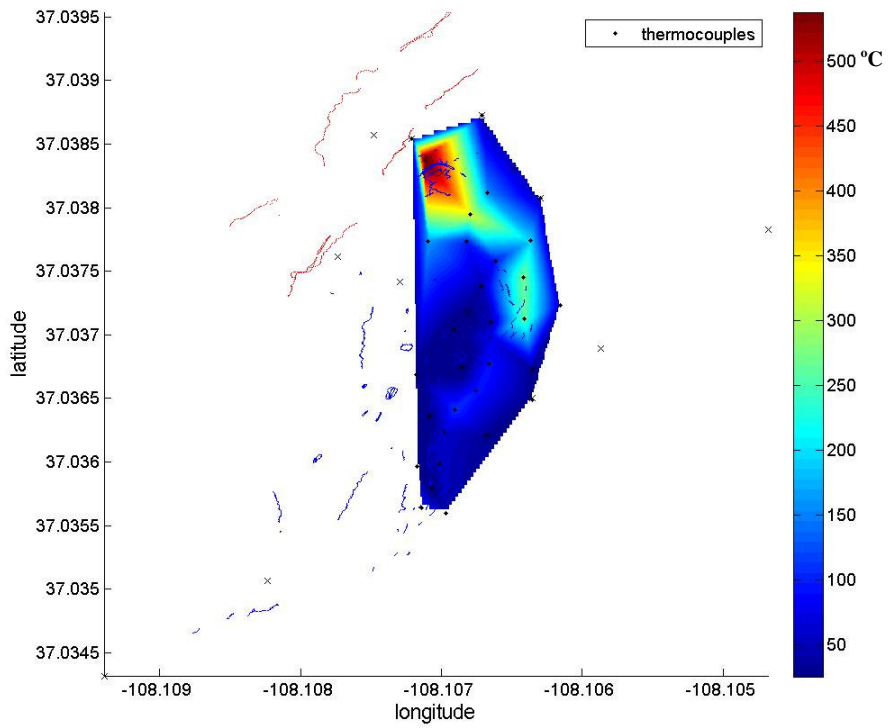


Figure 6. Subsurface temperatures measured in 2007.

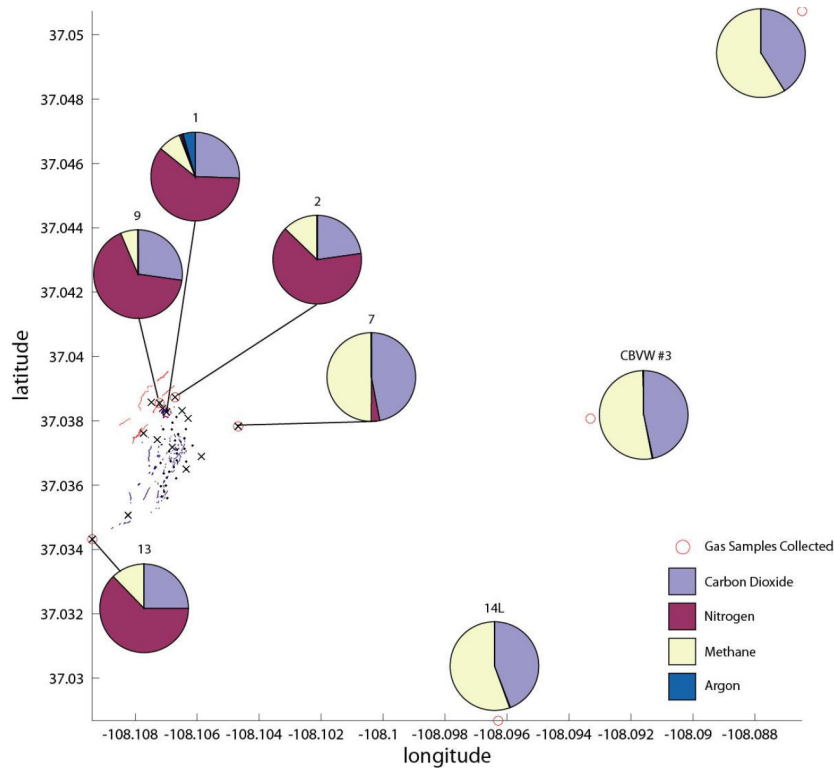


Figure 7. Gas composition data for locations near the coal fire and well away from the combustion zone.

from that of gases resident in the coal. That difference suggests that it may be possible to distinguish in future gas samples between CO₂ and CH₄ flowing from the unburned coal and CO₂ and CH₄ created in the partial oxidation reactions in the combustion zone itself.

Table 1. Isotope signatures of gas from the coal bed and gas flowing from drill hole 1

| | C ¹³ Isotope (CO ₂) | C ¹³ Isotope (CH ₄) | Deuterium (CH ₄) | Specific Gravity | BTU (CH ₄) |
|---------|--|--|------------------------------|------------------|------------------------|
| Well 1 | -10.12 | -38.73 | -187 | 1.043 | 101 |
| 14L | 14.57 | -46.17 | -228.7 | 0.982 | 564 |
| CBVW #3 | 14.34 | -45.94 | -227.9 | 1.006 | 539 |
| SS2 | 13.84 | -45.95 | -233.9 | 0.951 | 598 |

Geomechanics of Fissure Formation

The evidence obtained to date suggests that fissures play a very important role in the coal fire. They can provide the inlet for air, and they provide an exit for the hot gases that are created by the combustion reactions. Those fissures are, in effect, the chimney through which a density-driven flow feeds air to sustain the combustion reactions. To investigate the impact of subsidence on fissure formation, data from all the drill holes were combined to estimate the thickness and depth of the coal in the combustion area as well as to estimate the thickness of the burned coal. Figure 8 reports the results. The estimates show subsidence of 1.5-2.7 m. That length scale is consistent with subsidence observed in a nearby coal bed that shows evidence of an ancient fire that has now been exposed by erosion. Figure 9 shows two images of that outcrop. Figure 9a shows that

clinkered rock appears above a zone where the coal is missing. It also shows that the subsidence is about 2 m. Figure 9b shows a different view of the same outcrop with a surface fissure above the zone of subsidence.

The effect of subsurface subsidence was then modeled using a Boundary Element Method (BEM) formulation called a displacement discontinuity in an elastic half plane. This problem formulation is an adaptation of the elastic infinite plane displacement discontinuity method, where the finite surface is modeled using the principle of superposition (Crouch and Starfield, 1983). The problem of constant displacement discontinuity is formulated with the condition that the displacements are continuous everywhere except over the line segment where either a vertical (normal) or a horizontal (shearing) displacement is defined. The stress distribution solution is a function of the displacement location, magnitude, the shear modulus, Poisson's ratio, and the tilt of the displacement segment.

Figure 10 shows a schematic of a simplified subsidence calculation. Figure 11 shows the corresponding calculated displacements. The displacement patterns are roughly consistent with the observations made in the field. These simple calculations suggest that fissure formation is driven primarily by the removal of coal by combustion, which results in compaction and subsidence, which in turn creates stresses at the surface that cause opening mode fissures. In contrast, heating of the rocks above the combustion zone causes expansion of the rock, which creates compression and would therefore not lead to fissure formation.

Approximate Location of the Combustion Zone

The combination of observations gathered to date is sufficient to allow estimation of the locations of burned coal and the current location of the combustion front. Figure 12 shows that estimate. The boundary of the combustion zone is necessarily approximate. Drill holes that showed ash returns give a direct indication of past combustion, and high temperatures at surface fissures and at subsurface thermocouple locations indicate combustion nearby. Drill holes that show no evidence of combustion indicate that the boundary of the combustion zone lies somewhere between the current hot zone and the unaffected region, but the exact location of the boundary is not known, of course. The red line in Figure 12 shows the estimated maximum extent of the burn zone, and the yellow line shows areas for which there is some evidence that the fire may started have there. That observation is based on the existence of ash on the surface near where the coal would have outcropped and clinkered sandstones in the same areas.

It may be possible to use shallow seismic observations to delineate the area where coal has been burned in the past. There should be a significant contrast in seismic velocity between burned and unburned regions, for example. The possible use of shallow seismic measurements to delineate the combustion region is now being explored.

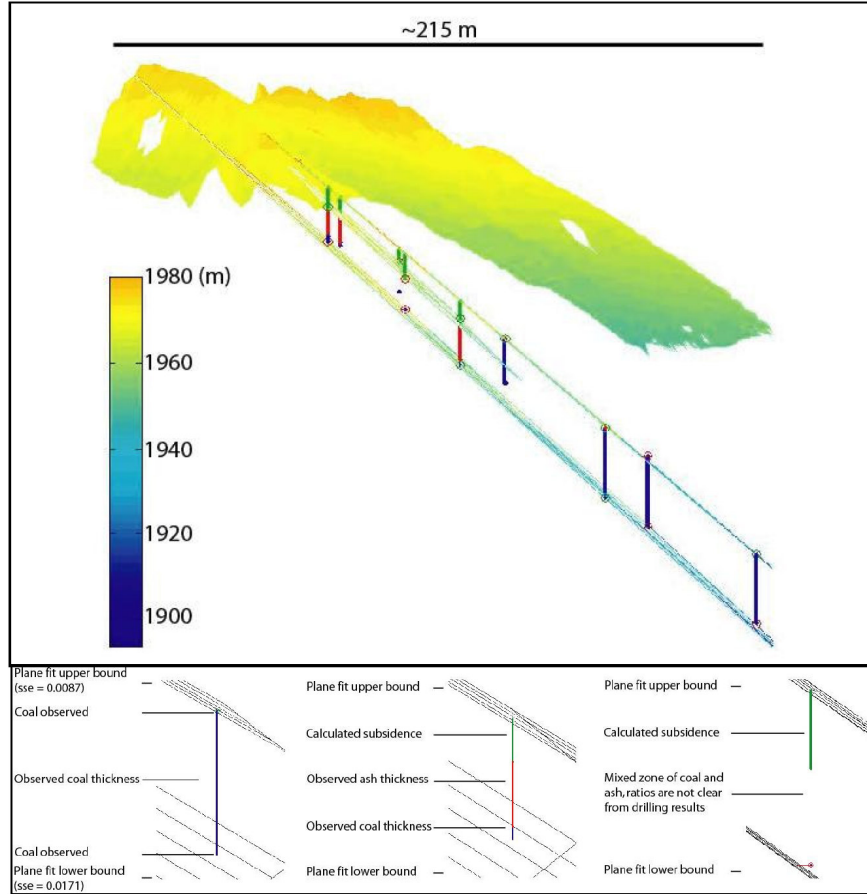


Figure 8. A combined surface and subsurface model depicting the surface contour and the subsurface coal seams. The middle plane in between the theoretical top and the bottom coal planes indicate the depth at which the coal seam has subsided to due to compaction.



Figure 9. (a) 2 m tall person standing below a subsided region, (b) a 1.5 m tall person standing below a subsided region and a surface fissure ~16 m above.

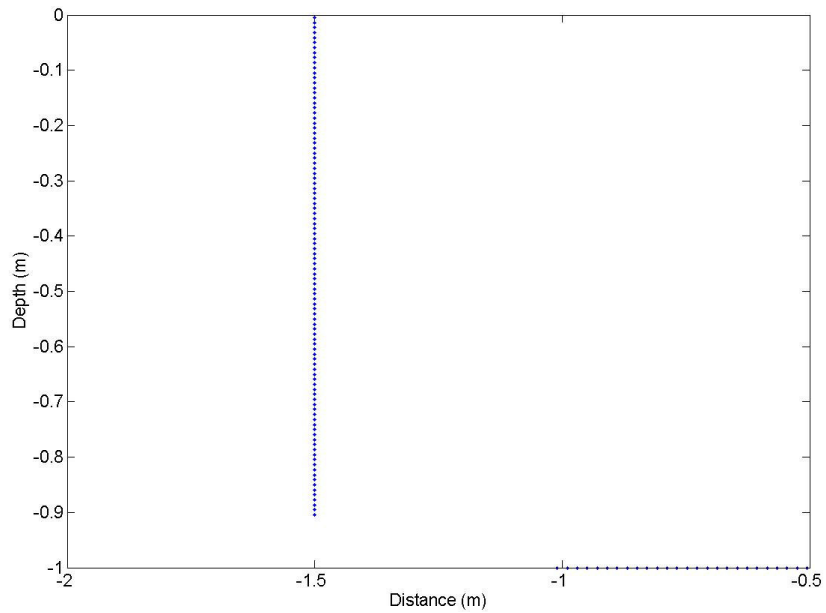


Figure 10. A Schematic of a simplified subsidence calculation. A constant displacement boundary condition is defined at the elements along the horizontal layer. The effect of the collapse on the vertical fracture is calculated.

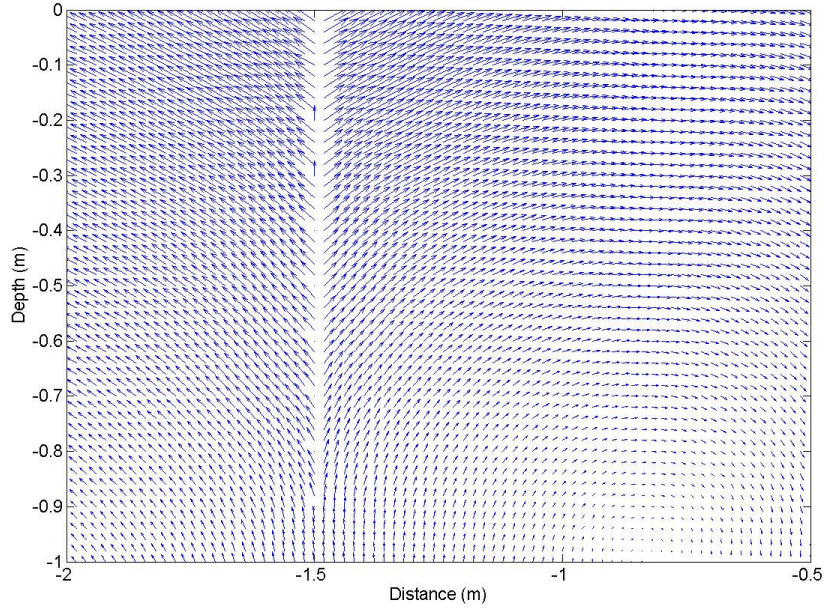


Figure 11. Calculated displacement trajectories that result from a collapse initiated on the horizontal layer.

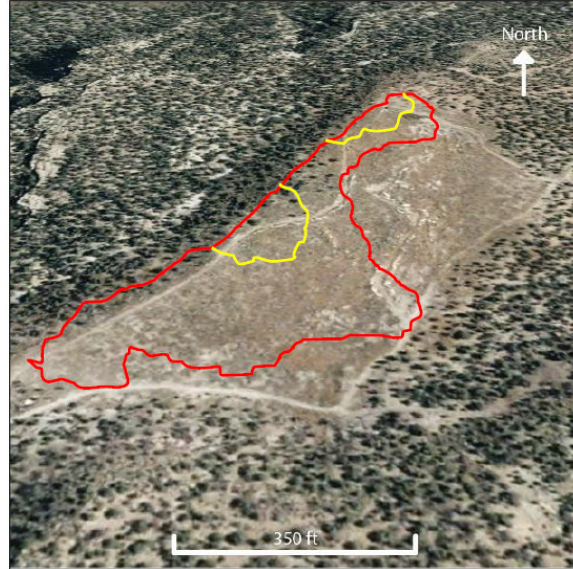


Figure 12. Estimated coal fire boundary. The red line is an estimate of the maximum extent of combustion, and the yellow line indicates possible areas where the fire started.

Additional Observations and Modeling Work

The field observations and interpretations assembled so far will be the basis for additional work to:

- refine understanding of the mechanics of fissure formation by making the boundary conditions for the calculation more realistic (a semi-infinite domain instead of an infinite one, for example)
- delineate more accurately where combustion is taking place now by a combination of surface temperature observations and possible seismic imaging of the burned zone,
- estimate the overall rate of coal combustion from estimates of gas flow rates for passages of dimensions constrained by field observations and fissure calculations,
- estimate the pressure gradients that drive flow of O_2 to the combustion zone and the release of hot gases from it using a combustion simulator, and
- determine whether it might be possible to disrupt those pressure gradients by fluid injection in a way that would exclude O_2 from the combustion zone and extinguish the fire.

When completed, this description of the anatomy and mechanics of a subsurface coalbed fire will be the most complete available so far.

Acknowledgement

We are very much indebted to Bill Flint and the Southern Ute Indian Tribe for allowing us to study in detail the field site on tribal land and for providing extensive support for the field work. We acknowledge with gratitude their many contributions to this work.

References

- Brown, K., "Subterranean Coal Fires Spark Disaster," *Science* 299, 1177, 2003.
- Cassells, C.J.S. and van Genderen, J.L., 1995. Thermal modeling of underground coal fires in northern China: Remote Sensing in Action. In: *Proceedings of the 21st Annual Conference of the Remote Sensing Society*, University of Southampton, England, pp. 544–551.
- Crouch, S.L. and Starfield, A.M., *Boundary Element Methods in Solid Mechanics* (London: George Allen & Unwin Ltd., 1983).
- Dai, S.F., Ren, D.Y., Tang, Y., Shao, L., and Li, S., 2002. Distribution, isotopic variation, and origin of sulfur in coals in Wuda Coalfield, Inner Mongolia, China. *Int. J. Coal Geology* 57: 237-250.
- DeKok, D., 1986, *Unseen danger*: University of Pennsylvania Press, p. 299.
- Fassett, J.E., 2000. Geology and coal resources of the upper cretaceous Fruitland formation, San Juan Basin, New Mexico and Colorado, Chapter Q of Geologic Assessment of Coal in the Colorado Plateau: Arizona, Colorado, New Mexico, and Utah, USGS Professional Paper 1625-B.
- Kunzer, C., Voigt, S., and Morth, D., 2005. Investigating land cover changes in two Chinese coal mining environment using partial mixing. *Gottinger Geographische Abhandlungen* 113.
- Rosema, A., Genderen, J.L. van, Schalke, H.J.W.G., 1993. Environmental monitoring of coal fires in north China. Project Identification Mission Report, BCRS 93-29, ISBN 90 5411 1054.
- Stracher, G.B. and Taylor, T.P., "Coal fires burning around the world: thermodynamic recipe for environmental catastrophe," *Int. J. Coal Geology*, 2004.
- Zhang, X. and Kroonenberg, S.B., 1996. Pleistocene coal fires in Xinjiang, northwest China. *Abstracts of the 30th International Geologic Congress, Beijing, China (August 4–14)* 1, p. 457. "Reviews in Engineering Geology, XVIII" edited by Glenn Stracher, entitled *Geology of Coal Fires: Case Studies from Around the World*.

Subsurface Monitoring of CO₂ Sequestration in Coal

Dynamic imaging provides an effective way to integrate previous time-lapse data with current data in order to estimate a current model. We present two methods useful for continuous dynamic reservoir and subsurface monitoring. The first method is a stochastic method for the inversion of geophysical data. It uses the ensemble Kalman filter (EnKF) that we demonstrate using time-lapse surface seismic data. We use reflection waveform and travelttime data plus sonic log information as input to the EnKF inversion. Unlike conventional seismic methods that give relative impedance, the EnKF inversion yields absolute seismic velocity. The second method is a specific dynamic imaging algorithm we call DynaSIRT. DynaSIRT integrates data from previous surveys in an efficient way, without the reprocessing older data. It preserves state variables that store the temporally damped effective illumination of previous surveys and timestamps to track parameter updates. We show results of DynaSIRT applied to synthetic time-lapse diffraction tomography data, where it provides a clear detection of a CO₂ leak even for sparse survey geometry. Lastly, we introduce the method of data evolution to supplement sparse data surveys for continuous monitoring. Data evolution may be used with any dynamic imaging stream to supplement sparse data recordings with predicted data based on spatio-temporal interpolation. And finally, we report herein a feasibility study for the use controlled-source electromagnetics (CSEM) for monitoring geological CO₂ storage in coal. We conducted the CSEM study in both the frequency domain and time domain. In order to test various monitoring methods and strategies, we used relatively realistic time-lapse seismic and electrical models that were constructed from flow simulation and rock physics.

Introduction

Seismic and electromagnetic methods are developed for monitoring geological CO₂ storage. CO₂ sequestration provides a possible solution for reducing green gas emissions to the atmosphere. For safety and operational reasons, we need to monitor the containment of the CO₂ in the subsurface. This report summarizes a continuation of last year's research on subsurface monitoring. In the 2007 report, we reviewed the seismic properties of coalbeds, discussed the concept of continuous monitoring with sparse data, and proposed a monitoring method using feature-enhanced adaptive meshes with spatio-temporal regularization.

In this year's report, we focus on a realistic full seismic simulation of dynamic imaging using surface reflection data. By "realistic", we mean (1) a flow model built from real field parameters for coal beds; (2) a sequence of time-lapse models simulated for CO₂ storage in dual porosity coal model with adsorption in coal; (3) a sequence of seismic models generated from rock physics; (4) full waveform seismic data generated with the finite difference method for surface reflection surveys; (5) Inversion of the simulated data using the robust EnKF statistical algorithm and DynaSIRT. This full scale simulation provides a reality check before field data experiments can be run. We also present a data evolution approach that is an important step towards continuous spatio-temporal tomography from sparse time-datasets.

In addition to seismic monitoring techniques, we also investigated the controlled-source electromagnetic (CSEM) method. Coalbeds are relatively shallow; therefore, the CSEM technique seems promising for monitoring of CO₂ sequestration in coalbeds. Since the CSEM method is preferentially sensitive to thin electrical resistors, we expect this method to be suitable for CO₂ leakage detection. We have carried out two numerical simulations in the frequency domain and the time domain to test the responses to the leakage models. Various survey configurations are examined for sensitivity tests.

The Application of Ensemble Kalman Filter for Inversion of Waveform and Traveltime Seismic Data

Introduction

Subsurface monitoring is a dynamic process. Seismic monitoring data observed at the surface change with time and consist of a series of time-lapse datasets. We want to integrate the temporal information captured by time-lapse datasets into the spatial seismic inversion (or imaging) method and develop the spatio-temporal seismic inversion for the monitoring. The Kalman filter is a classical method for integrating temporal and spatial information. The standard Kalman, however, has problems with a large number of model parameters as we have in seismic inversion. To overcome this problem, Evensen introduced the ensemble Kalman filter (EnKF). A complete introduction to EnKF can be found in Evensen (2007).

EnKF is a stochastic version of the Kalman filter. EnKF can be used for linear and non-linear stochastic inversion. It can also integrate different types of data in the inversion. Taking advantage of these features, we combine waveform data and travel time data for seismic inversion. The waveform inversion in our study is non-linear. The use of travel time data improves the estimation of the absolute seismic velocity.

The purpose of inversion is to recover the subsurface seismic properties e.g., acoustic impedance and velocity. For example, Oldenburg et al. (1983) discussed a deterministic approach for impedance inversion; Hass and Dubrule (1994) introduced a stochastic impedance inversion; Cao et al. (1989) presented an inversion method to estimate the background velocity and impedance simultaneously. Francis (2005) and Sancevero et al. (2005) compared deterministic and stochastic impedance inversion using examples. In general, stochastic seismic inversion has higher vertical resolution than deterministic inversion.

We first introduce the EnKF method and then use surface seismic data simulated for CO₂ monitoring in coal to demonstrate the monitoring method. The method can also be used for general stationary reservoir characterization.

Model

Consider the seismic signal \mathbf{d} recorded at surface as a function of subsurface model vector \mathbf{m} . In this seismic experiment, \mathbf{d} is normal incidence reflection data obtained after all necessary signal processing, and \mathbf{m} is the 1-D seismic velocity model directly below

the receiver. Data \mathbf{d} and model \mathbf{m} are related through an observation matrix \mathbf{G} for the linear case:

$$\mathbf{d} = \mathbf{G}\mathbf{m}. \quad (1)$$

A more general observation function g includes non-linear cases:

$$\mathbf{d} = g(\mathbf{m}). \quad (2)$$

We want to estimate model \mathbf{m} from observed data \mathbf{d} by a stochastic inversion procedure implemented with the ensemble Kalman filter.

We follow the derivation in Evensen (2003) and apply the general EnFK theory to our monitoring problem, i.e., joint inversion using both waveform and travelttime data. In our case, \mathbf{m} is an n -dimensional model vector composed with discretized 1-D velocity below the receiver; \mathbf{d} is an m -dimensional data vector having m_1 waveform data points and m_2 travelttime data points, where $m=m_1+m_2$. A proper scaling factor is needed to normalize the two types of data.

Assume model \mathbf{m} has a Gaussian probability distribution with mean \mathbf{m}_0 and covariance \mathbf{C} , and data \mathbf{d} also has a Gaussian probability distribution with mean \mathbf{d}_0 and covariance \mathbf{R} . We create a model ensemble

$$\mathbf{M} = [\mathbf{m}_1, \dots, \mathbf{m}_N] \quad (3)$$

that has the mean \mathbf{m}_0 and the covariance \mathbf{C} , and a data ensemble

$$\mathbf{D} = [\mathbf{d}_1, \dots, \mathbf{d}_N] \quad (4)$$

that has the mean \mathbf{d}_0 and the covariance \mathbf{R} . Here, \mathbf{m}_i and \mathbf{d}_i are ensemble members; N is the ensemble size that should be large enough to provide a good approximation to the probability distribution for the model and the data. The EnKF gives the statistical solution for a linear problem shown in equation (1):

$$\hat{\mathbf{M}} = \mathbf{M} + \mathbf{K}(\mathbf{D} - \mathbf{G}\mathbf{M}), \quad (5)$$

where

$$\mathbf{K} = \mathbf{C}\mathbf{G}^T(\mathbf{G}\mathbf{C}\mathbf{G}^T + \mathbf{R})^{-1} \quad (6)$$

is called the Kalman gain. The EnKF solution for a non-linear version equation (2) will be discussed in next section. The matrix $\hat{\mathbf{M}}$ is an $n \times N$ matrix; each column represents a realization from the posterior probability distribution. The average of all columns (or realizations) forms the solution for the model estimation. In a time-lapse inversion problem, new data are coming in continuously, and the model can be continuously updated by repeating the procedure above, equations (3)-(5), using the estimated model obtained in current step as the initial model for next time step.

Implementation

We start with an initial model \mathbf{m}_0 created from prior knowledge, e.g., sonic logs and their interpolations, or just a constant model in the worst case. Then we construct the model ensemble in equation (3) as

$$\mathbf{m}_i = \mathbf{m}_0 + \varepsilon_i,$$

where ε_i is a n -dimensional random vector with Gaussian statistics. Convolution is used as the observation function for waveform data modeling, that is, we calculate reflection coefficients from 1-D velocity and convolve the reflection profile with a wavelet extracted from the normal incidence seismogram and a sonic log. The observation function in this study is not a linear function, and we cannot directly use equation (6), because it is difficult to find an observation matrix \mathbf{G} for this convolution modeling operation. Instead we have to use a matrix-free implementation (Mandel, 2006) for this inversion.

The model covariance \mathbf{C} in equation (6) can be approximated by the ensemble covariance as

$$\mathbf{C} = \mathbf{A}\mathbf{A}^T / (N - 1), \quad (7)$$

where

$$\mathbf{A} = \mathbf{M} - E(\mathbf{M}) = \mathbf{M} - \frac{1}{N} \sum_{i=1}^N \mathbf{m}_i.$$

Then model update equation (5) can be performed with

$$\hat{\mathbf{M}} = \mathbf{M} + \frac{1}{N - 1} \mathbf{A}(\mathbf{G}\mathbf{A})^T \mathbf{P}^{-1} [\mathbf{D} - g(\mathbf{M})], \quad (8)$$

where

$$\mathbf{P} = \frac{1}{N - 1} \mathbf{G}\mathbf{A}(\mathbf{G}\mathbf{A})^T + \mathbf{R}, \quad (9)$$

and the i^{th} column of matrix $\mathbf{G}\mathbf{A}$ can be obtained from

$$[\mathbf{G}\mathbf{A}]_i = g(\mathbf{m}_i) - \frac{1}{N} \sum_{j=1}^N g(\mathbf{m}_j). \quad (10)$$

For the data ensemble \mathbf{D} , we perturb the observed data \mathbf{d} and have

$$\mathbf{d}_i = \mathbf{d} + \gamma_i.$$

Here, γ_i is an m -dimensional random vector from Gaussian statistics. The data covariance \mathbf{R} required in equation (9) can be obtained from the ensemble covariance

$$\mathbf{R} = \gamma\gamma^T / (N - 1).$$

We next apply the procedure described above to a synthetic example.

An Example of Time-lapse Seismic Monitoring

This is an integrated simulation study for seismic monitoring of CO₂ sequestration in coalbeds. The primary goal of this simulation is to create a series of relatively realistic CO₂ storage models and the corresponding surface reflection seismic data for monitoring tests.

Time-lapse Models

We first build a 2-D reservoir flow model according to the geology and flow parameters of unmineable coalbeds in the Powder River Basin. Over a period of 10 years, 175 time-lapse models are generated using the flow simulator GEM. Various cases, e.g., CO₂ storage with or without leakage, are simulated. In the coalbed, matrix porosity equals 5%, cleat porosity equals 1-5%, matrix permeability equals 0.5md and cleat permeability equals 100md.

Next, we convert the flow simulation results to time-lapse *P*-wave velocity models with the help of a rock physics model. Figure 1 shows four velocity models at time =0, 3 months, 1 year, and 3 years. It can be seen that the *P*-wave velocity decreases due to the CO₂ saturation. The methods discussed in previous sections are applied to these models to test if we can track the CO₂ front using EnKF.

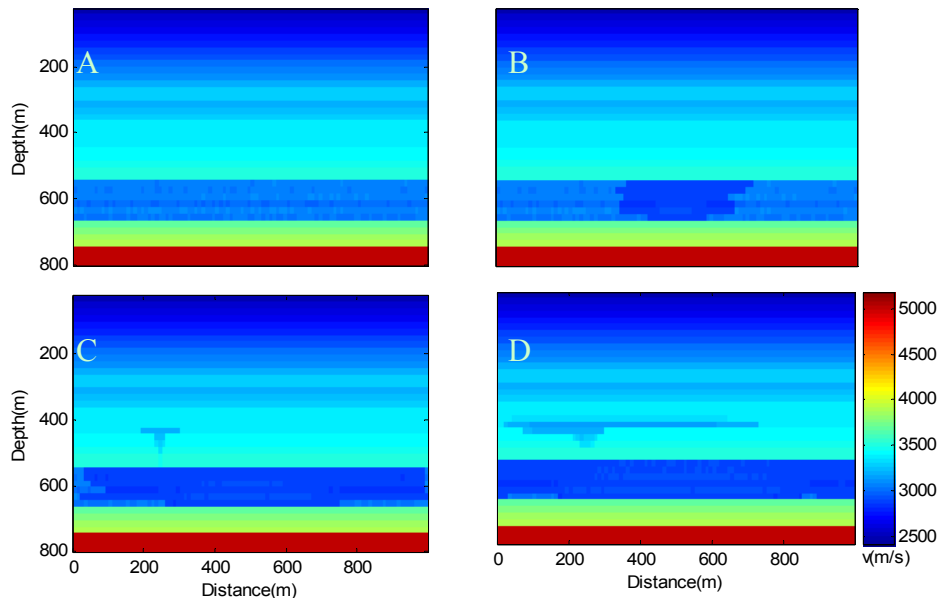


Figure 1: Four time-lapse *P*-wave velocity modes created based on CO₂ flow simulation in the coalbeds. A: time=0; B: time=3 months; C: time=1 year; D: time=3 years.

Seismic Data

A finite difference method is used to calculate the realistic seismic data (serves as observed data) for all 4 time-lapse models. Forty (40) shot gathers are calculated for each model. The source peak frequency is 50 Hz. Figure 2 gives a few samples of the shot gathers calculated using model D.

Prestack depth migration is then used to produce the depth image from these seismic data, where one of the resulting depth images is shown in Figure 3. The time image shown in Figure 4 is constructed from the zero-offset seismic traces. The reflection

waveform in the depth images plus the reflection picks from time and depth images are used for joint seismic inversion. Table 1 lists the reflectors picked from depth and time images (Figures 3 & 4) at a distance of 500 m, which provides the travetime data used for the joint inversion.

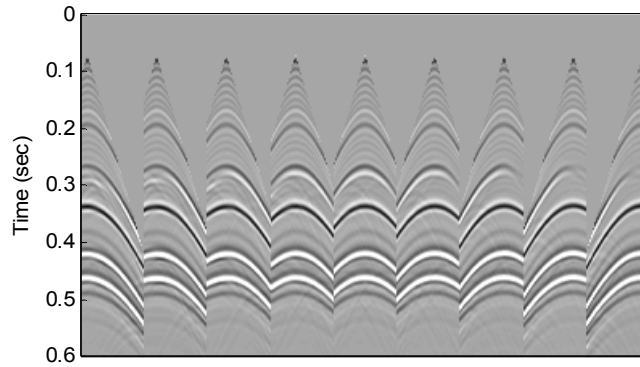


Figure 2: Sample shot gathers calculated using the finite difference seismic simulator.

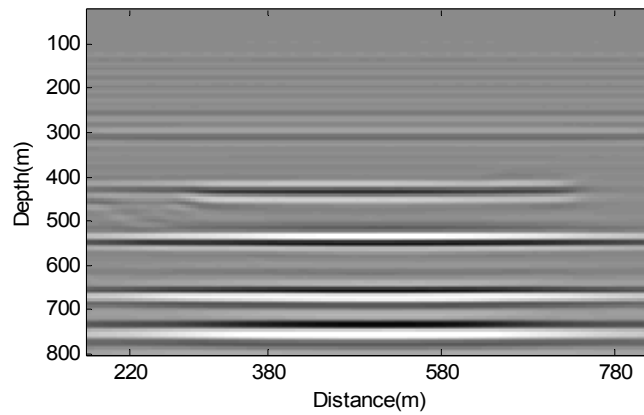


Figure 3: Prestack depth image of model D.

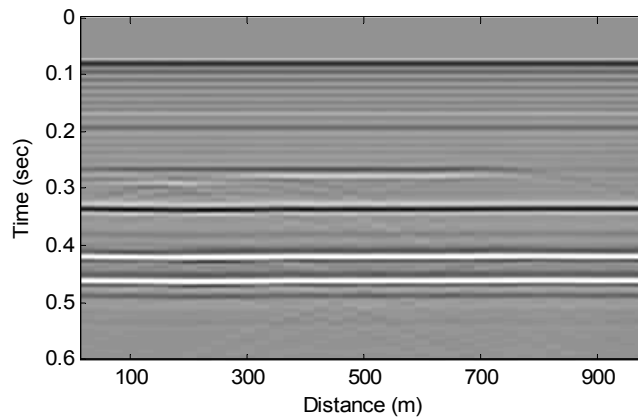


Figure 4: Time image of model D.

Table 1: Samples of traveltimes picks used for the inversion.

| Reflector | 1 | 2 | 3 | 4 | 5 |
|------------|--------|--------|--------|--------|--------|
| Depth (m) | 270 | 310 | 550 | 670 | 750 |
| Time (sec) | 0.1675 | 0.1918 | 0.3340 | 0.4173 | 0.4595 |

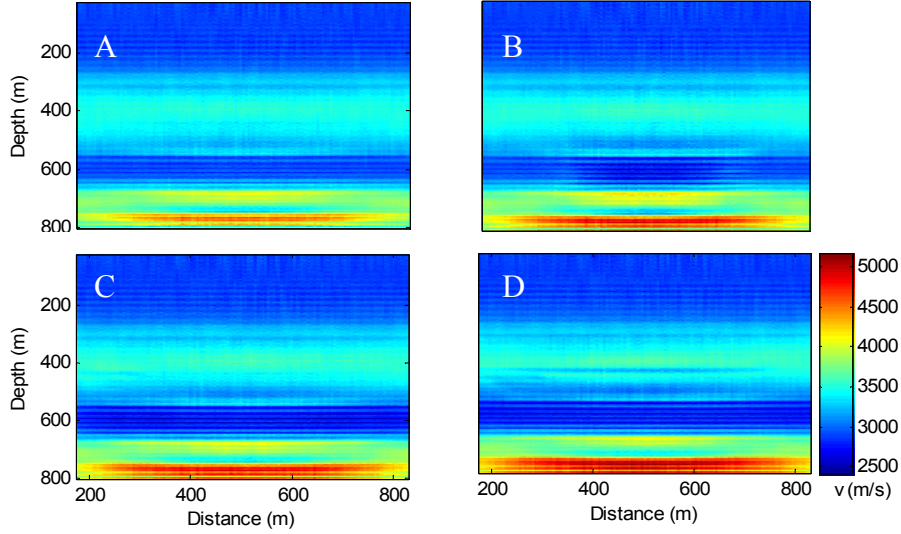


Figure 5: Time-lapse velocity models inverted using EnKF. Models A-D correspond to time=0, 3 months, 1 year, and 3 years, respectively.

Seismic Inversion with EnKF

Fast forward modeling tools are essential for EnKF inversion, because we must calculate $g(\mathbf{m}_i)$, equation (10), for each sample of the ensemble that usually has a size of hundreds of models. There are two types of forward modeling involved in the joint inversion. For waveform data, we assume a sonic log is available for source wavelet estimation and use the source wavelet for convolutional modeling. In this study, we simply use the true velocity profile for the wavelet estimation. Constant density is assumed for impedance calculation. The forward modeling in the inversion for traveltimes t is a summation down to a given reflector, i.e.,

$$t = 2 \sum_i 1/v_i,$$

where v_i is the 1-D velocity of i^{th} depth pixel.

Applying the procedure described in previous section to the synthesized “observed” seismic data, we obtain the inverted velocity models shown in Figure 5. In order to see the velocity changes more clearly, the velocity difference between models B-D and base model A are shown in Figure 6. A constant initial model is used in this test. It can be seen that the overall absolute velocity structure and the velocity drop due to CO₂ injection are

sufficiently recovered. Profiles in Figure 7 give a closeup comparison between the given model and the inverted model. Figure 8 compares the “observed” (or given data) and the data calculated with the inverted velocity. The given data and modeled data are virtually identical, though the given velocity model and the inverted velocity model exhibit some difference, especially the high frequency noise, which may be caused by the stochastic simulation procedure and the amplitude distortion in the depth imaging. True amplitude imaging will be very important for this seismic inversion.

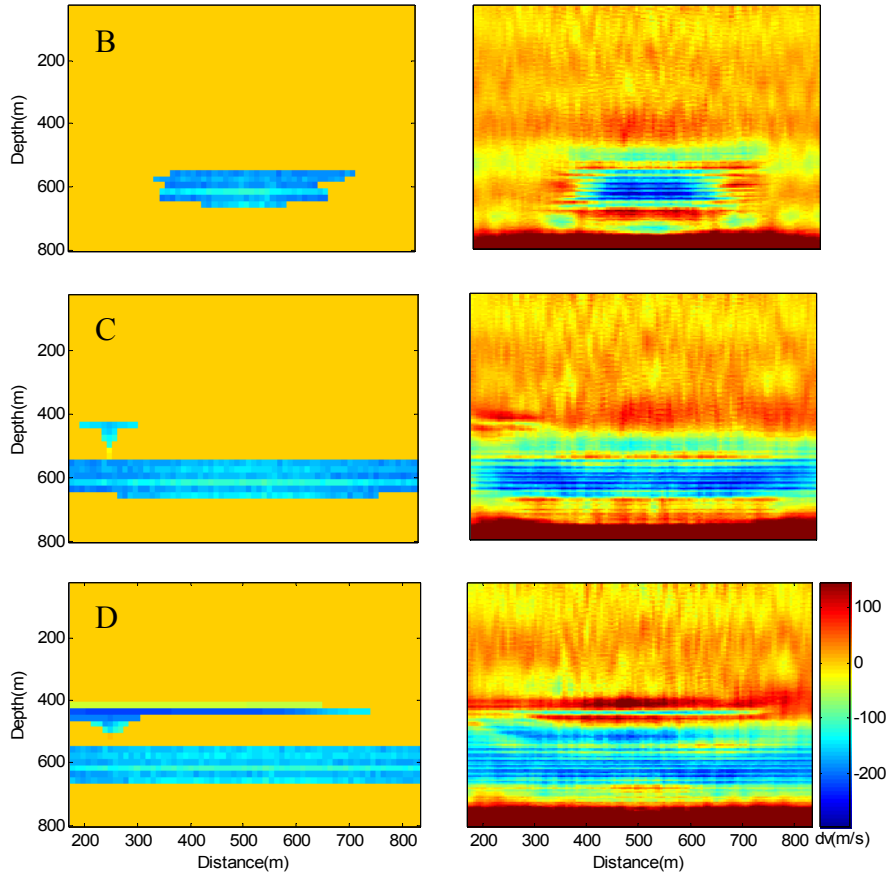


Figure 6: Velocity differences between time-lapse models B-D and base model A. Left: given models. Right: Inverted models.

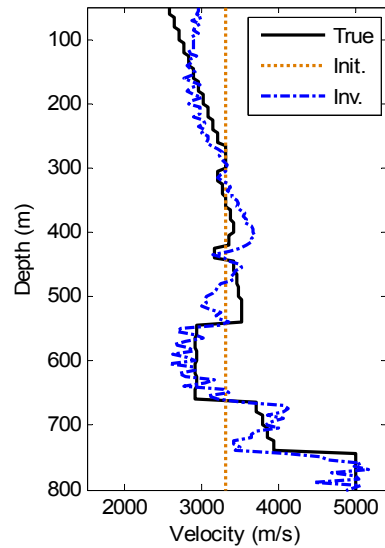


Figure 7: A comparison between true model (solid black line) and inverted model (Dashdot blue line) at distance=500 m. Dotted yellow line is the initial model.

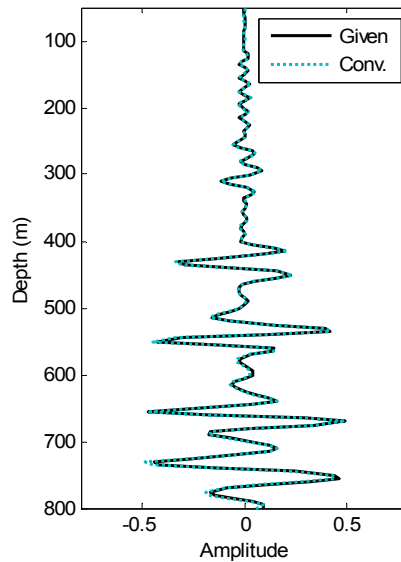


Figure 8: A comparison between “observed” data (solid line) and modeled data (dotted line). Solid line is sampled from distance=500m from the depth image and the dotted line is calculated from inverted velocity at the same location.

Conclusions

The ensemble Kalman filter provides a powerful tool for stochastic seismic inversion, especially for dynamic inversion in seismic monitoring. Integrating travetime data into the inversion makes the estimation of absolute velocity possible. Waveform data alone in the joint inversion gives the short wavelength (spatial) components of inverted velocity.

DynaSIRT: A Robust Dynamic Imaging Method for Time-lapse Monitoring

Dynamic Imaging

Dynamic imaging incorporates the temporal dimension into time-lapse seismic inversion. Instead of considering independent inversions for each time-lapse image, the temporal dynamics of the model are incorporated into inversion method, becoming a true spatio-temporal approach. This section describes a new algorithm for inversion of time-lapse seismic data named DynaSIRT. While conventional methods solve a system of equations independently for each survey for each snapshot in time, DynaSIRT incorporates information of previous surveys to estimate the current model without the reprocessing of previous data. Continuous or quasi-continuous monitoring present some special challenges for geophysical imaging. The amount of processing in case of joint inversion using data from older surveys or cross-equalization (Rickett and Lumley, 2001) can be excessively large and will grow in time. Practical implementation of dynamic imaging methods for seismic imaging must deal with memory and processing constraints. It can be done by incrementally solving the inversion problem and preserving solver state for later updates, keeping the problem tractable.

Regularization (Tikhonov and Arsenin, 1977) is usually applied to improve seismic imaging. Many conventional seismic imaging methods use spatial similarity along axes as additional information to perform inversion, applying spatial regularization (Santos, 2006). Analogously, similarities occur along time axes and can be used as well by means of temporal regularization (Ajo-Franklin et al., 2005). Dynamic imaging goes one step further beyond separated spatial and temporal regularization. It treats the evolution of the imaged area as a dynamic process, an integrated approach that intrinsically includes spatio-temporal dynamics on inversion method. Although medical imaging has successfully applied dynamic imaging methods, geophysics still widely uses static methods adapted for time-lapse imaging. This is due to the larger amount of data to be processed, the long time between geophysical surveys, and the larger number of parameters to be estimated from geophysical inversion methods.

DynaSIRT extends the static snapshot inversion method in order to incorporate temporal dynamic imaging. This method is efficient, processing equation by equation to incrementally update a previous model from new data. This incremental update is further explored for an additional advantage. The current state of the solver is saved for the next survey inversion, thus optimizing processing of sparse time-lapse data. Thus, DynaSIRT provides an efficient method for dynamic imaging, incorporating previous data into inversion without the burden caused by re-processing all the previous data. These features make DynaSIRT well suited for continuous monitoring of CO₂ injection.

DynaSIRT reduces computational effort by saving the solver state of last time-lapse inversion, avoiding increasing amounts of data to be processed along time. It can also provide snapshots of updated image during acquisition, due to its incremental way of processing and update.

Row-action Solvers

Row-action solvers compute an inversion problem solution iteratively, processing a linear system row by row, which means the updates are calculated equation by equation. These methods are the starting points for a practical implementation of dynamic imaging. A classic row-action method called ART (Algebraic Reconstruction Technique) computes parameter updates based on the difference between observed and computed data for each row (Peterson et al., 1985). The ART update equation for a linear system $\mathbf{d}=\mathbf{Gm}$ is given by

$$m_i^{(k+1)} = m_i^{(k)} + g_{il} \frac{\Delta d_i^{(k)}}{\sum_j g_{ij}^2}.$$

Here, d_i is the i -th data element; g_{ij} is a kernel matrix element, and m_i is the parameter element.

Artifacts may occur due to the row nature of ART since updates are computed separately for each row. Artifacts can be reduced by computing an average update from all equation updates. SIRT (Simultaneous Iterative Reconstruction Technique) averages the update using the expression (Stewart, 1992)

$$m_i^{(k+1)} = m_i^{(k)} + \frac{1}{N_l} \sum_{l=1}^n g_{il} \frac{\Delta d_i^{(k)}}{\sum_j g_{ij}^2}.$$

The iterative nature of these methods, dealing with each equation separately to update the model allows us to save the solver state and restart later from this saved state. This feature was implemented on DynaSIRT, avoiding reprocessing previous surveys data. Other row-action methods or methods that act on subsets of data may be used as well.

DynaSIRT

The continuous imaging/inversion approach must address three important questions:

- 1-How to preserve the influence of older survey equations on current model estimation?
- 2-How to balance influence between older and newer surveys equations?
- 3-How to avoid reprocessing older surveys equations?

DynaSIRT addresses these questions through the incorporation of three upgrades over original SIRT method:

- 1-Apply updates during computation, instead of later averaging and updating;
- 2-Apply temporal damping penalty effects for earlier surveys because the model changes with time (aging effects);
- 3-Save linear solver state for future surveys, thus avoiding reprocessing of older surveys equations.

The first upgrade was achieved by means of a moving average implementation. It yields a weighted expression that incorporates a single parameter update considering its influence over data when compared with previous surveys illumination N_l :

$$m^{(k+1)} = \left(\frac{N_l}{N_l + 1} \right) \Delta m^{(k-1)} + \left(\frac{1}{N_l + 1} \right) \Delta m^{(k)}.$$

The second upgrade was attained by exponential decay of older data over current model estimation. The third upgrade requires storing current model and timestamps for equations and parameters.

The DynaSIRT solver state is kept by four state variables: current estimated solution, number of equations that influence each parameter and timestamp arrays for equations and parameters. The aging factor α controls the decay of older survey equations influence, which is equivalent to the effective model illumination by previous surveys exponentially damped over time, i.e.

$$N_l^{(k+1)} = N_l^{(k)} e^{-\alpha(tse-tsp)},$$

where N_l , called effective illumination, is the number of previous equations that updated a certain parameter with index l , α is a temporal damping factor for aging, tse and tsp are the respective timestamps for equations and parameters. Placing the last two expressions into update equation yields the DynaSIRT update equation:

$$m^{(k+1)} = \left[\frac{N_l^{(k)} e^{-\alpha(tse-tsp)}}{N_l^{(k)} e^{-\alpha(tse-tsp)} + 1} \right] \sum_{i=1}^N g_{il} \frac{\Delta d_i^{(k+1)}}{\sum_j g_{ij}^2} + \left[\frac{1}{N_l^{(k)} e^{-\alpha(tse-tsp)} + 1} \right] \sum_{i=1}^N g_{il} \frac{\Delta d_i^{(k)}}{\sum_j g_{ij}^2}.$$

Model illumination N_l is damped, providing an effective number of equations that update each parameter over time, i.e., an effective illumination. Thus, the DynaSIRT update is based on survey acquisition timestamp and last parameter update timestamp, holding a trade-off between older and newer data in order to provide model estimation.

The most important factor controlling dynamic imaging in DynaSIRT is the aging factor (α) that controls how the relative influence of the older data with respect to newer data. It basically controls how the equivalent effective illumination of the model is updated according to how new the information timestamp is and how much illumination the new survey provides. This aging factor is related by analogy to the learning process of a system that incorporates new data but preserves older data to a degree. In seismic imaging, a very high factor would be equivalent to considering only the newest survey and to discard all previous ones ($\alpha \gg 0$), what is not usually wanted for when the current dataset is sparse. On the other hand, a very low aging factor would mean to keep all the older data but to resist against newer data. A very low aging factor would be equivalent to consider mostly the information from previous surveys but to minimize the influence of newer data, what is not usually wanted either ($\alpha \ll 0$).

Two particular cases are theoretically interesting. The first one happens when α is infinite, which would be analog to a system without memory. For this particular case, DynaSIRT becomes equivalent to SIRT applied only to the latest survey. Another particular case happens when α is zero, which means that the influence of older surveys is not damped and that all surveys are equally important, what is usually incorrect since the imaged area is usually changing over time.

Since the extremes are not desired, α should be chosen within a limited range. Lower α emphasizes older surveys influence. Higher α emphasizes newer surveys influence. The effects associated to intermediary values of α are somehow analog to control the regularization factor of temporal regularization in a very sophisticated and adaptive way. It means that conventional tools for regularization factor selection can be adapted for this purpose, such as L-curve (Hansen, 1992) or θ -curve (Santos and Bassrei, 2007).

Numerical Simulation

We applied DynaSIRT to a synthetic dataset generated with crosswell tomography surveys computed for 175 time-lapse 30×30 velocity models. The models show an expanding CO₂ leakage computed using the reservoir simulator (GEM) and monitored by a permanently emplaced crosswell acquisition system. The background velocity model (Figure 9 shows a coalbed between 550m and 650m of depth where the CO₂ is injected, causing a negative velocity contrast. All figures show distances in meters and velocities in m/s. Each time-lapse tomographic inversion was performed using diffraction tomography (Devaney, 1984) (Harris, 1987) (Wu and Toksöz, 1987). The discretization of the original continuous formulation leads to a linear system, which has to be inverted in order to estimate the velocity field (Rocha Filho, 1997) (Santos and Bassrei, 2007).

DynaSIRT was applied to estimate each time-lapse tomography solution, incrementally updating the estimated velocity field without reprocessing of previous surveys data. The error comparison between a conventional approach using SIRT and the proposed approach using DynaSIRT is shown on Figure 10 for the full survey (30 sources \times 15 receivers) and on Figure 11 for sparse partial survey (6 sources \times 15 receivers) along 175 time-lapse images for $\alpha=2$.

Good results were achieved and they show that inversion error is notably reduced when comparing DynaSIRT with SIRT for sparse partial surveys. Even when SIRT provides good results, the DynaSIRT method performs well, making SIRT an upper bound for its error.

The true velocity models for six time-lapse images equally spaced in time are shown on Figure 12 as absolute velocity contrast relatively to the background velocity field. The respective estimated models computed using DynaSIRT for sparse partial surveys are shown in the same way in Figure 13. Although this partial survey has only 20% of the data from the full survey, the DynaSIRT results still show good agreement with true models as expected from error comparison with SIRT.

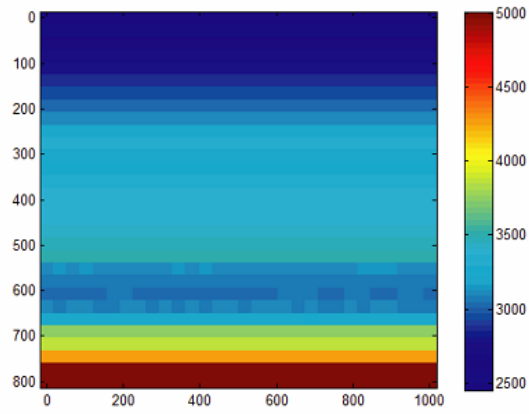


Figure 9: Background velocity field.

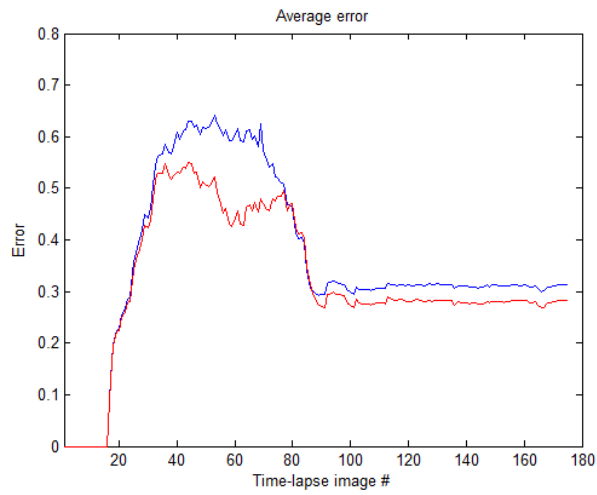


Figure 10: Error comparison along time for SIRT vs. DynaSIRT (full survey).

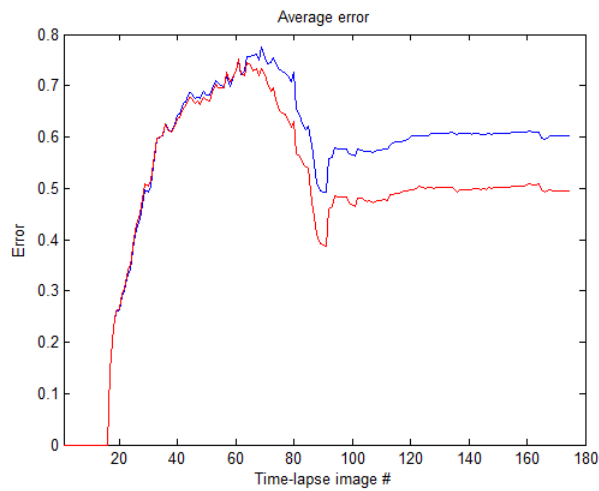


Figure 11: Error comparison along time for SIRT vs. DynaSIRT (partial survey).

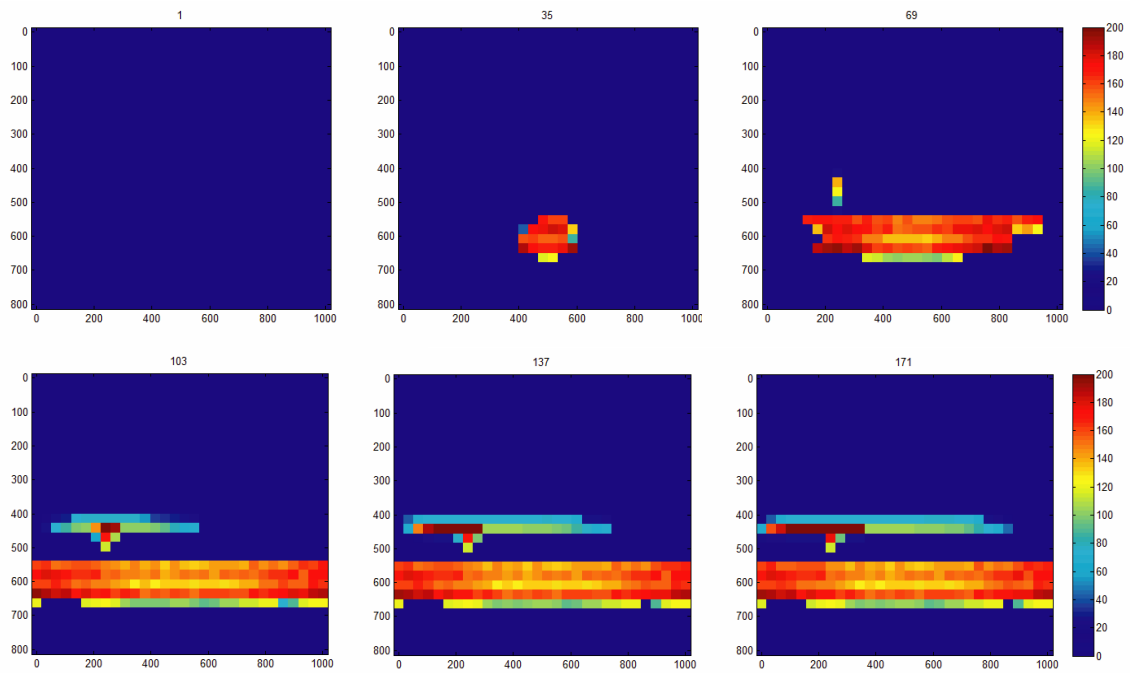


Figure 12: True model (CO₂ sequestration leakage modeling): velocity field contrast modulus. Time-lapse number shown on image top.

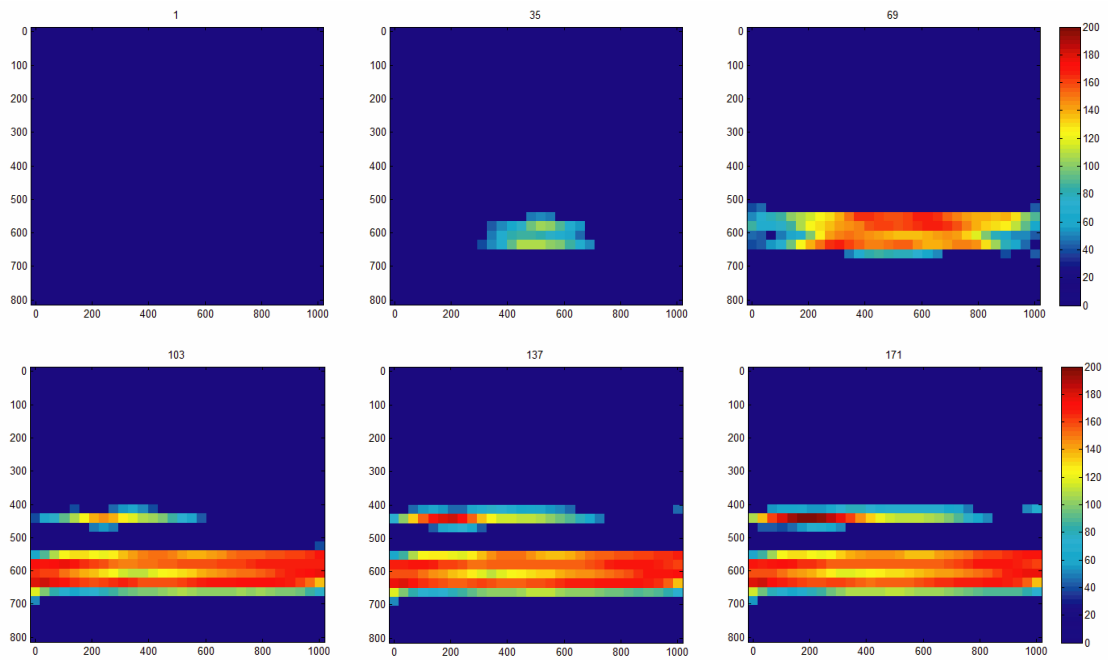


Figure13: Time-lapse tomographic inversion using DynaSIRT (partial survey): velocity field contrast modulus. Time-lapse number shown on image top.

Conclusions

We presented a dynamic imaging method called DynaSIRT that takes spatio-temporal aspects into account in time-lapse seismic imaging in order to continuously monitor CO₂ storage. The method was successfully applied to a synthetic dataset in order to perform time-lapse imaging for CO₂ sequestration monitoring. The current inversion state can be saved for newer updates, significantly improving computational efficiency. The next time-lapse inversion starts from the last solver state, including current estimated model, effective illumination and timestamps representing when model parameters were last updated and when data was acquired. Thus, DynaSIRT combines simplicity, robustness and efficiency for dynamic imaging. These features are very important for continuous monitoring, simplifying the design of permanent acquisition systems in order to acquire partial surveys, being well suited for CO₂ storage monitoring.

Data Evolution for Continuous Monitoring

We discussed the concept of data evolution for continuous monitoring in the 2007 annual report. We now give an example of data evolution using a statistical approach. We assume that the knowledge for the target being monitored increases as time-lapse monitoring experiments continue (e.g. Keeling & Whorf 1998; McKenna et al., 2001). It then follows that the amount of measured data required for continuous monitoring should reduce with time, with occasional acquisition of a complete dataset for calibration of the evolution process. Conventional techniques for time-lapse seismic monitoring cannot maintain spatial resolution in tomographic images while reducing data size, as demonstrated in Section 4 (Data Evolution and Model Evolution, GCEP Report 2007).

We propose to use acquired seismic data (sparse), which becomes sparser with time, along with the evolution technique to produce good, interpretable images of the subsurface through tomography. Since CO₂ sequestration and monitoring is a long-term effort, this approach will ensure a far more cost-efficient monitoring strategy than standard approaches.

Data integration can be statistically accomplished using spatio-temporal interpolation methods and/or the spatial covariance and temporal covariance of the data. A complete survey that is systematically designed to capture spatial changes in the data domain is used to determine the data spatial covariance structures. The temporal data covariance structures are obtained from simulated seismic data. To test the concept the seismic data are simulated from velocity models which are obtained from flow simulation. The product-sum covariance model (De Cesare et al., 2001) seems most relevant to the monitoring case. A simulation of the flow pattern of the injected CO₂ is carried out using prior knowledge of the geology as well as the interpretation of the baseline (before injection) velocity model in terms of rock properties. Then the spatial and temporal covariance information is used with the statistical simulation algorithm to evolve the sparse data into a full estimated dataset.

At every time-lapse step, the input to the statistical simulation algorithm is the previous measured data and the current measured data and the data covariance structures from the previously measured data and the simulated seismic data derived from the flow prediction.

The statistical simulation produces many realizations of the dataset. These will then be averaged to produce a point-wise mean dataset. In addition to estimating the point-wise mean, a distribution of the estimation uncertainty will also be produced. Finally the data uncertainty together with the time-lapse data will be used for subsurface imaging. We next use direct sequential simulation and crosswell seismic survey geometry to simulate how data evolution with direct sequential simulation method is implemented and used. In this example, only spatial covariance information is used. The tests on using both spatial covariance and temporal covariance are underway.

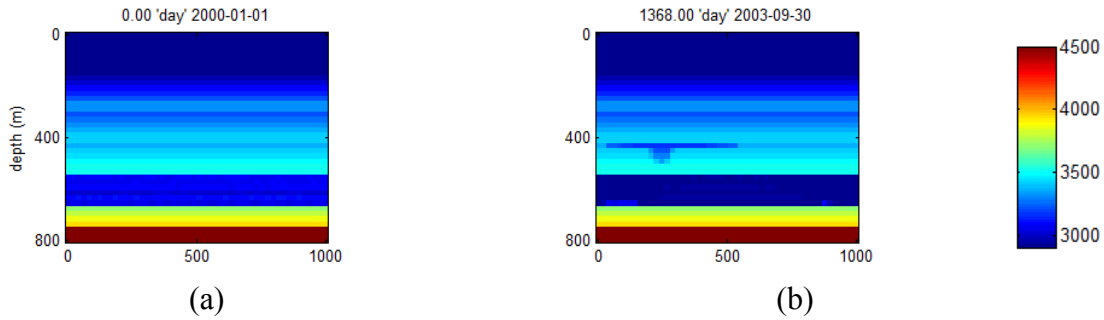


Figure 14: (a) True baseline (background) velocity model; (b) True time-lapse velocity model

Figure 14 shows 2 of 175 velocity models used in generating synthetic seismic traveltime data for testing the evolution method presented. The direct arrival traveltimes shown in Figure 15 were generated by assuming crosswell acquisition geometry with 100 shots and 100 receivers in wells on either sides of the model. The traveltime data can then be inverted using seismic tomography techniques.

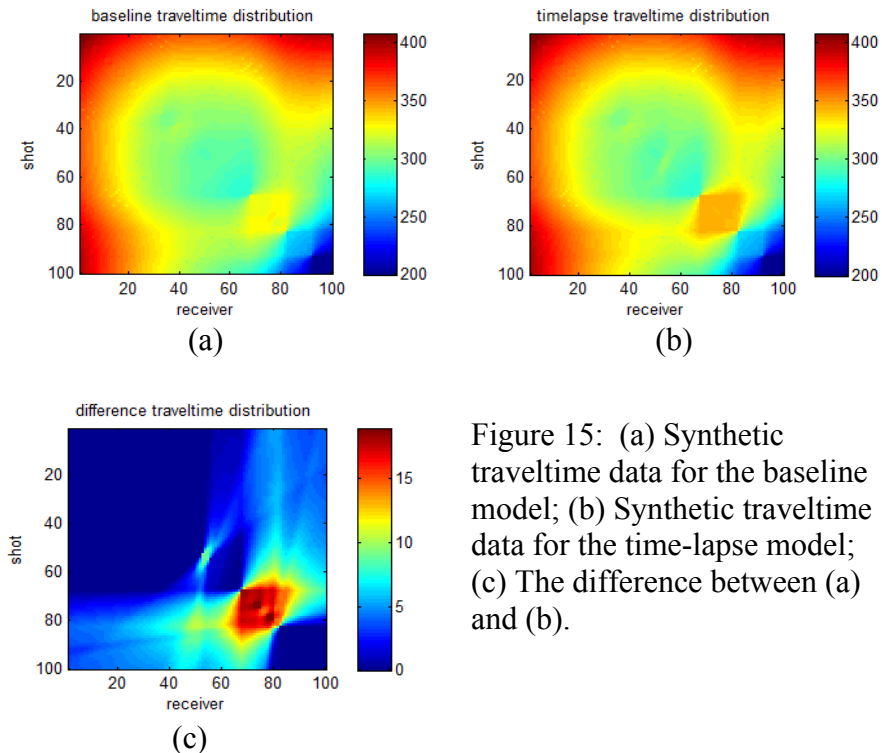


Figure 15: (a) Synthetic traveltime data for the baseline model; (b) Synthetic traveltime data for the time-lapse model; (c) The difference between (a) and (b).

Direct sequential simulation implementation

Consider a variable $\kappa(r)$ with a global cumulative distribution function $F_{\kappa}(z) = \text{prob}\{\kappa(r) < z\}$ and stationary spatiotemporal variogram, $\gamma(r)$, with which we intend to reproduce $\gamma(r)$ and $F_{\kappa}(z)$, direct sequential simulation will be implemented in the following way:

1. Select randomly, the location of a node r in a grid of nodes to be simulated
2. Get the neighborhood data, both original data, $\kappa(r_a)$, and simulated data, $\kappa(r_i)$
3. Calculate the conditional mean and conditional variance using simple kriging
4. Build a conditional cumulative distribution function (ccdf) at r with the moments obtained in step 3
5. Draw a value $\kappa(r_i)$ from the local ccdf
6. Return to step 1 until all nodes have been visited

Direct sequential simulation (dssim) was carried out on the data presented earlier, but decimated to about 10% (Figure 16b), using the variogram obtained from the complete data (from the full baseline dataset). Accurate estimates of the data are obtained by calculating the point-wise data average. Data uncertainties are obtained by calculating the point-wise data standard deviation. Selected realizations and the e-type (point-wise average) data are shown in Figure 17. Results compare reasonably well to the complete dataset.

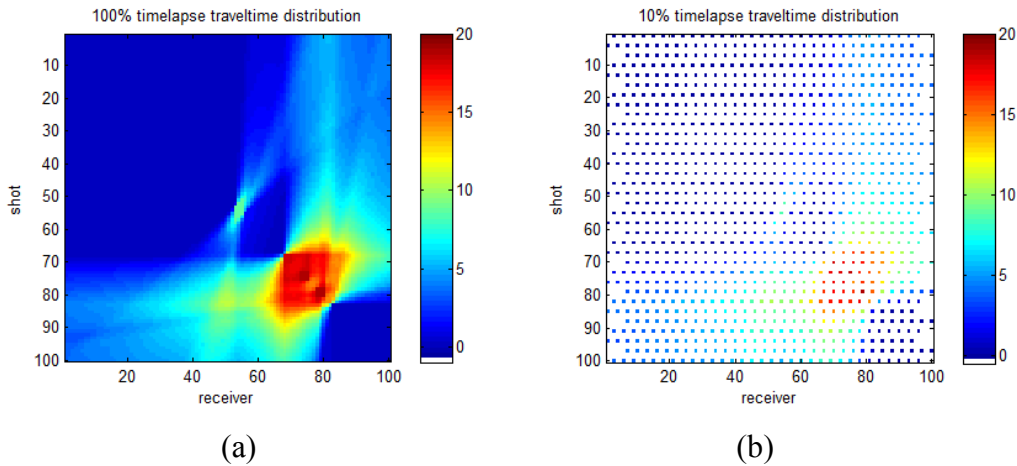


Figure 16: (a) Complete time-lapse difference dataset (same as Figure 15(c)); (b) Sparse 10% time-lapse difference dataset.

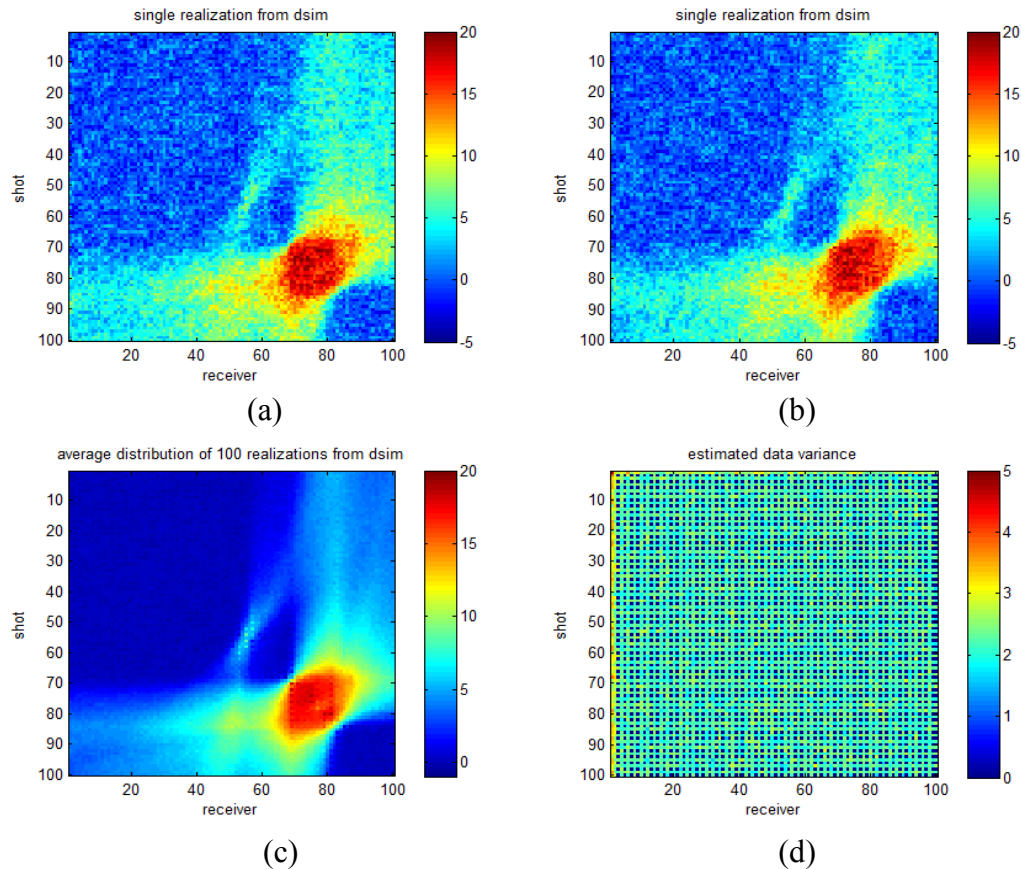


Figure 17: (a) and (b) are 2 realizations from 100 generated after running direct sequential simulation (dssim); (c) E-type (average) of all realizations obtained from running dssim on the dataset shown in Figure 16(b); (d) point-wise variance of all dssim realizations.

A Feasibility Study on the Controlled Source Electromagnetic Method for Monitoring of Geological CO₂ Sequestration

Introduction

The controlled-source electromagnetic (CSEM) method was first developed in academia more than 30 years ago to investigate the electrical conductivity structures of the deep ocean lithosphere and terrestrial basin (Strack, 1984 and Cox et al., 1986). Since the method is preferentially sensitive to thin electrical resistors such as hydrocarbon and gas reservoirs in depth, the method has recently demonstrated its commercial ability to evaluate the electrical resistivity of potential offshore hydrocarbon reservoirs before drilling (Eidesmo et al., 2002). The method is also being changed rapidly from a simple reservoir detecting tool to a multi-dimensional electromagnetic (EM) imaging and monitoring tool, trying to push the boundary of the EM monitoring capabilities (Gribenko and Zhdanov, 2007).

In this study, we investigate the feasibility of the CSEM method as a supplementary monitoring tool in water-saturated coalbed environments, though we continue our efforts

to develop efficient time-lapse seismic techniques as a primary subsurface monitoring tool. Before we present CSEM numerical modeling works and their analysis over the coalbed environment, we briefly summarize the basic rock physics and electromagnetics.

Rock Physics and Basic Electromagnetics

Electrical resistivity of rocks is highly sensitive to changes in brine saturation, as can be seen from plotting of Archie's law shown in Figure 18. As the electrically conductive pore fluid within a rock is replaced by the leaked CO₂ gas or other by-product gas, the electrical resistivity increases exponentially, resulting in a strong resistivity contrast between gas-saturated and brine-saturated geological media. For this type of geophysical scenario, the CSEM method would serve as an effective geophysical tool to monitor CO₂ leakage from a reservoir and supplement seismic methods with relatively low cost.

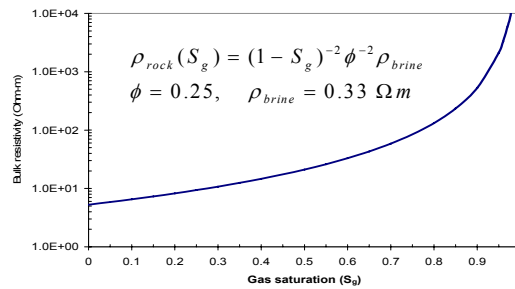


Figure 18: Archie's law and its plot (Gasperikova and Hoversten, 2006).

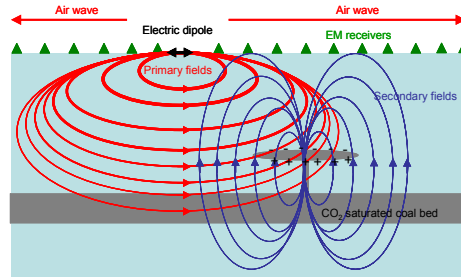


Figure 19: Electric dipole fields and charge buildups on the CO₂ plume.

In order to detect resistive CO₂ storage and its leakage, the CSEM method uses an electric dipole source and an array of multiple EM receivers as shown in Figure 19. The electric dipole source generates both vertical and horizontal electric fields in the subsurface and thus, drives currents in the subsurface. When the induced currents are normally incident upon the surfaces of the thin resistor, the governing boundary condition is continuity of normal current density:

$$J^N = J_1^N = J_2^N \quad (11)$$

where superscript, N indicate current density normal to the interface separating between the two media. Combining the equation above with Gauss's theorem results in buildups of anomalous surface charges, $Q_{surface}$:

$$Q_{surface} = J^N \left(\frac{\epsilon_1}{\sigma_1} - \frac{\epsilon_2}{\sigma_2} \right) \quad (12)$$

where ϵ is the dielectric permittivity (F/m). The perturbation due to $Q_{surface}$ in the existing electric and magnetic fields can be measured along the air-earth interface.

Creation of Time-lapse Geoelectrical Models

We first construct a series of geoelectrical models from flow simulation data using Archie's law. The flow model is built based on the coalbeds in the Powder River Basin. The flow simulation results (e.g., water saturation and gas saturation) plus lithology and porosity are then transformed into geoelectrical models as shown in Figure 20. Note there is a strong relationship between changes in gas saturation and changes in electrical resistivity. The CSEM responses to the models are computed using Schlumberger-Doll 2-D forward modeling code in the frequency domain and using EM1DSheet in the time domain.

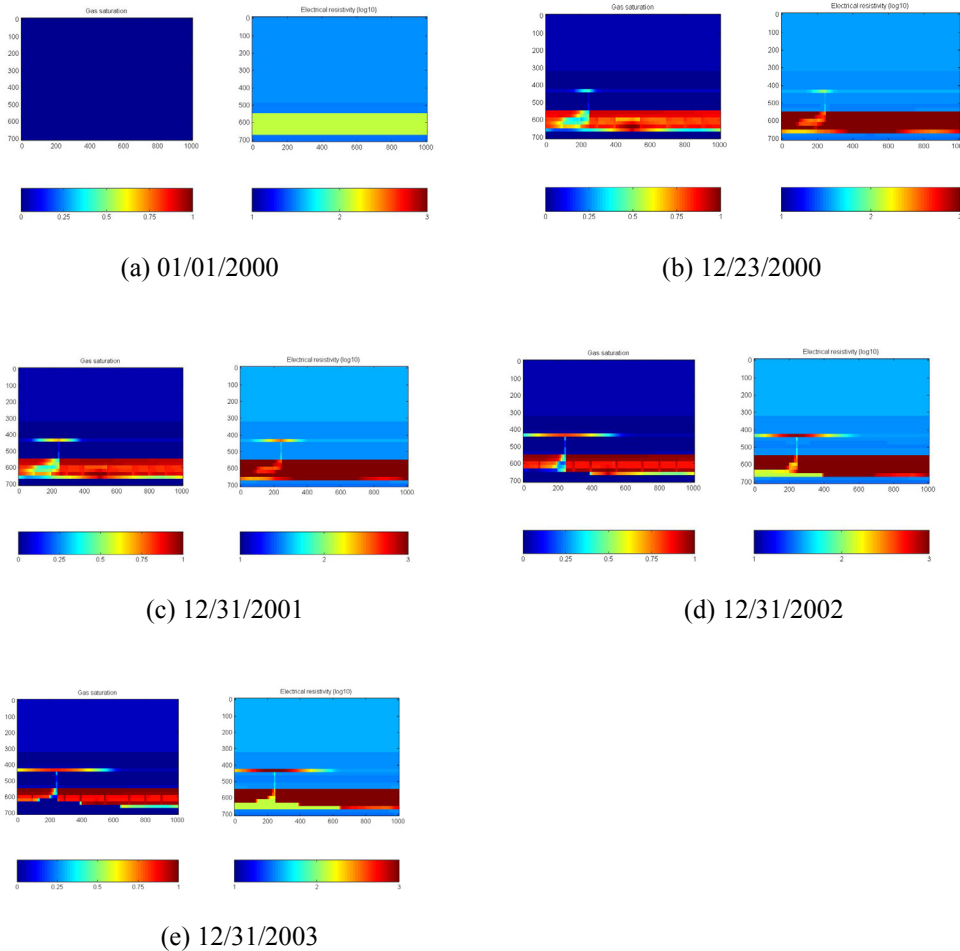


Figure 20: 2-D cross-sections of gas saturation (left) and electrical resistivity (right) at different times.

Sensitivity of the CSEM method to CO₂ plume

Frequency Domain Analysis

Synthetic CSEM measurements over the geoelectrical resistivity models shown in Figure 20 were generated at three different source frequencies: 22 Hz, 46 Hz and 100 Hz. Then, differences of the synthetic electric fields between the initial model and each model were plotted to demonstrate the sensitivity of the CSEM method to the CO₂ injection in Figure 21. In order to record the EM fields faithfully, 80 sets of EM receivers are densely placed with 50 m spacing.

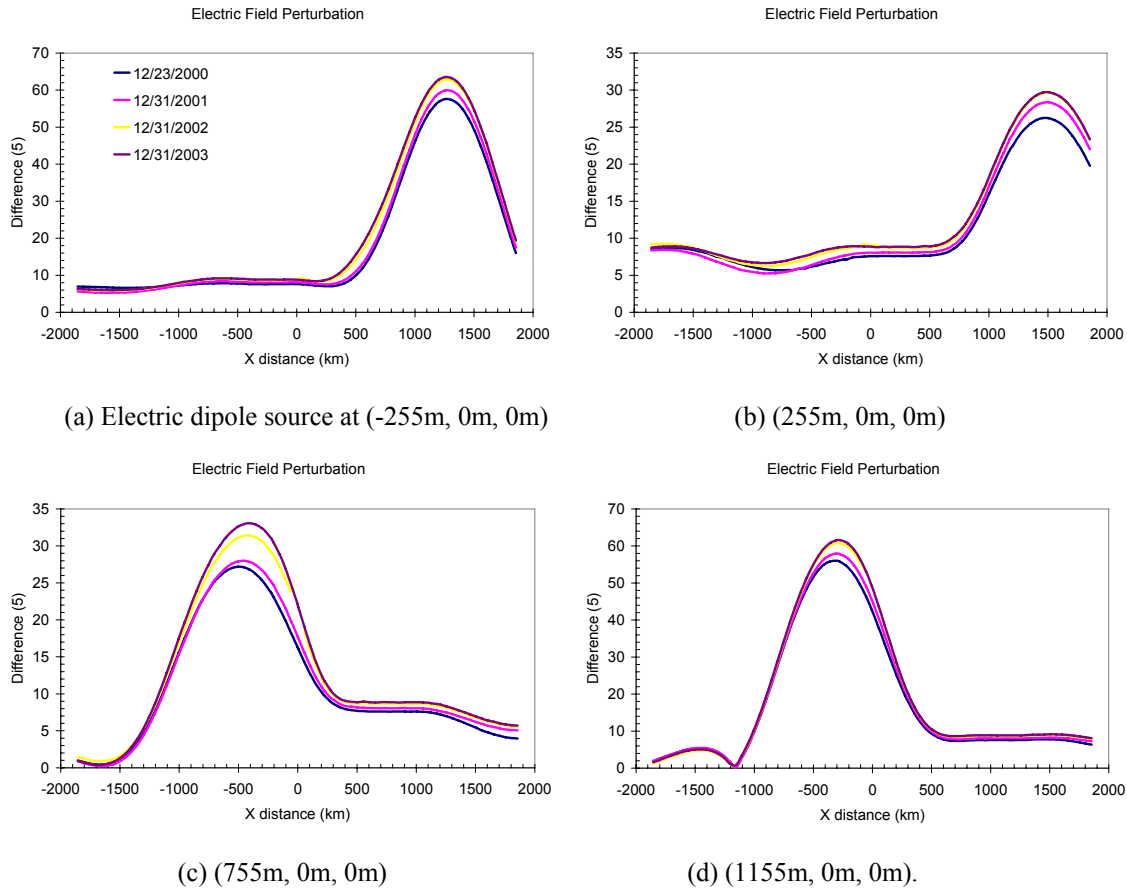


Figure 21: Difference (%) of the electric fields between the initial model and each model at four source positions.

Note that the CSEM method clearly detects the injection of the CO₂ gas into the coalbed in the first year. However, in the next following years, the relatively-small perturbations were observed. In order to examine how well the leakage can be imaged, the synthetic data were inverted. The background model without the injection is used as a starting model during the inversion process. The true model and inversion result are compared in Figure 22; the CSEM method fails to detect the thin CO₂ plume at 440 m depth, whereas it reasonably delineates the thick coalbed saturated with CO₂. Even though there exists sharp difference in electrical resistivity between the CO₂ plume and the background environment, the CSEM method is nearly blind to the thin leakage because of the following two reasons:

- Airwave that does not include any information about the subsurface dominates the subsurface responses, masking the weak anomalous response to the CO₂ leakage.
- Perturbation in electric field due to the coalbed is much larger than that due to the leakage, masking the weak anomalous response to the leakage.

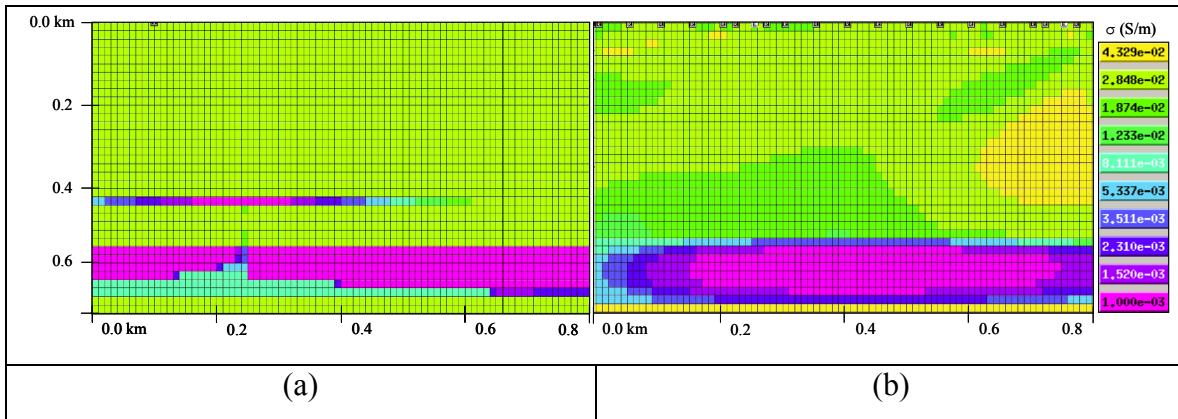


Figure 22: CSEM applications to monitoring CO₂ leakage in a terrestrial coalbed environment. (a) A 2-D geo-electrical model representing CO₂ leakage from the coalbed layers. (b) 2-D inversion result of synthetic FDCSEM data generated from (a).

Therefore, in order to use the CSEM method as a monitoring tool for geological CO₂ storage, it is necessary 1) to mitigate the effect of the airwave on the weak anomalous response and 2) to improve the amplitude of the anomalous response. As the first step of the efforts, we implement the CSEM method in the time domain in the next section. The primary advantage of the time-domain CSEM (TDCSEM) method over its frequency-domain counterpart is the fact that the airwave is naturally decoupled with subsurface EM measurements because the airwave travels at the speed of light in the air, whereas the subsurface EM responses diffuse slowly through conductive geological media. Such an example is demonstrated in the following section.

Time Domain Analysis

In this section, the previous 2-D geoelectrical models are replaced by two 10 Ohm-m half-space models with and without a 50 m thick, 200 Ohm-m layer buried at 400 m depth due to the current lack of multi-dimensional TDCSEM simulator¹.

In order to understand the basic characteristics of the TDCSEM method, a series of transient current snapshots over the homogeneous half-space model are presented in Figure 23. For more detailed analysis, the total transient current snapshots are also separated into the horizontal and vertical currents. Note that the vertical currents diffuse quickly downward at about 45°, whereas the horizontal currents diffuse slowly and laterally, and their maximum remains close to the earth's surface over time.

¹ SWP is currently developing an unstructured-mesh-based 3-D EM simulator to better test and evaluate monitoring capabilities of the TDCSEM method in more realistic CO₂ sequestration environments.

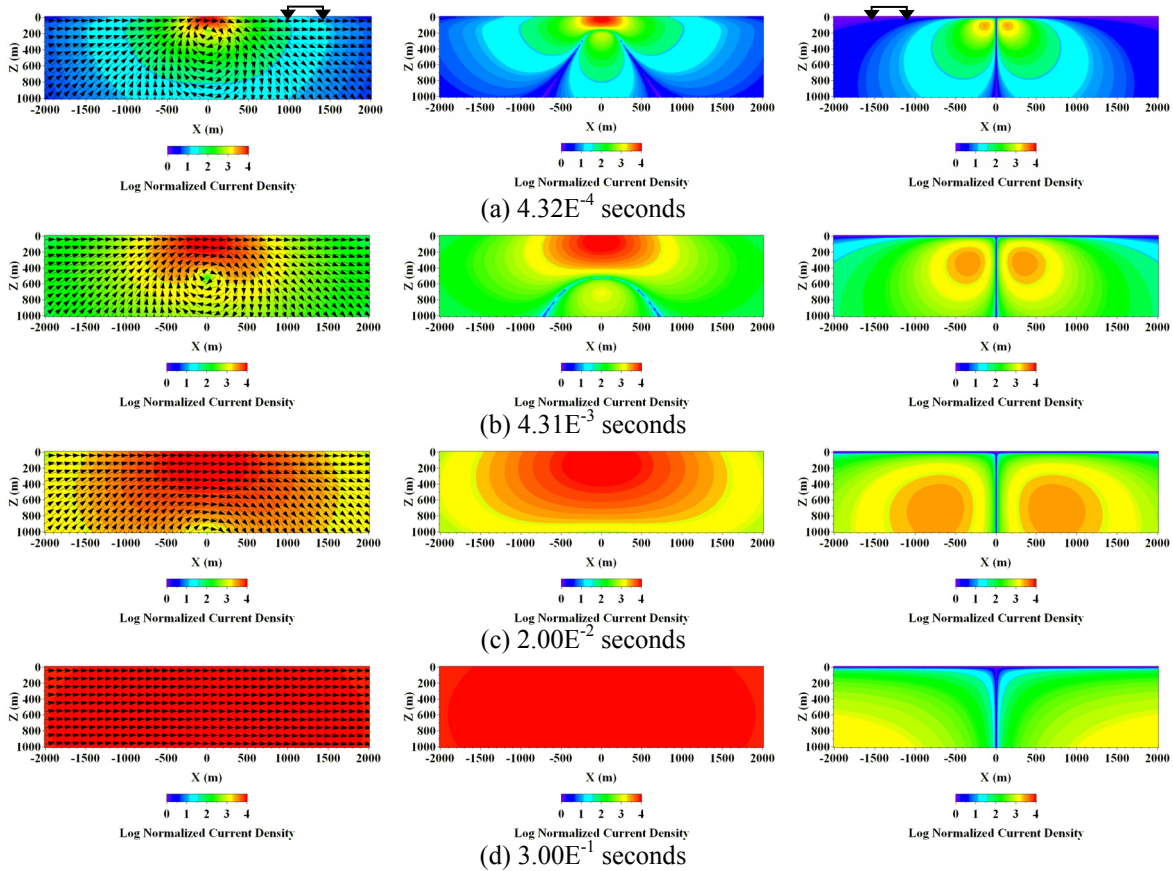


Figure 23: Total (left), horizontal (middle) and vertical (right) current density vector snapshots in the 10 Ohm-m homogeneous half-space model. A 250 m long, x-oriented electric dipole with $1.0E^{-4}$ second long ramp-off time is placed at the center of the model.

When a thin horizontal electrical resistor (e.g. geological CO₂ storage) is inserted in depth, the vertical currents will cause anomalous charge buildups on the surfaces of the resistor to satisfy the continuity of normal currents across the boundary, resulting in the perturbation in the background electric field. We want to measure the horizontal component of the perturbation on or beneath the earth's surface. In order to simulate the phenomena, the thin resistor is inserted into the half-space model. Current snapshots are calculated and presented in Figure 24. Note that in both models, the strong horizontal currents dominate the near-surface region. Therefore, although the charge buildup provides a perturbation in the transient electric field at the target depth, the horizontal component of the anomalous electric field near the earth's surface will be effectively masked by the strong near-surface horizontal currents which have no information about the resistor.

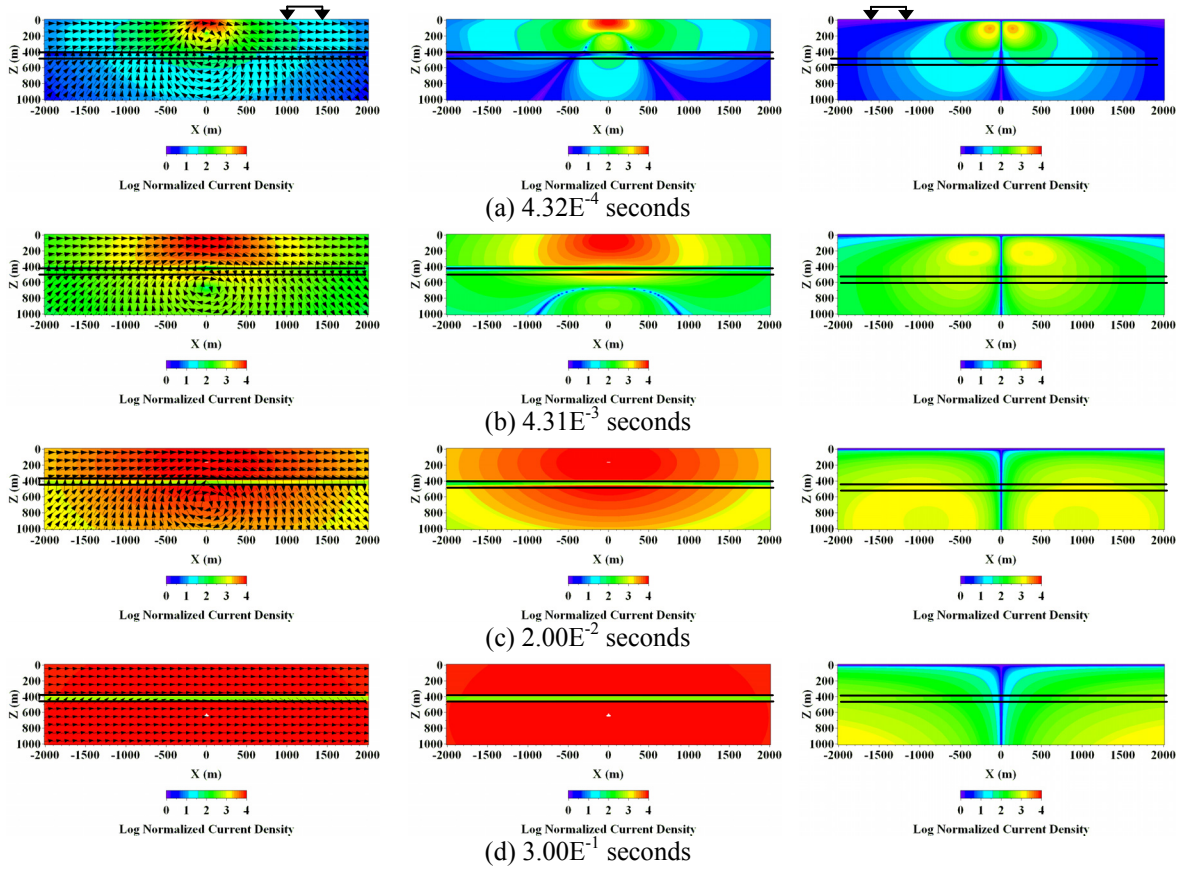


Figure 24: Total (left), horizontal (middle) and vertical (right) current density vector snapshots in the half-space model with the 50 m thick, 200 Ohm-m gas storage layer (denoted as the double black solid lines) at a depth of 400.

Consequently, the difference between the two models is clearly observed at the target depth in the vertical current snapshots, but is not obvious along the earth's surface in the horizontal current snapshots. As a result, when the surface electric fields are simulated over the half-space models with and without the resistor and plotted, the TDCSEM method does not distinguish between the two models as shown in Figure 25a.

A classic method for increasing the differences in the electric field measurements between the two models is to convert standard step-off responses into impulse responses by calculating the time-derivative of the recorded step responses (Edwards, 1997; Hördt et al., 2000). The time-derivatives of the step-off sounding curves shown in Figure 25a are presented in Figure 25b. Since an impulse source has a larger amount of high frequency contents than a standard step-off source, the near-surface horizontal currents are increasingly attenuated with source-receiver offsets over time; therefore, their masking effect on the anomalous electric field can be diminished.

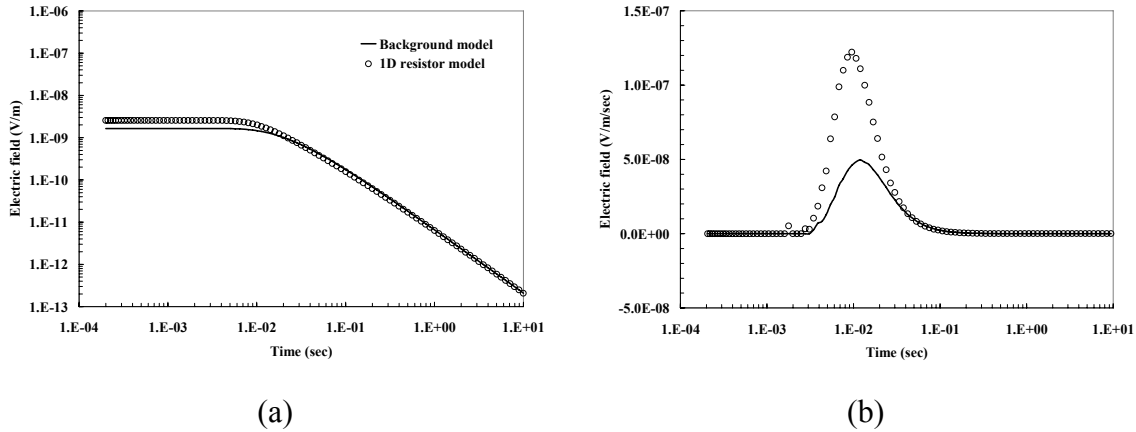


Figure 25: The inline horizontal electric field sounding curves over the half-space models with/without the CO₂ storage layer. (a) The inline electric field measurements excited by a step-off source waveform and (b) the time-derivative of the sounding curves in (a) to mimic the corresponding impulse responses.

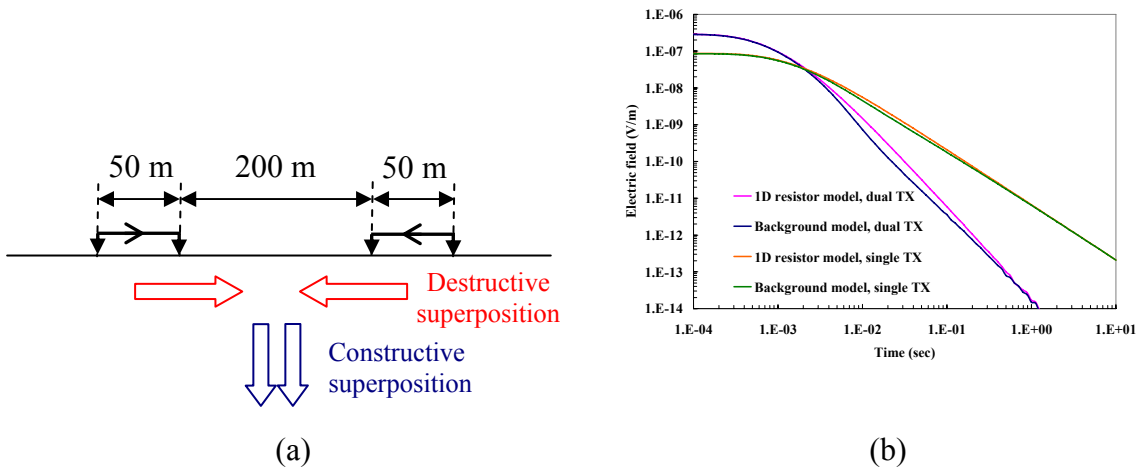


Figure 26: Sounding results over a 10 Ohm-m half-space with and without a 50 m thick, 200 Ohm-m gas storage buried at 400 m depth. (a) A dual source TDCSEM configuration with a synchronized step-off excitation. The arrows on the dipoles represent the direction of source polarization, and the fat arrows in the earth are transient currents. (b) Electric field measurements 300 m away from the center of the model (the center of the sources). The electric field measurements completed with a single 250 m-long source are superimposed for a direct comparison.

Another way to improve the sensitivity to the CO₂ storage is to split a single large electric dipole source into multiple smaller electric dipole sources and configure them concentrically. In such a configuration, transient vertical currents responsible for the galvanic response are constructively superimposed, producing larger galvanic responses at a region in which the CO₂ storage lies. In contrast, near-surface horizontal currents

from each source will interact destructively with each other at measurement points, reducing their masking effect on the useful galvanic responses. The simplest form of a multi-source TDCSEM configuration proposed here and its sounding curves are presented in Figure 26.

Since the amplitudes of the transient electric fields resulting from the dual source configuration decay rapidly over time, the quality of transient electric field measurements depends on the environment in which the data are acquired. However, this problem would be alleviated by configuring more small dipoles concentrically as shown in Figure 27, such that the galvanic responses become more constructively superimposed.

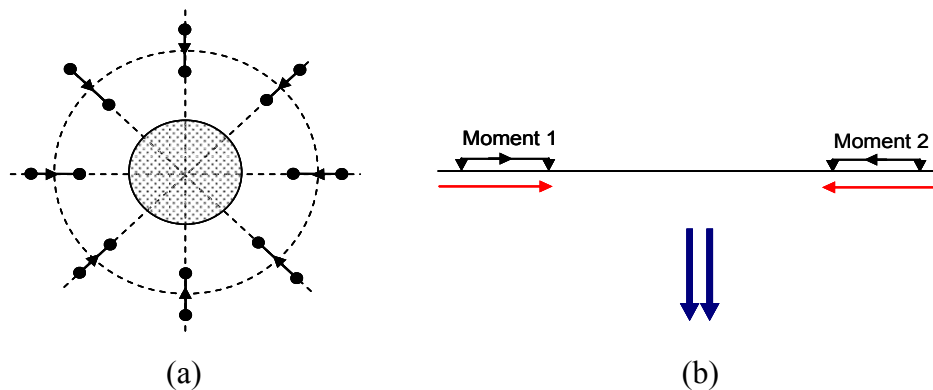


Figure 27: The concentric TDCSEM configuration. (a) Plan view: the black arrows represent source polarities. (b) Side view: The red and blue arrows represent horizontal and vertical transient currents, respectively. The constructively-superimposed vertical currents are expressed as thicker arrows. The same source moments are assigned to the dipoles such that the superimposed vertical currents can diffuse directly below the center of the circle.

Though the numerical modeling studies above were carried out in 1-D environments, the TDCSEM method looks more promising than the FDCSEM method because 1) it does not suffer from the airwave effects on a weak anomalous response, 2) impulse-like transient source pulse increases the sensitivity of the TDCSEM method to a resistive CO₂ storage in depth and 3) multi-source configurations also help reduce the near-surface horizontal currents at measurement points.

Conclusions

As demonstrated through simple 1-D and 2-D modeling, the TDCSEM application looks more promising for monitoring geological CO₂ storage than its frequency-domain counterpart since it is easier to remove what degrades the sensitivity of the CSEM method to the anomalous responses to the CO₂ storage and its leakage in the time domain.

References

- Ajo-Franklin, J. B., J. A. Urban, and J. M. Harris, 2005, Temporal integration of seismic traveltime tomography: 75th Annual International Meeting, SEG, Expanded Abstracts, 2468-2471.
- Cao, D., W.B. Bevdoun, S.C. Singn and A. Tarantola, A simultaneous inversion for background velocity and impedance maps: *Geophysics*, **55**, 458–469.
- Cox, C., S. Constable, A. Chave and S. Webb, 1986, Controlled-source electromagnetic sounding of the oceanic lithosphere, *Nature*, Vol. 320, 52-54.
- De Cesare, L., Myers, D. E., & Posa, D. (2001). Product-sum covariance for space-time modeling: an environmental application. *Environmetrics*, vol. 12 , 11-23.
- Devaney, A. J., 1984, Geophysical diffraction tomography: *IEEE Transactions on Geoscience and Remote Sensing*, **22**, 3-13.
- Eidesmo, T., S. Ellingsrud, L. MacGregor, S. Constable, M. Sinha, S. Johansen, F. Kong, and H. Westerdahl, 2002, Sea bed logging (SBL), a new method for remote and direct identification of hydrocarbon filled layers in deepwater areas: *First Break*, **20**, 144–152.
- Evensen, G., 2003, The ensemble Kalman filter: Theoretical formulation and practical implementation: *Ocean Dynamics*, **53**, 343–367.
- Evensen, G. 2007, *Data Assimilation – the Ensemble Kalman Filter*: Springer
- Francis, A., 2005, Limitations of deterministic and advantages of stochastic inversion: *CSEG Recorder*, February 2005.
- Gasperikova, E. and M. Hoversten, 2006, A feasibility study of nonseismic geophysical methods for monitoring geologic CO₂ sequestration, *The Leading Edge*, Vol. 25, No. 10, 1282-1288.
- Geologic Storage of CO₂, 2007, GCEP Annual Report.
- Gribenko, A. and M. Zhdanov, 2007, Rigorous 3D inversion of marine CSEM data on the integral equation method, *Geophysics*, Vol. 72, No. 2, WA73-WA84.
- Haas, A., and O. Dubrule, 1994, Geostatistical inversion — A sequential method of stochastic reservoir modeling constrained by seismic data: *First Break*, **12**, 561–569.
- Hansen, P. C., 1992, Analysis of discrete ill-posed problems by means of the l-curve, *SIAM Review*, **34**, 561-580.
- Harris, J. M., 1987, Diffraction tomography with discrete arrays of sources and receivers, *IEEE Transactions on Geoscience and Remote Sensing*, V. GE-25, n. 4, p. 448-455.
- Keeling, C. D., & Whorf, T. P., 2005, Atmospheric CO₂ records from sites in the SIO air sampling network. In *Trends: A Compendium of Data on Global Change*. Laboratory, Carbon Dioxide Information Analysis Center Oak Ridge National, Oak Ridge, Tenn., U.S.A.: U.S. Department of Energy.
- Mandel, J., 2006, Efficient implementation of the ensemble Kalman filter: CCM Report 231, University of Colorado at Denver and Health Sciences Center.
- McKenna, J., Sherlock, D., & Evans, B., 2001, Time-lapse 3-D seismic imaging of shallow subsurface contaminant flow: *Journal of Contaminant Hydrology*, vol. 53, 133-150.
- Oldenburg, D. W., T. Scheuer, and S. Levy, 1983, Recovery of the acoustic impedance from reflection seismograms: *Geophysics*, **48**, 1318–1337.

- Peterson, J. E., B. J. P. Paulsson, and T. V. McEvelly, 1985, Applications of algebraic reconstruction techniques to crosshole seismic data: *Geophysics*, v. 50. no. 10, p. 1566-1580.
- Rickett, J., and D. Lumley, 2001, Cross-equalization data processing for time-lapse seismic reservoir monitoring: A case study from the Gulf of Mexico: *Geophysics*, **66**, 1015-1025.
- Rocha Filho, A. A., 1997, Geophysical diffraction tomography: multifrequency matrix formulation and integrated inversion (in Portuguese): M.Sc. Dissertation, Federal University of Bahia.
- Sancevero, S.S, A.Z. Remacre, R. S. Portugal, 2005, Comparing deterministic and stochastic seismic inversion for thin-bed reservoir characterization in a turbidite synthetic reference model of Campos Basin, Brazil: *The Leading Edge*, February 2005, 1168–1172.
- Santos, E. T. F., 2006, Anisotropic seismic tomographic inversion with optimal regularization (in Portuguese): D.Sc. Thesis, Federal University of Bahia.
- Santos, E. T. F., and J. M. Harris, 2007, Time-lapse Diffraction Tomography for Trigonal Meshes with Temporal Data Integration Applied to CO₂ Sequestration Monitoring: 77th Annual International Meeting, SEG, Expanded Abstracts, 2959-2963.
- Santos, E. T. F., and A. Bassrei, 2007, L- and Theta-curve approaches for the selection of regularization parameter in geophysical diffraction tomography: *Computers & Geosciences*, **33**, 618-629.
- Strack, K.M., 1984, The deep transient electromagnetic sounding technique: first field test in Australia, *Exploration Geophysics*, Vol. 15,251-259.
- Stewart, R. R., 1992, *Exploration seismic tomography-fundamentals*, Course Notes Series, V. 3: Tulsa, Oklahoma, Society of Exploration Geophysicists.
- Tikhonov, A. N., and V. Y. Arsenin, 1977, *Solution of Ill-Posed Problems*: Wiley.
- Wu, R-S, and M. N. Toksöz, 1987, Diffraction tomography and multisource holography applied to seismic imaging. *Geophysics*, **52**, 11-25.

Future Plans

The results we have published/presented to date very much represent a work in progress. We plan to expand our efforts in several areas as detailed next.

Sequestration of CO₂ and ECBM in unmineable coal seams

First, we plan to continue extensive experimentation. We will repeat geomechanical and flow experiments at increased stresses, pore pressures, and temperature, in order to better simulate the *in situ* conditions of the coal beds in the Powder River Basin. We also plan to make measurements using pure methane and gas mixtures. It is also important to test whether or not the observations of creep strain, velocity change, and decreasing bulk modulus are reversible when the CO₂ is desorbed. Testing this will improve our understanding of the effect of CO₂ on the coal matrix.

The decrease in permeability following CO₂ saturation suggests that the coal matrix is swelling in response to adsorption. However, it is also possible that the adsorbed CO₂ is simply filling the pore space, and physically impeding flow. Distinguishing between these two effects is important for testing and building theoretical models relating adsorption and flow, but difficult in practice, because both mechanisms would cause a decrease in permeability. The experimental efforts headed by Mark Zoback and Tony Kovscek will continue their close collaboration to unravel the effects of swelling. The Kovscek group focuses on adsorption induced changes in permeability to gas and the Zoback group focuses on geomechanical response to permeability.

Our effort to characterize the nature of adsorbed gas mixtures on coal surfaces will continue. We seek to understand the level of complexity needed to obtain accurate multicomponent gas isotherm models as well as the degree of nonideality displayed by the adsorbed gas phase. We plan to follow the general methodology for multicomponent adsorption laid out by Talu [1].

Additionally, the variety of length scales exhibited by coal pore space dictate that we understand both convective and diffusion transport in coal coupled with multicomponent isotherms. Our prior experiments of gas-gas displacement in coal were constructed so that diffusive mass transfer limitations were minimized. We are expanding our understanding of diffusive transport in coal matrix because it is the most immature. We seek an understanding of whether countercurrent diffusion aids or impedes carbon dioxide penetration of the matrix.

We also plan to focus on deriving a constitutive law and failure envelope for coal. Observations of creep strain in the presence of CO₂ suggest that the coal becomes viscous. It is possible that this is a manifestation of coal plasticization at low temperature. To better understand this, we plan to conduct a series of creep strain tests

as a function of temperature. We also plan to investigate the effect of CO₂ on the compressive strength of coal. It is possible that shear failure of coal in the near wellbore region may be another means of overcoming loss of injectivity due to swelling.

Feasibility assessment of CO₂ Sequestration and Enhanced Recovery in Gas Shales

We are currently negotiating with several oil and gas companies for access to samples and data from gas shale reservoirs. Once the samples and data arrive in early summer 2008, we will begin a comprehensive study to test the feasibility of carbon sequestration and enhanced recovery using laboratory studies, fluid flow simulations, and integrated assessment techniques.

Laboratory Studies

In order to model the process of carbon sequestration and enhanced recovery in gas shale reservoirs, a collection of material properties must be used as inputs for fluid flow simulation. Because so little is known about the physical properties of gas shales, this study will investigate both adsorption and mechanical properties of shale samples to use as inputs for simulation.

To measure the mechanical and adsorption properties of gas shale samples, a triaxial press apparatus will be used. With this setup, we will measure adsorption properties at varying pressures and temperatures, as well as static and dynamic mechanical properties like Young's modulus, compressibility, and Poisson's ratio. In addition, we will measure permeability on the intact shale matrix using pressure pulse transient testing. As coals are known to exhibit change in physical properties as a function of the gas adsorbed to the matrix, He, CH₄, and CO₂ will be varied within the sample to test for property changes.

Specific research questions to be addressed by these experiments include:

- Do Barnett shale samples show preferential adsorption of CO₂ over CH₄?
- Does adsorption in shales exhibit hysteresis, as has been seen in coals?
- Do the mechanical properties of the Barnett shale depend on gas composition?
- Do shales exhibit shrinkage or swelling with adsorption that might affect permeability, as has been seen in coals?
- What is the permeability of the intact matrix?
- Can a composition-based metric be determined for adsorption parameters?

Field-Scale Simulation

The goal of this portion of the project is to test whether CO₂ sequestration and enhanced recovery are feasible in a producing gas shale field. Using the data acquired from experimental efforts, along with geological, geophysical, and production data from a real-world reservoir, three-dimensional fluid flow simulations will be conducted on a set of probable reservoir models. These simulations will test if the volume of CH₄ that can be produced and the volume of CO₂ that can be sequestered in a gas shale

reservoir is promising. The study will also test the importance of different reservoir properties for enhanced recovery and sequestration.

The basic workflow of this study will follow that used in previous studies on coalbed methane is comprised primarily of two steps, stochastic reservoir modeling and fluid flow simulation. The stochastic modeling will employ geostatistical techniques to populate a 3D grid with reservoir properties by using spatial correlations that are conditional to the sampled data. All available data (e.g. well logs, laboratory measurements, seismic, etc.) will be used to populate a gridded structural model filled with petrophysical properties.

For fluid flow simulations, we will use the Computer Modeling Group's simulator GEM. GEM is a compositional reservoir simulator with the ability to simulate dual porosity, multiple gas components, mixed gas diffusion, mixed gas adsorption, and stress dependent porosity and permeability. GEM has been used with success in studies of CO₂ sequestration in coal beds, and thus it is expected to be successful in simulating gas shale reservoirs because of the similarity in physical properties.

Overall, the simulation study will directly address the following questions:

- What is a reasonable estimate of enhanced recovery potential in the Barnett shale?
- What is a reasonable estimate of CO₂ sequestration potential in the Barnett shale?
- What is a reasonable estimate of CO₂ injectivity in the Barnett shale?
- What well configuration will co-optimize enhanced recovery and sequestration?
- How should the complex fracture network in the Barnett shale be modeled?
- What effect do the following geologic properties, geomechanical properties, and engineering practices have on enhanced recovery and sequestration?
 - Fracture spacing and orientation
 - Fracture permeability and porosity
 - Shale matrix permeability and porosity
 - Shale thickness, dip and depth
 - Reservoir pressure and temperature
 - Adsorption isotherms
 - Shale composition
 - Diffusion coefficients
 - Rock compressibility in the matrix and fractures
 - Seal capacity

Integrated Assessment

We will use the results of the flow simulation to answer questions related to CO₂ sequestration capacity, CO₂ leakage risk, and CO₂ sequestration economics in gas shale reservoirs.

Nuttall et al. [2] reported a sequestration capacity of 25 GtCO₂ in the Devonian shales of Kentucky. This large estimate is based on an average adsorption capacity for Kentucky black shales multiplied with an estimate of black shale volume in the state. This methodology gives an absolute upper bound for sequestration capacity under ideal conditions. Given the low permeability of gas shale reservoirs, it is likely that effective sequestration capacity will be much lower than this upper bound. In addition, injectivity may be quite low, thus limiting the rate at which CO₂ can be sequestered. The flow simulations will give an estimate of effective storage capacity for a shale gas sequestration project. This value will then be extrapolated to estimate the total sequestration capacity in the Barnett shale. It will also give a first-order estimate of sequestration capacity in other shale gas reservoirs based on a ratio of gas-in-place to carbon sequestration potential. The estimate of total capacity can then be used to gauge the potential of shale gas reservoirs as sequestration targets and guide the priorities of future research.

The risk of CO₂ leakage from a gas shale sequestration project is as of yet unknown. In the traditional model of sequestration, shale layers are considered the seal for injection, rather than the reservoir. Thus, there may be unique challenges and risks that are not well captured by the existing models for leakage. A particular focus will be on the extent of vertical migration of CO₂ within the reservoir and how effective the adsorption of CO₂ is within the reservoir. Specific flow simulations may address slow leakage through the overlying units to estimate the scale of the problem. In addition, geomechanical constraints will be applied to minimize risk of fracturing out of the Barnett shale into overlying formations. Simple estimates of leakage risk will be used as a cost input for economic analysis.

Using the results of the flow simulations, along with information on the costs associated with drilling and production, the economic feasibility of a gas shale injection project will be calculated. This analysis will use the techniques to measure the net present value (NPV) of a sequestration project as has been done for previous ECBM studies.

Integrating fluid flow and geomechanical models for CO₂ leakage risk assessments

We have started collaborating with David Gray from CGGVeritas, to use AVAZ (Azimuth Versus Angle and aZimuth) [3] to obtain information from pre-stack seismic data about fracture density and orientation in the caprock. These results will be later incorporated in the reservoir simulation to predict what will happen with the CO₂ if the fractures are reactivated.

Reservoir stimulation and permeability enhancement via induced microseismicity

The next step in this project will consist in the analysis of the data with the objective of detecting changes in permeability as a consequence of the injection and induced microseismicity and understanding the spatial-temporal behavior of the induced microearthquakes. We will model the system with SHIFT (Simulator for

Hydraulic Injection and Fracture Treatment) [4] that simulates shearing of fractures and permeability changes by solving interactions between fluid flow and rock mechanics [5], utilizing the stress state we have determined.

As an input for SHIFT, we need to create a reservoir model, incorporating a discrete fracture network. Few of these fractures were observed in the FMI log of well 4-30 and we expect that by analyzing the induced seismicity it will be possible to determine lineaments that represent the fracture network that had been activated as a result of the injection.

Coalbed Fires

The field observations and interpretations of the study coalbed fire area will continue to be assembled. An ultimate goal is to produce to date the most accurate description of the anatomy and mechanics of a subsurface fire. We plan to refine our understanding of the mechanics of fissure formation by making the boundary conditions for the calculation more realistic (a semi-infinite domain instead of an infinite one, for example). This understanding may lead to an improved description of air transport into coal beds. We shall delineate more accurately where combustion is taking place now by a combination of surface temperature observations and possible seismic imaging of the burned zone. Additionally, we shall estimate the overall rate of coal combustion from estimates of gas flow rates for passages of dimensions constrained by field observations and fissure calculations described above. The pressure gradients that drive flow of O₂, in the form of air, to the combustion zone and the release of hot gases from it using a combustion simulator shall also be estimates so as to determine whether it is possible to disrupt those pressure gradients by fluid injection in a way that excludes O₂ from the combustion zone and extinguish the fire.

Monitoring

We plan to test the EnKF seismic inversion method on continuous monitoring and develop a localized imaging technique. In this way, data can be acquired or sorted by patches, and the data in each patch may be sorted as a common reflection gather and stacked as a single trace for the seismic inversion. We will apply data evolution to transmission and reflection seismic tomography. The CSEM research has just started. We are developing a 3-D finite-element time-domain EM diffusion simulator to better handle complex subsurface geology and subtle geometric changes in CO₂ storage.

References

1. Talu, O., Needs, Status, Techniques and Problems with Binary Gas Adsorption Experiments, Adv. in Colloids and Interface Science, 76-77, 227-269, 1998.
2. Nuttall et al, Analysis of Devonian black shales in Kentucky for potential carbon dioxide sequestration and enhanced natural gas production, Kentucky Geological Survey. 2005.
4. Gray, F.D., Head, K.J., Chamberlain, C.K., Olson, G., Sinclair, J. and Besler, C., Using 3D Seismic to Identify Spatially Variant Fracture Orientation in the Manderson Field, paper SPE 5636 presented at the 1999 SPE Rocky Mountain Regional Meeting, Gillette, WY, May 15-18, 1999.
4. SHIFT software provided by JAPEX.

5. Tezuka, K., Hydraulic Injection and Microseismic Monitoring in the Basement Gas Reservoir in Japan: 2006 SPE Forum Series in Asia Pacific - Hydraulic Fracturing Beyond 2010, Macau, China, Society of Petroleum Engineers, 2006.

Publications

1. Brown, S., Bussod, G., and Hagin, P., AVO monitoring of CO₂ sequestration: A benchtop-modeling study, *The Leading Edge*, **26**, 1576, 2007.
2. Hagin, P., and Zoback, M., Physical Properties of Low-Rank Coal Samples from the Powder River Basin, Wyoming, *presented at Coal-Seq VI Forum*, April 10-11, 2008.
3. Lucier, A., and Zoback, M., Assessing the Economic Feasibility of Regional Deep Saline Aquifer CO₂ Injection and Sequestration, *presented at GCEP Research Symposium*, October 1-3, 2007.
4. Ross, H., Zoback, M., and Hagin, P., CO₂ Sequestration and Enhanced Coalbed Methane Recovery: Reservoir Characterization and Fluid Flow Simulations of the Powder River Basin, Wyoming, *presented at GCEP Research Symposium*, October 1-3, 2007.
5. Chiaramonte, L., Zoback, M., Friedmann, J. and Stamp, V. (2007). Seal Integrity and Feasibility of CO₂ Sequestration in the Teapot Dome EOR Pilot: Geomechanical Site Characterization. *Environmental Geology*, on-line first, doi:10.1007/s00254-007-0948-7, July 2007. Submitted: June 2006.
6. Chiaramonte, L., Zoback, M., Friedmann, J. and Stamp, V. (2007). Fluid Flow Simulation for CO₂-EOR and Sequestration Utilizing Geomechanical Constraints - Teapot Dome Oil Field, Wyoming. Accepted AGU Fall Meeting 2007.
7. Chiaramonte, L., Lucier, A., Ross, H. and Zoback, M. (2007). Geomechanics and Seal Integrity for Geologic Sequestration of CO₂. Abstracts of the IWCCS-07 Meeting, NGRI, Hyderabad, India.
8. Chiaramonte, L., Zoback, M., Friedmann, J. and Stamp, V. (2006). Geomechanical Reservoir Characterization for Prediction of the Likelihood of Faulting Induced by CO₂ Sequestration, *Eos Trans. AGU*, **87** (52), Fall Meet. Suppl., Abstract T12A-07.
9. Chiaramonte, L., Zoback, M., Gerst, J. and Gupta, N. (2007). Can controlled induced microseismicity be used to enhance permeability in geological CO₂ sequestration targets? NETL 6th Annual Conference on Carbon Capture & Sequestration, Pittsburgh, PA.
10. Kovscek, A.R., Lin W., Tang, G.-Q. and Jessen, K., "Laboratory and Simulation Investigation of Gas Adsorption, Transport, and Carbon Sequestration in Coal," U43C-1400 American Geophysical Union 2007 Fall Meeting, San Francisco, CA December 10-14, 2007.
11. Lin. W., G.-Q. Tang, and A. R. Kovscek, "Sorption-Induced Permeability Change of Coal During Gas-Injection Processes," *SPE Reservoir Engineering and Evaluation*, to appear.
12. Jessen, K., Tang, G.-Q. and A. R. Kovscek, "Laboratory and Simulation Investigation of Enhanced Coalbed Methane Recovery by Gas Injection," *Transport in Porous Media*, to appear.
13. Lin. W., G.-Q. Tang, and A. R. Kovscek, "Sorption-Induced Permeability Change of Coal During Gas-Injection Processes," SPE-109855, Proceedings of the SPE Annual Technical Conference and Exhibition, Anaheim, CA. Nov. 11 - 14, 2007.
14. Jessen, K., G.-Q. Tang, and A. R. Kovscek, "Multicomponent Sorption Modeling in ECBM Displacement Calculations" SPE-110258, Proceedings of the SPE Annual Technical Conference and Exhibition, Anaheim, CA. Nov. 11 - 14, 2007.
15. Quan, Y. and J.M. Harris, 2008, Stochastic Seismic Inversion using both Waveform and Traveltime Data and Its Application to Time-lapse Monitoring: SEG Expanded Abstracts.
16. Santos, Eduardo T. F. and Jerry M. Harris, DynaSIRT, 2008, A Robust Dynamic Imaging Method Applied to CO₂ Sequestration Monitoring, SEG Extended Abstracts.
17. Santos, E.T.F., Harris, J., Bassrei, A., Costa, J.C., 2007, Regularized diffraction tomography for trigonal meshes applied to reservoir monitoring. In: X Congresso Internacional da Sociedade Brasileira de Geofisica, Rio de Janeiro.
18. Santos, Eduardo T. F. and Harris, Jerry M., 2007, Time-lapse diffraction tomography for trigonal meshes with temporal data Integration applied to CO₂ sequestration monitoring, SEG Extended Abstracts.

Contacts

Jerry M. Harris: harris@stanford.edu
Anthony R. Kovscek: kovscek@stanford.edu
Franklin M. Orr, Jr.: fmorr@stanford.edu
Mark D. Zoback: zoback@stanford.edu
Paul Hagin: phagin@Stanford.edu
Youli Quan: quany@stanford.edu
Eduardo Santos: eduardot@stanford.edu
Tom Tang: ttcv@chevron.com
Tope Akinbehinje: topeakin@stanford.edu
Adeyemi Arogunmati: aadeyemi@stanford.edu
Laura Chiaramonte: chiarlau@stanford.edu
Jolene Robin-McCaskill: jmrobin@stanford.edu
John P. Vermilyen: vermylen@stanford.edu
Abhishek Dutta: adutta@stanford.edu
Taku Ide: idetaku@stanford.edu
Wenjuan Lin: wenjuanl@stanford.edu
Evan Um: eum@stanford.edu